

# **Magnetism of Single Adatoms and Small Adsorbed Clusters Investigated by Means of Low-Temperature STM**

THÈSE N° 5727 (2013)

PRÉSENTÉE LE 25 AVRIL 2013  
À LA FACULTÉ DES SCIENCES DE BASE  
LABORATOIRE DE NANOSTRUCTURES SUPERFICIELLES  
PROGRAMME DOCTORAL EN PHYSIQUE

ÉCOLE POLYTECHNIQUE FÉDÉRALE DE LAUSANNE

POUR L'OBTENTION DU GRADE DE DOCTEUR ÈS SCIENCES

PAR

Quentin DUBOUT

acceptée sur proposition du jury:

Prof. G. Meylan, président du jury  
Prof. H. Brune, directeur de thèse  
Prof. M. Grioni, rapporteur  
Dr J. Wiebe, rapporteur  
Prof. Ph. Willmott, rapporteur



ÉCOLE POLYTECHNIQUE  
FÉDÉRALE DE LAUSANNE

Suisse  
2013



# Abstract

This thesis works reports on the magnetic properties of single transition metal atoms and hydrogenated compounds adsorbed on crystal surfaces. It is an experimental study, based on scanning tunneling microscopy (STM), initiated by the project of demonstrating the existence of magnetic remanence for single adsorbed atoms (adatoms). All the measurements have been performed with a scanning tunneling microscope operating at 0.4 K and equipped with 8.5 T superconducting coils. The investigated systems are cobalt atoms, pure and hydrogenated (cobalt hydrides), adsorbed on Pt(111) and graphene on Pt(111) surfaces.

In the first case, we have immediately been confronted to the presence of cobalt hydrides on the surface. Three types of hydrides ( $\text{CoH}$ ,  $\text{CoH}_2$ , and  $\text{CoH}_3$ ) have been identified, quite different from the clean adatoms, and readily distinguished by their tunnel spectrum (STS). Two of these hydrides display low-energy vibrational modes (1 – 30 meV), identified by their absence of response to a magnetic field, the effect of an isotopic substitution, and by comparison with known systems. The three hydrides can be deprotonated applying a sufficient voltage between tip and sample.  $\text{CoH}_2$  on Pt(111) presents a Kondo resonance, due to a half-integer spin ( $S = 3/2$ ) and a peculiar magnetic anisotropy. This system corresponds to the first demonstration of the appearance of the Kondo effect upon hydrogen adsorption. The results of several attempts to observe remanence for single cobalt adatoms on Pt(111) with spin-polarized scanning tunneling microscopy (SP-STM) are also presented and discussed.

The second system differs from the first one in the presence of a graphene layer on the Pt surface. The first experimental determination of the magnetic moment and magnetic anisotropy of adatoms on graphene is reported in this thesis. A magnetic moment of  $(2.2 \pm 0.4) \mu_B$  was measured by spin-excitation spectroscopy (SES), as well as a hard magnetization axis with an anisotropy energy of  $8.1 \pm 0.4$  meV. This value, comparable to the record value of single cobalt atoms on Pt(111), has been mainly attributed to the strong hybridization between cobalt and graphene. *Ab initio* calculations confirmed our observations. Graphene thus represents an extremely promising substrate for future applications in nanoscale magnetism and spintronics.

This system also exhibits three different cobalt hydrides in addition to the clean atoms. Their respective chemical composition,  $\text{CoH}$ ,  $\text{CoH}_2$ , and  $\text{CoH}_3$ , was determined by direct comparison between high resolution STM images and simulated images obtained from *ab initio* calculated atomic structures. A controlled deprotonation method is presented.  $\text{CoH}_3$  is the only hydride to display spin excitations. Its magnetic moment is comparable to that of clean cobalt, it presents a hard magnetization axis as well, however, its magnetic anisotropy energy

---

is sensibly lower,  $1.7 \pm 0.05$  meV. The other two hydrides display vibrational excitations only. The effect of hydrogen on the magnetic properties of metal adatoms is therefore very strong in this system as well, and must be taken into account in future studies, hydrogen being a very common contaminant in ultra-high vacuum set-ups.

Finally, a detailed study of the structure graphene mono- and bilayers on Ru(0001) was realized. Two different stackings, AB and AA, have been identified for the bilayers, the last one not observed to date for this system. The moiré structure of monolayer graphene and of this last type of bilayer has been determined:  $(11.57 \times 11.57) R4.3^\circ$  and  $(10.54 \times 10.54) R4.7^\circ$ , respectively. Moreover, C-C bond distortions of more than 10%, observed in the STM images, have been studied in detail. A quantitative comparison with *ab initio* calculations allowed to identify their origin as the tilt of the graphene  $\pi$ -orbitals. These distortions are therefore purely artificial. This is an important result for future scanning tunneling microscopy studies of graphene.

**Keywords:** scanning tunneling microscopy (STM), spin-polarized scanning tunneling microscopy (SP-STM), scanning tunneling spectroscopy (STS), spin-excitation spectroscopy (SES), atomic magnetism, magnetic remanence, Kondo effect, single atoms, adatoms, cobalt, hydrides, platinum, graphene, ruthenium.



# Résumé

Cette thèse traite des propriétés magnétiques d'atomes isolés de métaux de transition et de le composés hydrogénés adsorbés sur des surfaces cristallines. Il s'agit d'une étude expérimentale, basée sur la microscopie à effet tunnel (STM), dont le point de départ consiste en la tentative de démontrer l'existence de la rémanence magnétique pour des atomes adsorbés (adatoms) isolés. L'ensemble des mesures a été effectué à l'aide d'un microscope à effet tunnel fonctionnant à 0.4 K et équipé de bobines supraconductrices de 8.5 T. Les systèmes étudiés sont des atomes de cobalt, purs et hydrogénés (hydrures de cobalt), adsorbés sur des surfaces de Pt(111) et de graphène sur Pt(111).

Dans le premier cas, nous avons été immédiatement confrontés à la présence d'hydrures de cobalt sur la surface. Trois types d'hydrures ( $\text{CoH}$ ,  $\text{CoH}_2$  et  $\text{CoH}_3$ ) ont été identifiés, bien différents des adatoms propres, facilement distinguables par leur spectre tunnel (STS). Deux de ces hydrures montrent des modes vibratoires de basse énergie (1 – 30 meV), identifiés par leur absence de réponse à un champ magnétique, l'effet d'une substitution isotopique, et par comparaison avec des systèmes connus. Les trois hydrures peuvent être déprotonés en appliquant une tension suffisante entre la pointe et l'échantillon.  $\text{CoH}_2$  sur Pt(111) présente une résonance Kondo, due à un spin demi-entier ( $S = 3/2$ ) et à une anisotropie magnétique particulière. Ce système constitue la première démonstration de l'apparition de l'effet Kondo suite à l'adsorption d'hydrogène. Plusieurs tentatives d'observation de rémanence pour des adatoms isolés de cobalt sur Pt(111) par microscopie à effet tunnel polarisée en spin (SP-STM) sont présentées et commentées.

Le second système diffère du premier du fait de la présence d'une couche de graphène sur la surface de Pt(111). La première détermination expérimentale du moment magnétique et de l'anisotropie magnétique d'adatoms sur du graphène est rapportée dans cette thèse. Nous avons mesuré un moment magnétique de  $(2.2 \pm 0.4) \mu_B$ , ainsi qu'un axe de magnétisation difficile avec une énergie d'anisotropie magnétique de  $8.1 \pm 0.4$  meV, par spectroscopie à excitations de spin (SES). Cette dernière valeur, comparable à la valeur record des atomes isolés de cobalt sur Pt(111), a été attribuée principalement à l'hybridation importante entre le cobalt et le graphène. Des calculs *ab initio* confirment nos observations. Le graphène constitue donc un substrat extrêmement prometteur pour de futures applications en nanomagnétisme et spintronique.

Ce système présente lui-aussi trois différents hydrures de cobalt en plus des atomes propres. Leur composition chimique respective,  $\text{CoH}$ ,  $\text{CoH}_2$ , et  $\text{CoH}_3$ , a été déterminée par comparaison d'images de microscopie à effet tunnel haute résolution avec des images simulées

---

obtenue à partir de structures atomiques calculées *ab initio*. Une méthode de déprotonation contrôlée est présentée.  $\text{CoH}_3$  est le seul hydruure à présenter lui-aussi des excitations de spin. Son moment magnétique est comparable à celui du cobalt propre, il présente aussi un axe de magnétisation difficile hors-plan, mais son énergie d'anisotropie magnétique, sensiblement plus basse, est de  $1.7 \pm 0.05$  meV. Les deux autres hydruures ne présentent que des excitations d'origine vibratoire. L'effet de l'hydrogène sur les propriétés magnétiques d'adatoms métalliques est donc très important dans ce système aussi, et devra être pris en considération dans les études futures, l'hydrogène étant un contaminant extrêmement commun dans les systèmes sous ultra-haut vide.

Finale­ment, une étude détaillée de la structure de monocouches et bicouches de graphène sur Ru(0001) a été réalisée. Deux différents empilements, de type AA et AB, ont été identifiés pour la deuxième couche, le dernier n'ayant pas encore été observé à ce jour pour ce système. La structure des moirés de la monocouche de graphène et de ce dernier empilement a été déterminée :  $(11.57 \times 11.57) \text{ R}4.3^\circ$  et  $(10.54 \times 10.54) \text{ R}4.7^\circ$ , respec­tive­ment. De plus, les distorsions des liaisons C-C de plus de 10% observées dans les images STM ont été étudiées en détail. Une comparaison quantitative avec des calculs *ab initio* a permis de relier leur origine à l'inclinaison des orbitales  $\pi$  du graphène. Ces distorsions sont donc purement arti­ficielles, ce qui constitue un résultat important pour de futures études du graphène basées sur la microscopie à effet tunnel.

**Mots clés :** microscopie à effet tunnel (STM), microscopie à effet tunnel polarisée en spin (SP-STM), spectroscopie à effet tunnel (STS), spectroscopie à excitations de spin (SES), magnétisme atomique, rémanence magnétique, effet Kondo, atomes isolés, adatoms, cobalt, hydruures, platine, graphène, ruthénium.

# Sommario

Questa tesi tratta le proprietà magnetiche di singoli atomi e di composti idrogenati di metalli di transizione adsorbiti su superfici monocristalline. Si tratta di uno studio sperimentale, sulla base di microscopia a scansione per effetto tunnel (STM), il cui punto di partenza è il tentativo di dimostrare l'esistenza di rimanenza magnetica per singoli atomi adsorbiti (adatom). Le misure sono state effettuate utilizzando un microscopio a effetto tunnel operante a 0.4 K e dotato di bobine superconduttrici in grado di fornire campi magnetici fino a 8.5 T. I sistemi studiati sono atomi di cobalto, puri e idrogenati (idruri di cobalto), adsorbito su superfici di Pt(111) e di grafene su Pt(111).

Nel primo caso, siamo stati immediatamente di fronte alla presenza di idruri di cobalto sulla superficie. Tre tipi di idruri ( $\text{CoH}$ ,  $\text{CoH}_2$  e  $\text{CoH}_3$ ) sono stati identificati, facilmente distinguibili dagli adatom puliti mediante misure di spettroscopia a scansione per effetto tunnel (STS). Due di questi idruri mostrano modi vibrazionali di bassa energia (1 – 30 meV), come tali identificati grazie alla loro mancata risposta ad un campo magnetico, all'effetto della sostituzione isotopica, e al confronto con sistemi noti. I tre idruri possono essere deprotonati applicando una opportuna tensione tra punta e campione.  $\text{CoH}_2$  su Pt(111) presenta una risonanza Kondo generata da uno spin semi-intero ( $S = 3/2$ ) e un particolare anisotropia magnetica. Questo sistema è la prima dimostrazione del verificarsi dell'effetto Kondo come conseguenza dell'adsorbimento di idrogeno. Vengono infine presentati e discussi diversi tentativi effettuati con lo scopo di osservare rimanenza per singoli adatom di cobalto su Pt(111) mediante microscopia a effetto tunnel polarizzata di spin (SP-STM).

Il secondo sistema differisce dal primo per la presenza di uno strato di grafene sulla superficie di Pt(111). La prima determinazione sperimentale del momento magnetico e l'anisotropia magnetica di adatom su grafene è riportata in questa tesi. Abbiamo misurato un momento magnetico di  $(2.2 \pm 0.4) \mu_B$  mediante la spettroscopia di eccitazioni di spin (SES), e un asse di magnetizzazione difficile, con un'energia dell'anisotropia magnetica di  $8.1 \pm 0.4$  meV. Quest'ultimo valore, paragonabile al record detenuto da singoli atomi di Co su Pt(111), è stato attribuito principalmente alla forte ibridazione tra cobalto e grafene. Calcoli *ab initio* confermano le nostre osservazioni. Il grafene è quindi un substrato molto promettente per future applicazioni nei campi di spintronica e nanomagnetismo.

Anche questo sistema presenta tre differenti idruri oltre agli atomi di cobalto puliti. La loro composizione chimica,  $\text{CoH}$ ,  $\text{CoH}_2$  e  $\text{CoH}_3$  è stata determinata confrontando immagini di microscopia a effetto tunnel ad alta risoluzione con immagini simulate di strutture atomiche calcolate *ab initio*. Un metodo di deprotonazione controllata è presentato.  $\text{CoH}_3$  è il solo

---

idruri a presentare eccitazioni di spin. Il suo momento magnetico è paragonabile a quello del cobalto pulito, presenta anch'esso un asse di magnetizzazione difficile fuori dal piano, ma la sua anisotropia magnetica è notevolmente inferiore,  $1.7 \pm 0.05$  meV. Gli altri due idruri mostrano solo eccitazioni di origine vibrazionale. Essendo l'idrogeno un contaminante molto comune nei sistemi di ultra-alto vuoto, il suo effetto sulle proprietà magnetiche di adatom metallaci su grafene è molto importante, e deve essere considerato in studi futuri.

Infine, uno studio dettagliato della struttura del monostrato e doppio strato di grafene su Ru(0001) è stato eseguito. Due impilamenti diversi, AB e AA, sono stati identificati tra il primo ed il secondo strato, l'ultimo dei quali non era ancora stato osservato per questo sistema. Le strutture moiré del grafene monostrato e di quest'ultimo impilamento sono stati determinati :  $(11.57 \times 11.57) R4.3^\circ$  e  $(10.54 \times 10.54) R4.7^\circ$ , rispettivamente. Inoltre, le distorsioni dei legami C-C di oltre il 10% osservate in immagini STM sono stati studiate in dettaglio. Un confronto quantitativo con i calcoli *ab initio* ha legato la loro origine alla inclinazione degli orbitali  $\pi$  del grafene, dimostrando come queste distorsioni siano puramente artificiali. Questo risultato è importante per gli studi futuri del graphene basati sulla microscopia a effetto tunnel.

**Parole chiave :** microscopia a scansione per effetto tunnel (STM), microscopia a effetto tunnel polarizzata di spin (SP-STM), spettroscopia a effetto tunnel (STS), spin-eccitazione spettroscopia (SES), magnetismo atomico, rimanenza magnetica, effetto Kondo, singoli atomi, adatom, cobalto, idruri, platino, grafene, rutenio.

# Zusammenfassung

Die vorliegende experimentelle Studie befasst sich mit der Erforschung der magnetischen Eigenschaften einzelner Übergangsmetall-Atome und Moleküle auf Kristalloberflächen. Die Experimente wurden mit einem Rastertunnelmikroskop (STM) durchgeführt. Die Ausgangsmotivation bestand aus der zentralen Frage, ob der Nachweis einer Remanenz für einzelne adsorbierte Atome (Adatome) gelänge. Der Schwerpunkt der Studie liegt auf der Charakterisierung einzelner Kobaltatome auf den Oberflächen von Pt(111) und Graphen auf Pt(111), in reinem und hydriertem Zustand (Kobalt-Hydrid). Alle Messungen wurden bei Tieftemperaturen bis hinunter zu 0.4 K und unter dem Einfluss magnetischer Felder bis 8.5 T durchgeführt. Im ersten Teil dieser Arbeit behandeln wir die Eigenschaften von Kobalt und dessen Hydriden auf der Oberfläche von Pt(111). Drei Arten von Hydriden ( $\text{CoH}$ ,  $\text{CoH}_2$ , und  $\text{CoH}_3$ ) wurden beobachtet, wovon sich jedes durch seine charakteristische Signatur in Tunnel-Spektren (STS) identifizieren ließ. Zwei dieser Hydride zeigen Niedrigenergie-Schwingungsmoden (1 – 30 meV), welche unabhängig von der angelegten magnetischen Feldstärke sind, und durch Isotopensubstitution sowie dem Vergleich mit bekannten Systemen identifiziert wurden. Alle drei Hydride konnten durch einen wohldefinierten Spannungspuls mit Hilfe der Tunnelspitze deprotoniert werden.  $\text{CoH}_2$  auf Pt(111) zeigt eine Kondo-Resonanz aufgrund seines halbzahligen Spins ( $S=3/2$ ) und seiner magnetischen Anisotropie. Die vorliegenden Resultate sind der erste Nachweis eines Kondo-Systems welches sich durch Wasserstoffadsorption entwickelt. Unsere Ansätze die Remanenz einzelner Kobalt Atome auf Pt(111) mittels spin-polarisierter Rastertunnelmikroskopie (SP-STM) zu beobachten vorgestellt und diskutiert.

Das zweite System unterscheidet sich vom ersten durch eine zusätzliche Lage Graphen auf der Platinoberfläche. Wir präsentieren an dieser Stelle die erste experimentelle Bestimmung des magnetischen Moments und der magnetischen Anisotropie von Kobalt-Adatomen auf Graphen. Ein magnetisches Moment von  $(2.2 \pm 0.4) \mu_B$  wurde durch Spin-Anregungs-Spektroskopie (SES) gemessen. Des Weiteren konnten wir eine Anisotropie-Energie von  $8.1 \pm 0.4$  meV ableiten. Dieser Wert ist vergleichbar mit dem aktuellen Rekord von Kobalt auf Pt(111). Im vorliegenden Fall wird diese Anisotropie-Energie hauptsächlich auf die starke Hybridisierung zwischen Kobalt und Graphen zurückgeführt. Begleitende *ab initio* Berechnungen bestätigen unsere Beobachtungen. Graphen stellt somit ein äußerst vielversprechendes Substrat für zukünftige Anwendungen im Bereich des Nano-Magnetismus und der Spintronik dar.

Wir konnten neben den Kobalt-Atomen in diesem System ebenso drei verschiedene Kobalt Hydride charakterisieren. Ihre jeweilige chemische Zusammensetzung,  $\text{CoH}$ ,  $\text{CoH}_2$  und

CoH<sub>3</sub>, wurde durch direkten Vergleich zwischen hochauflösenden STM-Bildern und simulierten Bildern atomarer Strukturen bestimmt. CoH<sub>3</sub> ist das einzige Hydrid welches Spin-Anregungen zeigt. Sein magnetisches Moment ist mit jenem des reinen Kobalt-Atoms vergleichbar. CoH<sub>3</sub> verfügt ebenso über eine Harte-Magnetisierungsachse, allerdings ist seine magnetische Anisotropie-Energie deutlich niedriger,  $1.7 \pm 0.05$  meV. Die beiden anderen Hydride zeigen jeweils nur Schwingungsanregungen. Der Einfluss von Wasserstoff auf die magnetischen Eigenschaften von Metall-Atomen ist folglich auch in diesem System sehr stark. Zukünftige Studien müssen diesen Umstand berücksichtigen, da Wasserstoff eine stets anwesende Komponente des Restgases in Ultrahochvakuum-Anlagen ist.

Schließlich wurde eine detaillierte Untersuchung der Graphen-Struktur von Mono- und Doppelschichten auf Ru(0001) durchgeführt. Es wurden zwei unterschiedliche Stapelfolgen für die Doppelschichten identifiziert. Zum einen die Folge AB, zum anderen die Folge AA. Letztere wurde erstmals im Rahmen dieser Arbeit beobachtet. Die moiré Strukturen der Graphen-Monolage und jener Doppellage mit Stapelfolge AA wurden bestimmt:  $(11.57 \times 11.57) R4.3^\circ$  beziehungsweise  $(10.54 \times 10.54) R4.7^\circ$ . Darüber hinaus wurde geklärt weshalb CC-Bindung in STM Aufnahmen mit einer Streckung von mehr als 10% abgebildet werden. Ein quantitativer Vergleich mit *ab initio* Berechnungen erlaubt es diese scheinbare Streckung auf die Neigung der Graphen  $\pi$ -Orbitale zurückzuführen. Die Streckungen sind somit rein künstlich. Dieser Zusammenhang ist von grosser Bedeutung bei der Interpretation zukünftiger Rastertunnelmikroskopie Studien von Graphen.

**Schlüsselwörter:** Rastertunnelmikroskopie (STM), Spin-polarisierte Rastertunnelmikroskopie (SP-STM), Rastertunnelspektroskopie (STS), Spin-Anregungs-Spektroskopie (SES), atomarer Magnetismus, magnetische Remanenz, Kondo-Effekt, einzelner Atome, Adatome, Kobalt, Hydride, Platin, Graphen, Ruthenium.

# Contents

<b>Abstract (English/Français/Italiano/Deutsch)</b>	<b>iii</b>
<b>List of figures</b>	<b>xiii</b>
<b>1 Introduction</b>	<b>1</b>
<b>2 Methods</b>	<b>5</b>
2.1 Scanning Tunneling Microscopy . . . . .	5
2.2 Simple theory of STM . . . . .	6
2.3 Spin-polarized STM . . . . .	8
2.4 Inelastic Electron Tunneling Spectroscopy . . . . .	10
2.5 Improving our ultralow-temperature STM set-up . . . . .	11
2.5.1 Presentation of the ultralow-temperature STM . . . . .	11
2.5.2 Modifications of the set-up . . . . .	14
<b>3 Single atom magnetism</b>	<b>19</b>
3.1 Magnetism of a free atom . . . . .	19
3.2 Magnetism in solids: a very brief overview . . . . .	21
3.3 Magnetism of adsorbed atoms: an intermediate case . . . . .	22
3.4 Spin-Excitation Spectroscopy: probing magnetic excitations with the STM . . .	25
3.5 A particular case: the Kondo effect . . . . .	27
<b>4 Co and Co-hydrides on Pt(111): an attempt at discovering single-adatom magnetic remanence, and an unexpected Kondo effect</b>	<b>33</b>
4.1 Co and Co hydrides on Pt(111) . . . . .	34
4.1.1 Switching types with voltage pulses and exposure to H <sub>2</sub> . . . . .	37
4.1.2 Isotopic substitution . . . . .	39
4.1.3 Temperature dependence . . . . .	40
4.1.4 Effect of an out-of-plane magnetic field . . . . .	43
4.2 Magnetic remanence in single adatoms . . . . .	47
<b>5 Co and Co-hydrides on graphene on Pt(111)</b>	<b>51</b>
5.1 Graphene/Pt(111): preparation and observations . . . . .	52
5.2 Co/G/Pt(111): four types of complexes . . . . .	52
5.3 Co/G/Pt(111): Magnetic properties . . . . .	58

## Contents

---

5.4	CoH <sub>x</sub> ( $x=1,2,3$ ): vibrational and magnetic properties . . . . .	61
<b>6</b>	<b>Mono- and bilayer graphene on Ru(0001): Structure, stacking, and distortions</b>	<b>65</b>
6.1	Two different stackings for bilayer graphene/Ru(0001) . . . . .	66
6.2	Structure of monolayer and flat bilayer graphene on Ru(0001) . . . . .	70
6.3	Apparent distortions in graphene on Ru(0001) . . . . .	73
6.3.1	Shortening factor in the 2D-projected C-C distances . . . . .	76
6.3.2	DFT calculations of the structure . . . . .	77
6.3.3	Directionality of the $\pi$ -orbitals of graphene and corrugation . . . . .	78
6.3.4	Apparent distortions in 2 ML graphene . . . . .	78
6.3.5	DFT-simulated STM images . . . . .	80
<b>7</b>	<b>Conclusion and outlook</b>	<b>83</b>
	<b>Bibliography</b>	<b>87</b>
	<b>Acknowledgements</b>	<b>99</b>
	<b>Curriculum Vitae</b>	<b>101</b>



# List of Figures

2.1	Schematic representation of quantum tunneling of electrons between two electrodes . . . . .	6
2.2	Schematic representation of spin-polarized quantum tunneling . . . . .	9
2.3	Schematic representation of inelastic quantum tunneling . . . . .	10
2.4	Photograph of the ultralow-temperature STM set-up . . . . .	12
2.5	Schematic of the $^3\text{He}$ cryostat . . . . .	13
2.6	3D model and photographs of the STM . . . . .	14
2.7	3D model of the new tip-holder design . . . . .	16
3.1	Schematic representation of the energy position of the different $m_S$ states of a $S = 3$ system with uniaxial anisotropy . . . . .	23
3.2	Schematic representation of the evolution of the magnetic states of a uniaxially-anisotropic spin-3/2 system with $D = 0.5$ meV and an isotropic g-factor of 2 . .	24
3.3	Energy of the magnetic states of a fully anisotropic spin-3/2 system with $D = 0.5$ meV, $E = 0.25$ and an isotropic g-factor of 2 . . . . .	25
3.4	Schematic representation of the Kondo magnetic screening process . . . . .	28
3.5	Fano functions . . . . .	30
3.6	Temperature dependence of the width and amplitude of a Kondo resonance . .	31
4.1	Co/Pt(111): STM image and STS spectra for clean Co adatoms . . . . .	35
4.2	STS spectra of two Co-related complexes . . . . .	36
4.3	Effect of $\text{H}_2$ exposure and voltage on Co-related complexes . . . . .	37
4.4	Deprotonation voltage versus current . . . . .	38
4.5	H-saturated Co complexes on Pt(111) . . . . .	39
4.6	Effect of $\text{D}_2$ exposure on type 2 Co complexes . . . . .	40
4.7	STS spectra for $\text{CoH}_2$ versus temperature . . . . .	41
4.8	Intrinsic width and height of the Kondo resonance versus temperature . . . . .	42
4.9	$\text{CoH}$ versus magnetic field . . . . .	44
4.10	$\text{CoH}_2$ versus magnetic field: a spin-3/2 Kondo system . . . . .	44
4.11	Modelling the splitting with magnetic field of the Kondo resonance . . . . .	46
4.12	SP-STM on bilayer Co islands and Co adatoms . . . . .	48
4.13	Height distribution of Co adatoms with a spin-polarized STM tip . . . . .	49
5.1	Four different moiré patterns for graphene/Pt(111) . . . . .	53

## List of Figures

---

5.2	Four different types of Co complexes on graphene, distinguishable by their apparent height and STS features . . . . .	54
5.3	Statistical distribution of the four types of Co complexes on G/Pt(111) . . . . .	55
5.4	H-desorption threshold voltages versus current . . . . .	55
5.5	High-resolution STM images and simulations yielding the chemical composition of each Co-related type . . . . .	56
5.6	Clean Co atoms adsorbed on graphene/Pt(111) . . . . .	57
5.7	Comparison between the appearance of Co adatoms on graphene and on Pt(111) . . . . .	57
5.8	Magnetic moment and anisotropy of Co atoms on graphene . . . . .	59
5.9	Calculation of the magnetic moment of Co versus graphene - Pt distance . . . . .	60
5.10	CoH and CoH <sub>2</sub> /G/Pt(111) vs magnetic field . . . . .	61
5.11	CoH <sub>3</sub> /G/Pt(111): spin-excitations . . . . .	62
6.1	Graphene mono- and bilayers on Ru(0001): appearance and profile . . . . .	67
6.2	Mono- and flat bilayer graphene frontier . . . . .	68
6.3	Two differently-stacked second graphene layers on graphene/Ru(0001) . . . . .	69
6.4	Moiré patterns of mono- and bilayer graphene on Ru(0001) . . . . .	71
6.5	Structural analysis of mono- and bilayer graphene in the reciprocal space . . . . .	72
6.6	Construction of the C-C bond length map . . . . .	74
6.7	Apparent lattice distortions in 1 ML . . . . .	75
6.8	2D-projection shortening factor . . . . .	77
6.9	The directionality of the $\pi$ -orbitals as the origin of the distortions . . . . .	79
6.10	Apparent lattice distortions in 2 ML . . . . .	80
6.11	C positions versus ring centres . . . . .	81

# 1 Introduction

Magnetism has been known, studied and exploited for millennia. Progress in atomic physics over the last century, with the birth of quantum mechanics, allowed mankind to track its origin down to the very electrons of the atoms constituting magnetic materials. Yet a very simple question remains: how small can a magnet be? Let us formulate the problem in a different way: A magnet is an object that produces a magnetic field, with field lines curling in space from a north to a south pole. Most people know that cutting a magnet in two always results in two magnets, each with its own pair of north and south poles. The question is the following: if we kept cutting our magnet into halves down to the ultimate limit of a single atom, could it possibly still be a magnet, with fixed north and south poles?

Of course, in this simple case, the answer is known: a single atom in free space is isotropic, its electronic orbitals, responsible for magnetism, have no preferential direction. Consequently, this system cannot be considered as a magnet according to our definition. But what about a single atom adsorbed on a surface, a so-called "adatom"? Its electronic orbitals are affected by those of the substrate, giving rise to magnetic anisotropy. Could this anisotropy block the magnetic moment of a single adatom in space and time – a property called "magnetic remanence" – thus yielding a single-adatom magnet? That is the very exciting question that initiated this thesis work, which is more generally concerned with the magnetic properties of single adatoms and adsorption complexes, as well as with relevant surfaces in the field of nanoscale magnetism.

## Chapter 1. Introduction

---

But first and foremost, how does one gain access to an adatom? How can one probe its magnetic properties? **Chapter 2** provides an answer to this question, discussing the capabilities of the Scanning Tunneling Microscope (STM), an instrument of choice owing to its spatial resolution, high sensitivity, versatility, and non-invasive character. Its principle of operation is explained, and Spin-Polarized STM (SP-STM), Scanning Tunneling Spectroscopy (STS), and Inelastic Electron Tunneling Spectroscopy (IETS) are introduced. Finally, our own STM set-up is briefly described, and the improvements that have been made to the initial set-up are presented.

**Chapter 3** contains a very condensed summary of atomic magnetism starting from basic quantum mechanics. It focuses on the particular case of transition metal adatoms on non-magnetic surfaces. The concept of magnetic excitations and the related STM technique of Spin-Excitation Spectroscopy (SES) are then introduced, and the main achievements of this relatively new technique in the field of nanoscale magnetism are reviewed. Finally, the very peculiar Kondo effect, arising from strong electronic correlations between adatom and substrate, and frequently encountered in magnetic adatoms systems, is presented and explained in a simple picture.

The next three chapters deal with experimental results obtained with STM for magnetic adatoms and magnetically relevant systems:

**Chapter 4** treats of single Co adatoms on Pt(111). We begin by explaining why we chose this system in the prospect of demonstrating magnetic remanence in adatoms. We then provide a thorough characterization of the system, which turned out to contain not only Co adatoms, but also three different Co-hydrides. Their chemical composition, vibrational modes and magnetic properties are exposed. One of them exhibits a very clear Kondo effect. The implications of this observation on the magnetic properties of the system are explained in detail. Finally, we provide an overview of our progress regarding our initial objective, observing magnetic remanence with SP-STM in this system.

**Chapter 5** concerns a novel system: it presents the very first experimental determination of the magnetic properties of magnetic adatoms on graphene. Graphene, arguably the most promising and investigated material these days, is indeed remarkable in many aspects, due to its two-dimensional honeycomb structure of C atoms. Its exceptional electronic properties, mainly characterized by a linear and gapless dispersion of charge carriers, have also been predicted to qualify it as an exceptional substrate for magnetic adatoms. This is what we verified experimentally, in the precise case of Co adatoms deposited on graphene grown on Pt(111). Similarly to Co/Pt(111), pure Co adatoms as well as three Co-hydrides were identified and fully characterized. Two of them display large vibrational features, while the last one exhibits a magnetic behaviour comparable to that of clean Co and a much lower magnetic anisotropy.

---

**Chapter 6** provides an in-depth structural characterization of graphene (G) on Ru(0001). Since the importance of graphene regarding nanoscale magnetism has been demonstrated in the previous chapter, a detailed analysis of the structure of this system deserves its place in this thesis. G/Ru(0001) is technically more relevant than G/Pt(111) due to its far superior uniformity and quality. Graphene bilayers on Ru(0001) are found to stack in two different ways: one, the Bernal or AB stacking, which was already reported, the other, the AA stacking, which has not been reported yet for this system. The precise structure of monolayer graphene and of AA-stacked bilayer graphene on Ru(0001) is shown to be directly accessible with high-resolution STM images. For the first time, the issue of large distortions of the honeycomb mesh observed in the STM images is addressed quantitatively by comparison with first-principle calculations.

Finally, we conclude on the different achievements of this work, and their implications for future studies in the field of atomic and nanoscale magnetism, graphene, and nanotechnology.



## 2 Methods

### 2.1 Scanning Tunneling Microscopy

The Scanning Tunneling Microscope granted the Nobel Prize in Physics 1986 to its inventors, G. Binnig and H. Rohrer, while working at the IBM Research Laboratory in Rüschlikon, Switzerland [1, 2]. It relies on quantum tunneling of electrons between two electrodes separated by an insulator (typically vacuum or air). The first electrode, an atomically-sharp conducting tip, lies at a distance  $z$  in the nanometre range away from the second one, which would be the surface of the sample under study. Upon application of a voltage between the two electrodes, called "bias voltage"  $V$ , a tunnel current of electrons  $I$  establishes, as illustrated in figure 2.1.

The basic idea behind scanning tunneling microscopy is that the tunnel current  $I$  depends exponentially on the tip-sample distance  $z$ , and is thus dominated by the apex of the tip (the last atom for an atomically sharp tip). Therefore scanning the tip over the sample and at a constant distance allows one to reconstruct the topography of the surface (thus a microscopy image) from the tunnel current with a resolution of the order of the size of a single atom. This mode of image acquisition is called the constant-height mode. However, the roughness or inclination of the sample surface can lead to loss of the tunnel current when the tip-sample distance exceeds the detection limit of the apparatus, and to tip and/or sample damage when the tip is too close to the surface. It is therefore usually more convenient to perform STM in the constant-current mode, where as the name indicates, the current  $I$  is kept constant while scanning. This can be done automatically at a relatively fast speed using an electronic feedback loop taking  $I$  as an input and acting on an actuator controlling  $z$  with a precision typically in the picometre range. To grant both such a precision and fast response to this  $z$  actuator and the scan  $x$  and  $y$  actuators, they are usually made of piezoelectric elements. However, micro-electromechanical systems (MEMS) have recently been demonstrated as an interesting alternative, notably for high-speed applications (video-STM) [3].

It is important to note that STM is more than an atomic-scale probe: it also has the capability to displace adatoms and molecules over a surface in a controlled way [4, 5], and therefore assemble nanostructures with atomic precision. The possibilities offered by STM-based

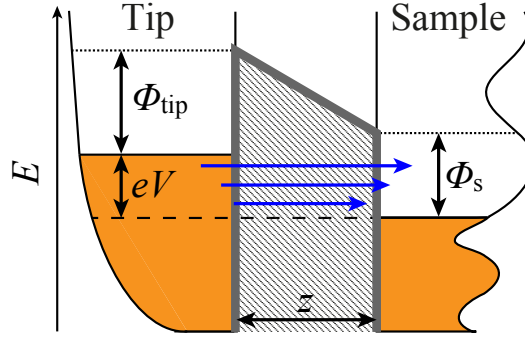


Figure 2.1: Schematic representation of quantum tunneling of electrons from tip (left-hand side) to sample (right-hand side). The orange areas correspond to the occupied states of the tip and surface band structure.  $\Phi_{\text{tip}}$  and  $\Phi_s$  correspond to the tip and sample electron work function, which, together with the tip-sample distance  $z$ , define the energy barrier encountered by the electrons, represented in grey. Upon application of a voltage  $V$  between tip and sample, electrons from the tip lying higher in energy than the Fermi level of the sample are able to tunnel into unoccupied states, as represented by blue arrows.

atomic manipulations range from the realization of clusters of controlled size and geometry to complex, purely artificial structures such as quantum corrals [6], and to the assembly of arbitrary molecular complexes and a completely new surface chemistry [7].

## 2.2 Simple theory of STM

To derive a quantitative expression for the tunnel current, let us start by considering J. Bardeen's time-dependent perturbation approach for infinite planar electrodes [8].<sup>1</sup> It starts by considering the tip and sample electrodes as two separate subsystems, with electronic wavefunctions  $\psi$  and  $\chi$  expanding through the tunnel barrier. The tunneling matrix element  $M$  is defined as:

$$M = \frac{\hbar}{2m} \int_{S_{z_0}} \left( \chi^* \frac{\partial \psi}{\partial z} - \psi \frac{\partial \chi^*}{\partial z} \right) dS \quad (2.1)$$

where  $z$  corresponds to the direction perpendicular to the electrodes, and the integration is carried over a surface  $S_{z_0}$ , separating the two electrodes at a distance  $z_0$  (the results should be independent of the peculiar position  $z_0$  as long as it lies in between the electrodes).

The Fermi golden rule yields the probability  $w$  for an electron in state  $\psi$  with an energy  $E_\psi$  to tunnel into state  $\chi$  at the energy  $E_\chi$ :

$$w = \frac{2\pi}{\hbar} |M|^2 \delta(E_\psi - E_\chi) \quad (2.2)$$

<sup>1</sup>This section is based on [9], to which the reader is referred for more details on the historical and theoretical aspects of the STM.



with  $\delta$  the Dirac delta function, restricting tunneling to tip and sample electronic states with the same energy (elastic tunneling).

The tunnel current is obtained by summing this probability (multiplied by the elementary charge carried by each electron) over all the relevant states:

$$I = \frac{4\pi e}{\hbar} \int_{-\infty}^{+\infty} [f(E_F - eV + \epsilon) - f(E_F + \epsilon)] \times \rho_S(E_F - eV + \epsilon) \rho_T(E_F + \epsilon) |M|^2 d\epsilon \quad (2.3)$$

$V$  is the voltage difference between sample and tip, and  $f$  is the Fermi-Dirac distribution function, defined as

$$f(E) = \left( 1 + e^{\frac{E - E_F}{k_B T}} \right)^{-1} \quad (2.4)$$

and  $\rho_T$  and  $\rho_S$  are the density of states (DOS) of the tip and sample, respectively. The Fermi distribution function can usually be approximated by a simple step function, provided that the thermal energy  $k_B T$  is smaller than the energy resolution of the measurement. Bardeen showed that  $|M|$  can actually be treated as a constant for the small energy differences involved [8]. Equation 2.3 thus simplifies into the well-known Bardeen formula for the tunnel current:

$$I \propto \int_0^{eV} \rho_S(E_F - eV + \epsilon) \rho_T(E_F + \epsilon) d\epsilon \quad (2.5)$$

which is nothing else than the convolution of the DOS of the two electrodes.

In this simple model of two infinite planar electrodes, the differential conductance is

$$dI/dV \propto \rho_S(E_F - eV) \rho_T(E_F) \quad (2.6)$$

The measurement of  $dI/dV$  as a function of  $V$  is called Scanning Tunneling Spectroscopy (STS), and is usually done with a tip having a DOS as constant as possible in the voltage range of the spectrum, so that the observed signal is, to a good approximation, proportional to the DOS of the sample right below the tip.

J. Tersoff and D. R. Hamann later refined Bardeen's model taking into account the finite curvature of the tip [10, 11]. Assuming a spherical tip apex with radius  $R$ , and retaining only the  $s$ -wave solutions of the Schrödinger equation for a spherical potential well as the tip wavefunctions, they derived the following expression for the tunnel current at low bias:

$$I \propto \sum_{E_\mu = E_F - eV}^{E_F} |\psi_\mu(\vec{r}_0)|^2 = eV \rho_S(\vec{r}_0, E_F) \quad (2.7)$$

where  $\vec{r}_0$  is the position of the centre of curvature of the tip. In this model, the tip DOS has been taken out of the problem, and the current is simply proportional to the sample local DOS, or "LDOS", at the centre of curvature of the tip. For free electron metal samples, where

the LDOS contours at a distance from the surface almost coincide with the contours of the total electron density, mapping the surface at a constant current therefore yields the surface charge-density contours. This model has proven very useful for simulating STM images of metallic surfaces.<sup>2</sup>

### 2.3 Spin-polarized STM

The basic idea behind Spin-polarized STM (SP-STM) [12, 13, 14] is to add magnetic sensitivity to the high spatial resolution of the STM using a magnetic tip, or more precisely, a tip that exhibits a different DOS for spin-up and spin-down electrons at the Fermi level,  $\rho_T^\uparrow(E_F)$  and  $\rho_T^\downarrow(E_F)$  respectively, noted  $n_T^\uparrow$  and  $n_T^\downarrow$  for simplicity.<sup>3</sup> The key element of SP-STM is that the spin of an electron undergoing elastic tunneling must be conserved. Consequently, if the tip and sample are magnetized along the same axis, the problem can be separated into two independent parts, the DOS of spin-up (respectively spin-down) electrons yielding a current of purely spin-up (spin-down) electrons, as proposed by M. Julliere [15]. Adopting the same notation for the spin-polarized LDOS of the sample at the Fermi level, the conductivity at zero bias corresponds to:

$$\frac{dI}{dV} \propto n_S^\uparrow n_T^\uparrow + n_S^\downarrow n_T^\downarrow \quad (2.8)$$

For the more general case of non-parallel tip and sample magnetization direction, we can write:<sup>4</sup>

$$\frac{dI}{dV} \propto n_S^\uparrow n_T^\uparrow |M_{\uparrow\uparrow}|^2 + n_S^\downarrow n_T^\downarrow |M_{\downarrow\downarrow}|^2 + n_S^\downarrow n_T^\uparrow |M_{\downarrow\uparrow}|^2 + n_S^\uparrow n_T^\downarrow |M_{\uparrow\downarrow}|^2 \quad (2.9)$$

where  $M_{\sigma_1\sigma_2}$ ,  $\sigma_i \in \{\uparrow, \downarrow\}$  are the spin-resolved tunneling matrix elements.

Simply defining the total DOS at the Fermi level of tip and sample as  $n_{T,S} = n_{T,S}^\uparrow + n_{T,S}^\downarrow$ , and their respective spin polarization at the Fermi level as

$$P_{T,S} = \frac{n_{T,S}^\uparrow - n_{T,S}^\downarrow}{n_{T,S}} \quad (2.10)$$

it can be shown that equation 2.9 for the spin-polarized conductance is equivalent to

$$\frac{dI}{dV} \propto n_S n_T (1 + P_S P_T \cos \theta) \quad (2.11)$$

---

<sup>2</sup>Please note that this model fails to reproduce atomic resolution images of metallic surfaces, due to the lateral extent of the assumed  $s$  orbital. In that case, different, more localized orbitals are believed to be responsible for the high lateral resolution.

<sup>3</sup>The up and down directions are defined with respect to the quantization direction of the tip magnetization.

<sup>4</sup>This section is mainly based on [14], to which the reader is referred for further details. Please also note that the expressions derived in this section rely on the approximation that tunneling only occurs between the respective Fermi levels of tip and sample, and therefore only apply to small bias voltages. A more general expression can be found in [16].

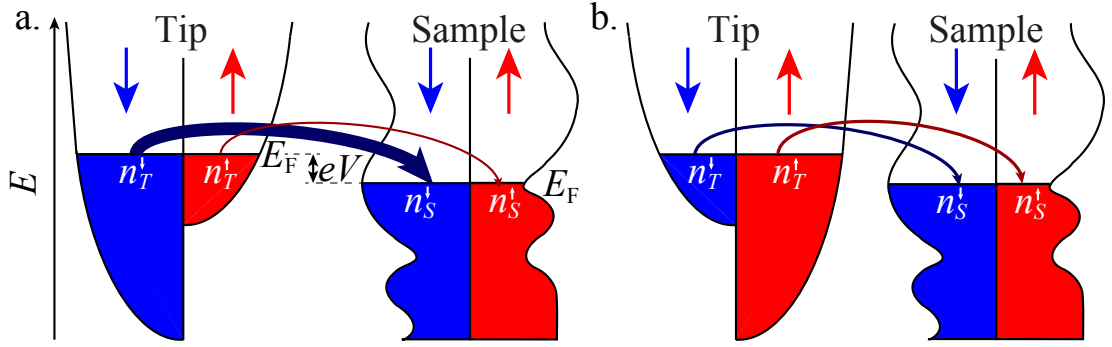


Figure 2.2: Schematic representation of quantum tunneling from a tip to a sample, both being spin-polarized at their respective Fermi level. **a.** Tip and sample are polarized parallel, a large current of majority (spin-down in this case) electrons can build up, leading to a high total tip-sample current  $I_{\uparrow\uparrow}$ . **b.** Tip and sample are polarized anti-parallel, both currents of spin-up and down electrons are low. In this case the total current  $I_{\uparrow\downarrow}$  is low.

with  $\theta$  the angle between the tip and sample magnetization direction. It becomes clear that the conductance, and thus the current, can be separated into a constant part and a spin-polarized part, which is positive if the scalar product of the tip and sample magnetization is positive ("parallel" case, the current is then simply noted  $I_{\uparrow\uparrow}$ ), and negative in the opposite case ("anti-parallel" case, the lower current is noted  $I_{\uparrow\downarrow}$ ). Figure 2.2 illustrates spin-polarized tunneling for parallel and anti-parallel tip and sample magnetization.

An effective polarization  $P$  can be defined for the tunnel junction as  $P = P_S P_T \cos \theta$ . If the sample can be magnetized in the two opposite directions of a single axis, the two possible values for the tunnel current are given by

$$I_{\uparrow\uparrow} = I_0(1 + P) \quad \text{and} \quad I_{\uparrow\downarrow} = I_0(1 - P) \quad (2.12)$$

so that  $P$  can be calculated from the measurement of  $I_{\uparrow\uparrow}$  and  $I_{\uparrow\downarrow}$ :

$$P = \frac{I_{\uparrow\uparrow} - I_{\uparrow\downarrow}}{I_{\uparrow\uparrow} + I_{\uparrow\downarrow}} \quad (2.13)$$

When STM is performed in constant-current mode, the feedback loop will compensate the difference in current over two oppositely magnetized objects with a different tip-sample distance  $\Delta z$ . The effective polarization can be shown to approximately correspond to

$$P = \frac{e^{A\phi\Delta z} - 1}{e^{A\phi\Delta z} + 1} \quad (2.14)$$

with  $\phi$  the tunnel barrier height, and  $A = 1.025 \text{ eV}^{-1/2} \text{ \AA}^{-1}$  [12].

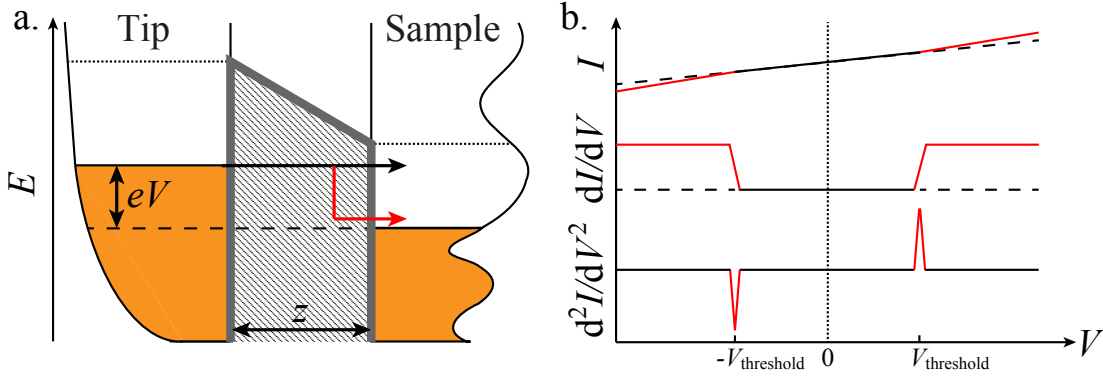


Figure 2.3: **a.** Schematic representation of elastic (black arrow) and inelastic quantum tunneling (red arrow) from tip to sample of an electron with energy  $eV$  above the Fermi level of the sample. **b.** Schematic  $I(V)$ ,  $dI/dV$ , and  $d^2I/dV^2$  curves in the presence of an inelastic tunneling process at energy threshold  $eV_{\text{threshold}}$ . Above this threshold, the effect of inelastic tunneling is evidenced in red, and the dashed lines correspond to purely elastic tunneling.

## 2.4 Inelastic Electron Tunneling Spectroscopy

So far, we have always assumed elastic tunneling of electrons, that is, tunneling from occupied into unoccupied levels with the same energy. However, inelastic tunneling of electrons through an insulator has been demonstrated nearly half a century ago [17], leading to the birth of Inelastic Electron Tunneling Spectroscopy (IETS). Its main application concerns the characterization of molecular vibrational modes. IETS was first demonstrated in an STM set-up for C-H stretch modes of  $\text{C}_2\text{H}_2$  on Cu(100) [18].

Basically, if an electron has enough energy to excite an inelastic process, such as a vibration, and still find an unoccupied state to tunnel into, the differential conductance of the junction will be increased. This translates into a step in  $dI/dV$  at an energy which is characteristic of the inelastic process involved. The situation is symmetric with respect to bias voltage, therefore a second conductance step is observed at the opposite voltage, with same amplitude as the first one. This amplitude corresponds to the probability of the inelastic tunneling process with respect to that of elastic tunneling. A third information, the lifetime of the inelastic excitation, can be obtained from IETS spectra: provided that it is sufficiently short, the Heisenberg uncertainty principle translates it into a broadening of the threshold energy of the excitation. Figure 2.3 illustrates inelastic tunneling and the way it affects  $I$ ,  $dI/dV$ , and  $d^2I/dV^2$ .

In summary, the voltage position of the inelastic features relates to the energy of the excitation, their amplitude to the cross section of the inelastic process, and their width yield a measurement of the lifetime of the excitation. This last statement relies on the assumption that the measured width corresponds to the intrinsic width, what is generally not the case, as will become clear in the following.

IETS signals can be very small signals (several % of the total conductance). In order to maximize the signal to noise ratio,  $dI/dV$  signals are usually acquired directly, instead of recording  $I$  and numerically differentiating it with respect to  $V$ . This is done using the lock-in technique, where a small sinusoidal AC voltage  $V_{\text{mod}} \sin(\omega_{\text{mod}} t)$  is added to the bias voltage  $V$ , and a lock-in amplifier used to record the part of the  $I$  signal that oscillates with the same angular frequency  $\omega_{\text{mod}}$  and an adjustable phase. The chosen frequency is usually higher than the maximal response frequency of the feedback loop so that the added modulation does not affect the position of the STM tip. The effect is twofold: firstly, the measured signal is, to a very good approximation, proportional to  $dI/dV$ , the component of  $I$  at  $\omega_{\text{mod}}$  being the first order term of a Taylor expansion of  $I$ . Secondly, a significant fraction of the noise present in  $I$  can be eliminated by this frequency and phase filtering. Note that  $d^2I/dV^2$  can also be acquired directly, setting the lock-in frequency to  $2\omega_{\text{mod}}$ . This may be particularly useful in the case of extremely small inelastic signals. The inelastic features appear in  $d^2I/dV^2$  as a dip-peak couple (a negative peak on the negative bias side, a positive one on the positive bias side), symmetric with respect to the origin.

Another important aspect of STS and IETS limitations is their energy resolution, which affects both the position and width of the observed features. It is first limited by the measurement temperature, the Fermi-Dirac distribution of electrons in tip and sample DOS introducing a thermal broadening of the measured features, and the amplitude of the voltage modulation introduced in the lock-in technique. It is then usually further decreased by electrical noise coming from various sources.

Although mainly concerned with vibrational modes, IETS also represents an extremely valuable source of information regarding the magnetic properties of adatoms and adsorbed molecules. Indeed, magnetic excitations also represent inelastic processes that can be excited and probed by a tunnel current of electrons. This will be the subject of section 3.4, page 25, in the next chapter.

## 2.5 Improving our ultralow-temperature STM set-up

### 2.5.1 Presentation of the ultralow-temperature STM

The measurements presented here have been carried out with a homebuilt ultrahigh-vacuum (UHV) sub-Kelvin STM equipped with superconducting coils producing magnetic fields from  $-8.5$  to  $+8.5$  T perpendicularly oriented with respect to the sample, and from  $-0.8$  to  $+0.8$  T in one of the surface directions. Figure 2.4 presents a photograph of the whole experimental apparatus.

The cryostat, illustrated in figure 2.5, is based on a commercial closed-circuit single-shot pumped  $^3\text{He}$  cryostat, granting  $\sim 12$  hours of stable measurement conditions at 0.4 K. STM measurements can also be performed at  $\sim 2$  K after condensation and cooling down of  $^3\text{He}$  (without pumping on liquid  $^3\text{He}$ ), 4.5 K (gaseous  $^3\text{He}$  providing thermal contact to the liquid

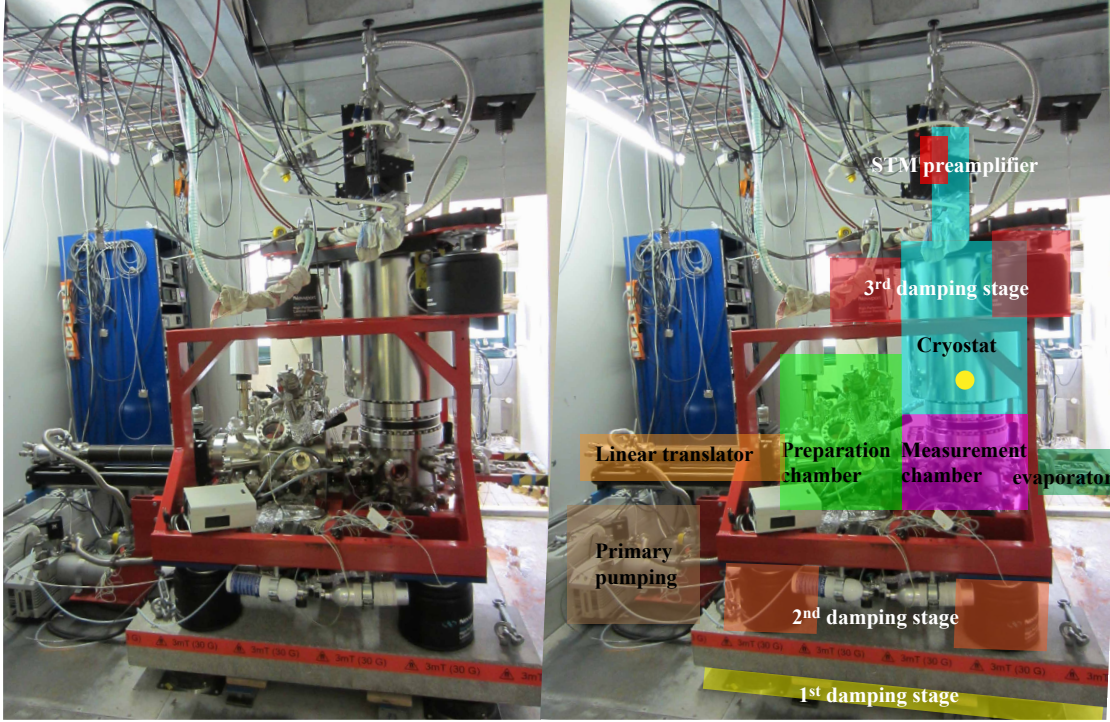


Figure 2.4: Photograph of the ultralow-temperature STM set-up. The main parts of the machine as well as the successive damping stages have been evidenced in the right-hand-side picture. The yellow circle indicates the position of the sample during STM measurements.

$^4\text{He}$  bath), and above using an integrated resistive heater.

The STM, presented in figure 2.6, is rigidly attached to the  $^3\text{He}$  pot of the cryostat, there is therefore no internal vibration insulation. The external vibration damping consists of four parts: the cryostat lies on three laminar flow pneumatic feet which rest on the machine frame. This frame supports all the vacuum chambers and apparatus, and is supported by four similar laminar flow pneumatic feet. These feet sit on a concrete block, which is decoupled from the floor through four basic pneumatic feet. The whole measurement room, including floor and ceiling, is a soundproof Faraday cage.

All the necessary equipment to prepare single crystals (ion sputtering, annealing by electron-bombardment, gas dosing, direct measurement of the sample temperature with a type K thermocouple, characterization of the surface purity with an Auger electron spectrometer), thin films and islands (*e*-beam evaporator, Knudsen cell evaporator, cooling down of the sample down to  $\sim 50$  K with a liquid He flux cryostat), adatoms and small clusters (triple *e*-beam evaporator for *in situ* deposition at temperatures down to 2 K), is available, as well as a carousel to store samples and a fast-entry lock.

This set-up has already been thoroughly described in a former PhD thesis [19]. In the following,

## 2.5. Improving our ultralow-temperature STM set-up

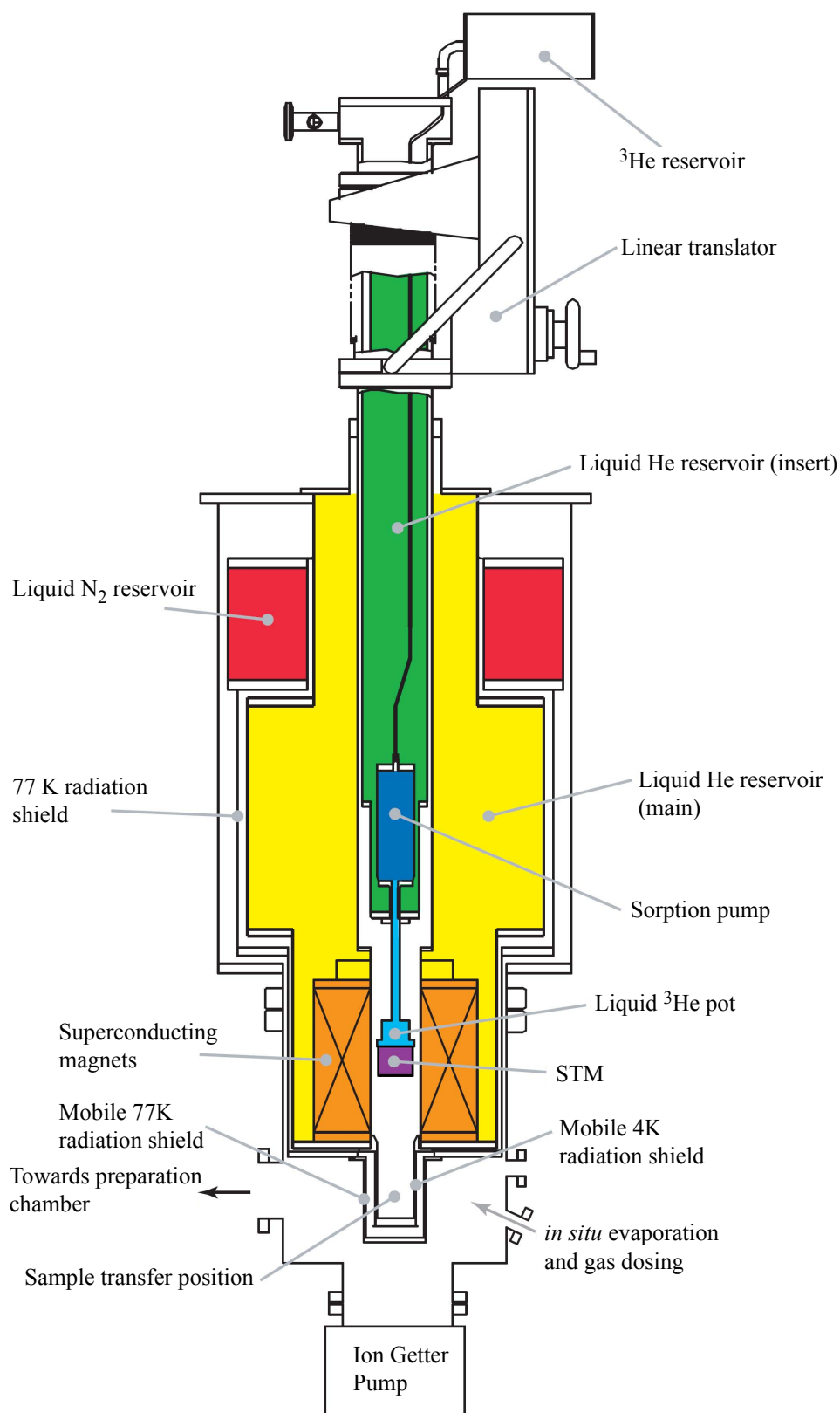


Figure 2.5: Schematic of the  $^3\text{He}$  cryostat, adapted from [19].

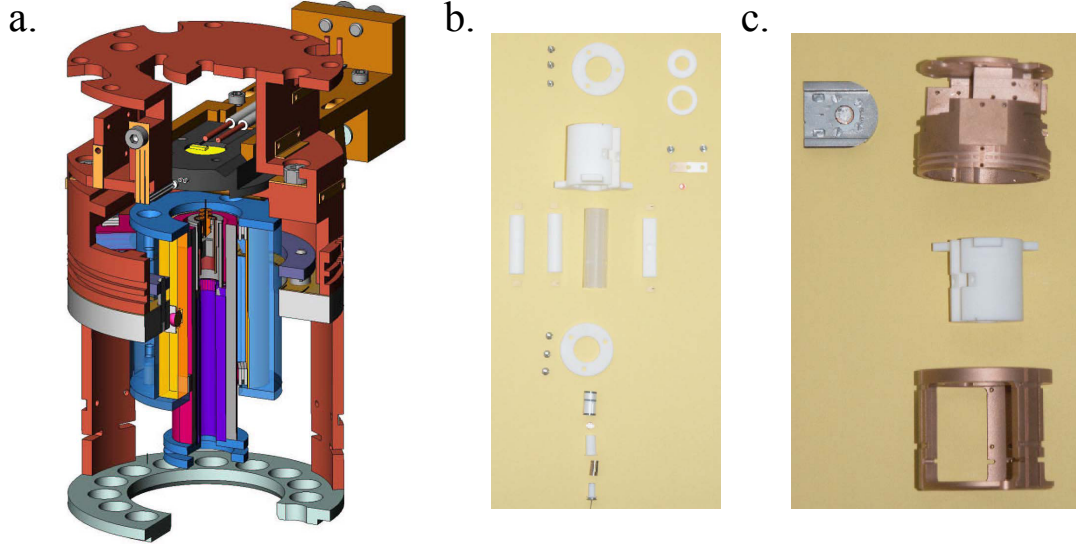


Figure 2.6: **a.** Cross-section view of a 3D model of our STM, with sample-holder and manipulator head. **b.** Disassembled STM head. **c.** Sample-holder (top-left corner), STM cage (top-right and bottom) and STM body (middle).

we will concentrate on the main improvements that have been realized during this thesis work.

### 2.5.2 Modifications of the set-up

First of all, several upgrades have been carried out regarding the vacuum quality of the machine, bringing its base pressure from  $\sim 1 \times 10^{-9}$  to  $\sim 3 \times 10^{-10}$  mbar:

- A connection between the STM UHV chamber and the empty space behind the STM electrical feedthroughs has been added. This volume was previously pumped only through the STM cable channels going through the mobile  $^4\text{He}$  cryostat (insert). We believe that this connection, which had a very low gas conductance especially when the cryostat was at liquid He temperature, did not allow for a good evacuation of the upper volume. Part of the improvement in the base pressure of the STM chamber, as well as the disappearance of the periodic pressure peaks (peaks of  $\sim 1 \times 10^{-9}$  mbar with a period of  $\sim 10$  minutes), have been attributed to this modification.
- Bake-out of the cryostat, and consequently of the STM chamber, is not possible due to the specifications of the superconducting coils and their direct thermal coupling to the walls of the cryostat. A pair of UVC lamps (RBD Instruments) have been added to the STM chamber to perform cold bake-out [20]. The underlying principle is photon-stimulated desorption (PSD) of the water molecules. This modification has improved



## 2.5. Improving our ultralow-temperature STM set-up

---

the base pressure of the STM chamber noticeably, and reduces dramatically the pump-down time when pumping from atmospheric pressure.

- The original diode-type ion getter pump (IGP) of the STM chamber was replaced with a StarCell<sup>®</sup> IGP equipped with a Ti-sublimator (Varian) in order to improve the pumping volume and decrease the H partial pressure in the STM chamber.

Concerning the STM itself, the major upgrade consists in a new design for the tip-holder in order to allow *in situ* STM tip-exchange, and thus, *in situ* tip preparation (*e.g.*, ion sputtering, annealing by electron bombardment, coating of the tip apex with magnetic films) in a near future. The former design required to apply some force on the STM prism (holding the tube scanner and the tip holder) in the *z* direction of the microscope. The required force was sensibly higher than the force provided by the coarse-*z* piezo-elements, preventing one to perform a tip-exchange *in situ* with the single available tool. Moreover, the openings in the radiation shields did not yield a good visual access to the tip-holder while inserting the tip-exchange tool.

In order to keep the possibility to return to the initial design, the new tip-holder was made in two parts: a fixed part that is held inside the tube scanner in the same way as the former tip-holder (*i.e.*, clamped by a CuBe cylindrical spring), and a mobile part that holds the tip, as presented in figure 2.7. The mechanical connection between these two parts is provided by a specially-designed CuBe spring. The mobile tip-holder can be taken out of and put into the fixed part using the tip-exchange tool already implemented in the set-up (wobble stick-mounted fork), applying only small horizontal forces. Furthermore, the openings in the mobile radiation shields have been enlarged in a way to grant visual access to the tip during tip-exchange. This enlargement has been carefully studied in order not to deteriorate the radiation shielding efficiency while the shields are closed.

Furthermore, we removed as many magnetic and superconducting (and so diamagnetic) elements in the STM as possible, in order to improve its stability in magnetic field. The stainless-steel screw that originally held the CuBe wire spring (*I* contact) at the back of the tip-holder was replaced with a Ti one (*I* contact is still achieved through a CuBe spring). The new tip-holder body is also made of Ti instead of Mo as the original tip-holder. Mo undergoes a superconducting transition below 0.92 K, and is thus expected to become strongly diamagnetic when performing measurements at 0.4 K.

The new tip-holder is also completely metallic. Formerly, a Macor<sup>®</sup> cylinder electrically decoupled the CuBe spring (holding the tip-holder inside the scanner) from the tip. This CuBe spring, which was originally designed to be grounded, had been left floating. It is now connected to the tip-holder.

Bias contact to the sample in the STM was originally done with a Cu wire traversing a small cylindrical ceramic. It has been replaced with a Ta piece in a ceramic with the same diameter, yielding a much larger contact surface.

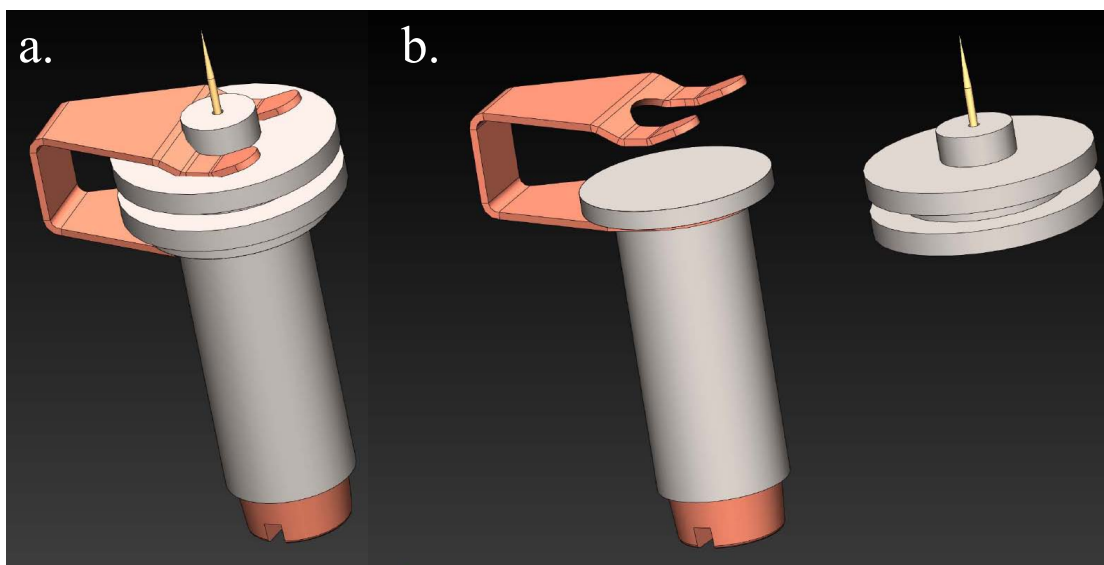


Figure 2.7: **a.** 3D model of the new tip-holder. It consists of a fixed part made of two Ti components screwed into each other, a Ti screw that holds the tunnel current contact, and a CuBe spring. This spring holds the mobile tip-holder, made of Ti as well, and allows for its insertion and extraction using lateral force only. **b.** Same model with the mobile tip-holder out of the fixed part.

Several modifications have also been made on other aspects of the machine, and are listed below:

- The four springs that initially held the whole machine, mechanically decoupling it from the ceiling, have been replaced by simple pneumatic feet (visible at the bottom of figure 2.4). The machine thus now lies on the floor, increasing dramatically its mechanical stability without deteriorating noticeably its performances.
- A type K thermocouple has been installed at the bottom of the outer (77 K) radiation shield to monitor the N<sub>2</sub> solidification process and indicate when the liquid N<sub>2</sub> cryostat is empty.
- Three contact plates made of chromel and allumel (type K thermocouple materials) provide an electrical connection between the sample-holder and the manipulator (*Z* translator), allowing sample temperature measurement and heating by electron bombardment. These contacts were formerly held in place by 8 screws, each supporting a pair of ceramic washers for electrical insulation. This design often led to insulation issues, and was thus replaced with a more efficient one: insulation is now achieved by a pair of Macor<sup>®</sup> plates on each side of the contacts, held in place by the four external screws of the original design (the four inner screws were removed). A stainless steel plate was added on top of the upper-Macor<sup>®</sup> plate for robustness.

## 2.5. Improving our ultralow-temperature STM set-up

---

Finally, we report the following couple of upgrades that were carried out before the beginning of this thesis work, but after the work of L. Claude recorded in [19]:

- In addition to the four internal coaxial cables used to carry the  $I$ ,  $V$ , and  $Z$  signals, and define the potential of the  $Z$  counter-electrode (the so-called  $Z$ -offset signal), a fifth coaxial cable has been installed. It is intended to be used as an antenna to excite spin-processes with electromagnetic radiations. To this effect, it does not share the same duct through the cryostat as the four other coaxial cables, but goes through the same duct as the less-sensitive STM piezo cables ( $X$ ,  $Y$ , and coarse motion piezos), in order to minimize cross-talk issues. At the moment, this new cable only arrives at the 4 K stage of the cryostat, and is thus not usable yet for the intended purpose.
- Teflon rings have been added to the upper edges of the two mobile radiation shields surrounding the STM in order to facilitate their motion, especially at low temperature.



## 3 Single atom magnetism

### 3.1 Magnetism of a free atom

The magnetic properties of an atom are essentially determined by its electrons, carrying both an orbital angular momentum  $\vec{l}$  and an intrinsic angular momentum, or "spin",  $\vec{s}$ .<sup>1</sup> These two quantities can be described by the quantum numbers  $l$ ,  $m_l$  and  $m_s$ . The orbital quantum number  $l$  is defined as

$$\vec{l}^2 = \hbar^2 l(l+1) \quad (3.1)$$

and corresponds to the type of electronic orbital:  $l = 0$  for an  $s$ -orbital, 1 for a  $p$ -orbital, 2 for a  $d$ -orbital, and 3 for an  $f$ -orbital. The magnetic quantum number  $m_l$  gives the projection of  $\vec{l}$  along a specified direction  $z$ ,

$$l_z = m_l \hbar \quad (3.2)$$

and can take on any integer value between  $-l$  and  $l$ . Similarly, the spin quantum number  $m_s$  corresponds to

$$s_z = m_s \hbar \quad (3.3)$$

and can only have two values:  $1/2$  and  $-1/2$ .

The orbital angular momentum  $\vec{L}$  and spin  $\vec{S}$  of the atoms are simply given by the sum of  $\vec{l}$  and  $\vec{s}$  over all the electrons, so that their associated orbital and spin quantum numbers are:

$$L = \sum_i m_{l,i} \quad (3.4)$$

---

<sup>1</sup>This whole section was inspired from [21], which provides a much more rigorous and thorough treatment of this subject. A more general presentation of magnetism can also be found in [22].

$$S = \sum_i m_{s,i} \quad (3.5)$$

Only partially-filled electronic shells give a finite contribution to  $L$  and  $S$ . The filling of the different electronic orbitals, which thus defines  $L$  and  $S$ , is governed by Hund's rules:

1.  $S$  takes on the largest possible value allowed by the Pauli exclusion principle (electrons being Fermions, two electrons cannot have the exact same set of quantum numbers).
2.  $L$  takes on the largest possible value compatible with the first rule.
3. The total angular momentum is  $J = |L - S|$  for less than half-filled shells, and  $J = L + S$  for more than half-filled shells.

The last rule describes the combination of  $\vec{L}$  and  $\vec{S}$  into a total angular momentum  $\vec{J} = \vec{L} + \vec{S}$  through the so-called spin-orbit interaction.

The orbital and spin magnetic moments are defined as

$$\vec{\mu}_L = -g_L \mu_B \vec{L} \quad (3.6)$$

$$\vec{\mu}_S = -g_S \mu_B \vec{S} \quad (3.7)$$

where  $g_L$  and  $g_S$  are the orbital and spin g-factors and are respectively equal to exactly 1 and approximately 2.002 for a free electron, and  $\mu_B$  is the Bohr magneton:

$$\mu_B = \frac{e\hbar}{2m_e} \approx 5.7884 \times 10^{-5} \text{ eV/T} \quad (3.8)$$

The total magnetic moment  $\vec{\mu}_J$  is thus a vectorial sum of the orbital and spin magnetic moments, and can be expressed as

$$\vec{\mu}_J = \vec{\mu}_L + \vec{\mu}_S = -g_J \mu_B \vec{J} \quad (3.9)$$

where  $g_J$ , often written  $g$ , is the Landé g-factor, and is defined as

$$g_J = 1 + \frac{J(J+1) + S(S+1) - L(L+1)}{2J(J+1)} \quad (3.10)$$

Using Hund's rules and equations 3.9 and 3.10, one can calculate the magnetic moment of any free atom, provided that its electronic configuration is known. Table 3.1 presents such values for the 3d transition metal sequence.

### 3.2. Magnetism in solids: a very brief overview

Element	$Z$	el. config.	$L$	$S$	$J$	$g_J$
Sc	21	[Ar]3 $d^1$ 4 $s^2$	2	1/2	3/2	0.8
Ti	22	[Ar]3 $d^2$ 4 $s^2$	3	1	2	0.67
V	23	[Ar]3 $d^3$ 4 $s^2$	3	3/2	3/2	0.4
Cr	24	[Ar]3 $d^5$ 4 $s^1$	0	3	3	2
Mn	25	[Ar]3 $d^5$ 4 $s^2$	0	5/2	5/2	2
Fe	26	[Ar]3 $d^6$ 4 $s^2$	2	2	4	1.5
Co	27	[Ar]3 $d^7$ 4 $s^2$	3	3/2	9/2	1.33
Ni	28	[Ar]3 $d^8$ 4 $s^2$	3	1	4	1.25
Cu	29	[Ar]3 $d^{10}$ 4 $s^1$	0	1/2	1/2	2

Table 3.1: Electronic configuration, orbital, spin, and total magnetic moment, and Landé  $g$ -factors of the 3 $d$  transition metals.

### 3.2 Magnetism in solids: a very brief overview

In order to understand how the interaction with a non-magnetic surface affects the properties of an adsorbed magnetic atom, let us briefly consider what happens when identical magnetic atoms are put together to form a solid: When the atoms assemble in an ordered way to form a crystal, the peculiar symmetry of the surrounding of each atom produces an electric field called the crystal field. For transition metals, the open shells responsible for magnetism are external, and thus directly exposed to the crystal field.

This field lifts the degeneracy of electronic orbitals with different value of  $m_l$ , leading to a reduction of the total orbital angular momentum  $L$ , which is further quenched (partially or totally) by a non-centrosymmetric potential, as the spatial components of  $\vec{L}$  ( $L_x$ ,  $L_y$ ,  $L_z$ ) are no longer conserved, and their temporal average value can become zero. Magnetism in transition metals thus mostly originates from the spin angular momentum  $\vec{S}$ . Moreover, hybridization with the  $d$ -orbitals of neighbouring atoms usually leads to a decrease of  $L$ . The situation is different for rare earth elements, since their open  $f$  shells are screened from the crystal field by  $p$  and  $s$  shells.

When the orbital moment  $\vec{L}$  is not completely quenched, the spin-orbit interaction still couples  $\vec{S}$  and  $\vec{L}$ , leading to a Landé  $g$ -factor  $g < 2$  for less than half-filled shells,  $g = 2$  for half-filled shells, and  $g > 2$  for more than half-filled shells. The crystal field also affects transition metal atoms in another way: it produces energetically favourable and unfavourable directions for the orientation of the orbital moment  $\vec{L}$ , and the spin-orbit interaction translates them as preferential directions for the spin as well, and thus for the total angular momentum  $\vec{J}$ . An energy barrier may then have to be overcome to bring the magnetic moment from a given direction to another one. This is called the magneto-crystalline anisotropy energy, usually noted  $K$  and given in meV/atom in atomic-scale magnetism. At finite temperature, the Néel-Brown model of magnetization reversal yields a characteristic time for the stability of the

system obeying an Arrhenius law [23]:

$$\tau = \tau_0 \exp\left(\frac{NK}{k_B T}\right) \quad (3.11)$$

$N$  is the number of atoms with magneto-crystalline anisotropy energy  $K$ , and the prefactor  $\tau_0$  is of the order of  $10^{-10}$  s. When  $\tau$  is sufficiently large so that the magnetization can be considered as blocked, remanence is achieved.

Magnetism in solids is a much richer and more complex topic, however going further into it would take us away from the main subject of this thesis work, namely magnetism of single adatoms.

### 3.3 Magnetism of adsorbed atoms: an intermediate case

Schematically, the case of magnetic atoms adsorbed on the surface of a crystal is an intermediate case compared to the free atom and the solid: although the atom experiences a crystal field from the surface, as well as a possible charge transfer with the substrate due to a difference in electronegativity, a significant component of  $\vec{L}$  can survive due to the reduced symmetry of the system as compared to a bulk crystal. Consequently, orbital magnetism can become comparable to spin magnetism, so that large total magnetic moments can arise, and very large magnetic anisotropies can develop. This leads to extremely interesting atomic-scale magnetic systems that can furthermore be addressed individually with a local probe technique, such as STM.

Let us consider a transition metal adatom with spin  $\vec{S}$  on a surface. As in the case of solids, we expect the crystal field of the surface to partially quench the orbital momentum  $L$ . Since for transition metals (as opposed to rare earth elements) the energy scale associated with the crystal field is larger than that of the spin-orbit interaction, the latter is generally treated as a perturbation affecting magnetic states defined by an effective spin.

In the case of a perfectly homogeneous surface, the magnetic moment orientation will be isotropic in the surface plane, and anisotropic in the surface normal direction. The system can be described with a uniaxial anisotropy, with the anisotropy axis in the out-of-plane direction. The quantum magnetic state of the system in a magnetic field  $\vec{B}$  is given by the so-called spin Hamiltonian [24]:

$$\hat{\mathcal{H}}_{spin} = g_{\mu\nu} \mu_B \hat{\vec{S}} \cdot \vec{B} + D \hat{S}_z^2 \quad (3.12)$$

where  $g_{\mu\nu}$  is the  $g$  tensor,  $D$  is the uniaxial anisotropy parameter,  $\hat{\vec{S}} = \{\hat{S}_x, \hat{S}_y, \hat{S}_z\}$  is the adatom effective spin operator, and  $z$  is the direction of the anisotropy axis (the out-of-plane direction in our example). The effect of the remaining part of  $L$  manifests itself in the anisotropy parameter  $D$  as well as in the value of  $g_{\mu\nu}$  and in the fact that it is not an isotropic quantity.



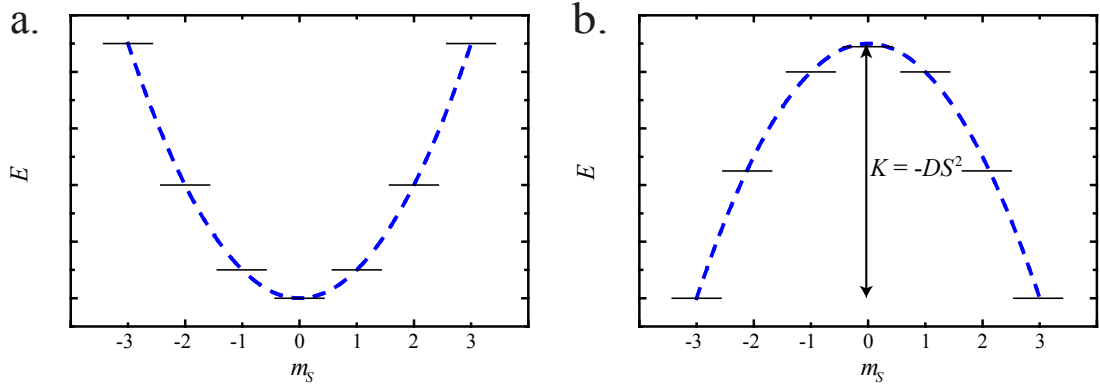


Figure 3.1: Schematic representation of the energy position of the different  $m_S$  states of a  $S = 3$  system with uniaxial anisotropy. **a.** corresponds to the  $D > 0$  case, and **b.** to  $D < 0$ . The energy barrier between the two stable states is indicated.

One immediately sees that in the absence of a magnetic field, states with the same value of  $|m_S|$  have the same energy. If  $S = 1/2$ , no energy barrier can exist between the two possible  $m_S$  states which must remain degenerate to satisfy time reversal invariance, according to Kramers theorem [25].

For  $S \geq 1$ , two scenarios can be distinguished, as illustrated in figure 3.1:

- If  $D > 0$ , the low- $|m_S|$  states ( $m_S = 0$  for integer  $S$ ,  $m_S = \pm 1/2$  for half-integer  $S$ ) are lower in energy, and thus represent the ground state. The high- $|m_S|$  states are excited states.
- If  $D < 0$ , the high- $|m_S|$  states  $m_S = \pm S$  represent the ground state. Magnetization reversal can occur through successive excitation of the system from one of the high- $|m_S|$  states to the low- $|m_S|$  states. The energy cost of this process is thus given by the energy difference between low and high- $|m_S|$  states,  $K = -DS^2$  when  $S$  is an integer, and  $K = -D(S^2 - 1/4)$  when  $S$  is half-integer.<sup>2</sup>

The effect of a magnetic field applied along the quantization direction  $z$  is simply to shift the energy of each  $m_S$  state proportionally to  $g_{\mu\nu}$ ,  $B$ , and the value  $m_S$  itself. This is referred to as the Zeeman effect, and illustrated in figure 3.2, **a.** Conversely, when the magnetic field is applied perpendicularly to the quantization direction, the magnetic states evolve as shown in figure 3.2, **b.**

Things get a little more complicated when considering a non-homogeneous surface, introducing an additional anisotropy in the surface plane. The expression of this additional transverse anisotropy term depends on the symmetry of the surface.

<sup>2</sup>The sign of  $K$  is defined with respect to the surface normal direction. By convention,  $K$  is positive for an out-of-plane easy magnetization axis (or in-plane hard axis), and negative for an out-of-plane hard axis (or in-plane easy axis).

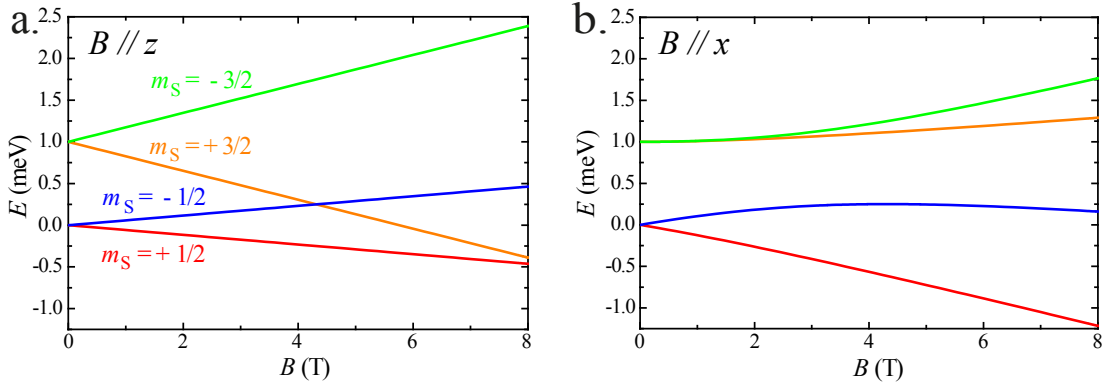


Figure 3.2: Schematic representation of the evolution of the magnetic states of a uniaxially-anisotropic spin-3/2 system with  $D = 0.5$  meV and an isotropic  $g$ -factor of 2. **a.** The magnetic field is applied along the quantization direction of the magnetization ( $z$  direction). The energies of the magnetic eigenstates shift linearly in energy with magnetic field. **b.** The magnetic field is applied perpendicularly to the  $z$  direction. The effect of the magnetic field no longer corresponds to a linear shift of the states.

For a twofold symmetry, the spin Hamiltonian can be re-written as:

$$\hat{\mathcal{H}}_{spin} = g_{\mu\nu} \mu_B \hat{\mathbf{S}} \cdot \vec{B} + D \hat{S}_z^2 + E (\hat{S}_x^2 - \hat{S}_y^2) \quad (3.13)$$

where  $E$  is the transverse anisotropy parameter, and  $\hat{S}_x$  and  $\hat{S}_y$  are the projections of the spin operator along  $x$  and  $y$ . These directions are orthogonal to each other and to the  $z$  direction, which is itself defined such as to maximize  $|D|$ . By convention,  $x$  and  $y$  are chosen in such a way that  $E > 0$ . It is therefore important to note that  $z$  does not necessarily corresponds to the surface normal.

This additional term in the Hamiltonian can have a dramatic effect on the magnetic configuration of the adatom: firstly, the evolution of the various eigenstates with applied magnetic field can be noticeably modified, as illustrated in figure 3.3, **a** and **b**. Secondly, since  $\hat{S}_x$  and  $\hat{S}_y$  do not commute with  $\hat{S}_z$ , they do not share the same eigenstates and eigenvalues. Consequently, the eigenstates of the Hamiltonian can no longer be simply described by the set of possible  $m_S$  values, but correspond to linear combinations of them. In other words, some of the eigenstates may acquire a finite overlap since they share the same  $m_S$  component. This finite overlap allows for quantum tunneling between these states: In the case of  $D < 0$ , magnetization reversal does no longer require to overcome the anisotropy barrier  $K$ , and the temporal magnetic stability of the system is therefore reduced. This purely quantum effect is known as quantum tunneling of the magnetization [26].

For a bistable magnetic system ( $D < 0$ ) with integer effective spin, quantum tunneling of the magnetization may happen between the two lowest-energy (high- $|m_S|$ ) states. Conversely, tunneling is strongly suppressed if  $S$  is half-integer, because states with equal  $m_S$  have no

### 3.4. Spin-Excitation Spectroscopy: probing magnetic excitations with the STM

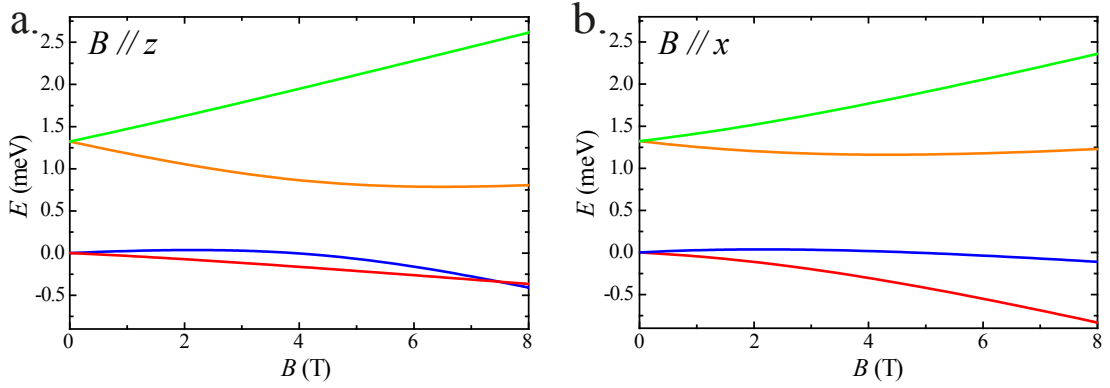


Figure 3.3: Energy of the magnetic states of a fully anisotropic spin-3/2 system with  $D = 0.5$  meV,  $E = 0.25$  and an isotropic  $g$ -factor of 2, as predicted by equation 3.13. **a.** The magnetic field is applied along the highest anisotropy direction ( $z$  direction). **b.** The magnetic field is applied along the  $x$  direction.

overlap [27]. However, in this case, precise calculations of the spin-dynamics of the system still require to take into account quantum tunneling of the magnetization [28].

### 3.4 Spin-Excitation Spectroscopy: probing magnetic excitations with the STM

We mentioned earlier that these fascinating properties can be accessed at the single atom scale using STM. We have also mentioned that tunneling electrons can excite inelastic processes above a given threshold energy, which can be measured in STS (which is sometimes referred to as IETS in that case, see section 2.4, page 10). This applies very well to single adatom magnetism, the inelastic process involved here being the magnetic excitation of the system from ground to an excited state. The technique is then usually called Spin-Excitation Spectroscopy (SES) [29], and can be considered as an STM adaptation of metal-oxide-metal planar junctions doped with magnetic impurities [30, 31, 32], granting access to a single impurity. Spin-excitation with the STM must obey the following selection rule: since an electron carries a spin of  $1/2$ , a tunneling electron can only transfer a quantity  $\Delta m_S = 0, \pm 1$ , and  $\Delta S = 0, \pm 1$ , to the adatom [33].

SES may appear as a very simple technique, however a couple of difficulties have to be overcome, in addition to the general difficulties inherent to single atom STS: although  $\mu_S$  and  $K$  may yield exceptionally large atomic values for single adatoms compared to atoms in bulk materials, as expressed in section 3.3, their absolute value is still rather small, typically  $\sim 1 - 5 \mu_B$  for the first one, and  $\sim 1 - 10$  meV for the second one. Consequently, both the energy of the spin-excitations and their shifting in magnetic fields, which is simply given by  $\Delta E = g m_S B$ , are small. One therefore needs a very high energy resolution in order to resolve

spin-excitation signals, *i.e.*, ultralow temperatures, and high magnetic fields are required to yield observable Zeeman effects. The second difficulty is related to the amplitude of these signals, which corresponds to the probability for a single tunneling electron to excite a magnetic transition. Since the cross section of the spin-carrying orbitals is usually small as compared to conduction orbitals as far as tunneling is concerned,  $dI/dV$  signals related to spin-excitations of adatoms on metals are typically in the 10% range or below.

That is the reason why SES was first demonstrated for single Mn adatoms on 2 ML  $\text{Al}_2\text{O}_3$  on NiAl(110) [29], an ultrathin insulator, granting a 25% cross section to the spin-excitation process, using a 0.6 K 7 T STM. The same group reported spin-excitation measurements for a variety of  $3d$  transition metal atoms on ultrathin insulators, namely:

- $\text{Mn}_n$  ( $n = 1, 2, \dots, 10$ ) chains on  $\text{Cu}_2\text{N}/\text{Cu}(100)$  [33], where the total magnetic moment, as well as the magnetic coupling between the atomic spins were investigated. A spin  $S = 5/2$  per Mn atom and an antiferromagnetic coupling between them were found.
- Fe adatoms on  $\text{Cu}_2\text{N}/\text{Cu}(100)$  [34], where an effective spin  $S = 2$  and a very large anisotropy energy  $K = 6.20 \pm 0.04$  meV were measured.
- Co on  $\text{Cu}_2\text{N}/\text{Cu}(100)$  [35], where an anisotropy energy  $K = 5.5 \pm 0.1$  meV and effective spin  $S = 3/2$  were found. This work actually focused on the Kondo effect, which is described in the next section.
- Co and Fe adatoms coupled together on  $\text{Cu}_2\text{N}/\text{Cu}(100)$  [36]. Here as well the Kondo effect was studied.
- Mn dimers on  $\text{Cu}_2\text{N}/\text{Cu}(100)$  [37], where a spin-polarized tip was used together with large tunnel currents in order to perform successive spin-excitations of the dimer in the same direction ( $\Delta m_S$  always equals  $-1$ ), and thus spin-pumping. Spin-polarized spin-excitation was investigated in more details for Mn and Fe adatoms and are the subject of a short review [38].
- FeCu dimers on  $\text{Cu}_2\text{N}/\text{Cu}(100)$  [39], where in addition to the magnetic moment and anisotropy, the spin relaxation-time was also obtained, using a novel STM-based pump-probe technique.

SES has also been demonstrated for a single atom on a semiconductor, namely an Fe atom embedded in the surface of an InSb crystal [40]. The same group also reported the first observation of spin-excitations for Fe adatoms on a metallic substrate,  $\text{Cu}(111)$  [41], overcoming the challenge presented by the very low cross section of the process in that case (the spin-excitation signal represents only 5% of the total conductance), and demonstrated the itinerant nature of magnetic excitations of adatoms on metals.<sup>3</sup>

---

<sup>3</sup>An earlier publication reporting spin-excitations for Fe and Co adatoms and small clusters on  $\text{Pt}(111)$  exists [42]. However it did not provide an actual proof for the magnetic origin of the observed features, as discussed in the introduction of chapter 4.

This very brief review of SES achievements illustrates some of the numerous possibilities offered by this relatively new technique in the field of atomic-scale magnetism.

### 3.5 A particular case: the Kondo effect

As already foreseen in the previous section, the Kondo effect is closely related to spin-excitations in single adatoms, arising when having a degenerate pair of magnetic states separated by  $\Delta m_S = \pm 1$ .

This effect is an electron correlation effect that is related to scattering of conduction electrons on a localized magnetic moment. It was first observed as the existence of a finite resistivity minimum in dilute magnetic alloys. J. Kondo could accurately compute the low-temperature resistivity of various dilute magnetic alloys using the  $s-d$  interaction model [43], demonstrating that this behaviour was due to spin-dependent scattering of conduction electrons on the localized magnetic impurity. Nowadays, this kind of scattering is usually treated using P. W. Anderson's so-called Single Impurity Anderson model (SIAM) [44], which considers all the possible interactions between electrons in a localized orbital ( $d$  or  $f$ ) and conduction electrons. The key parameters of this model are the Coulomb repulsion  $U$  experienced by two opposite-spin electrons occupying the same localized orbital (on-site repulsion), and the hybridization parameter  $V$  allowing electrons to hop from the conduction band to the localized orbital and reciprocally.

The Kondo effect can be apprehended in a simple picture, as illustrated in figure 3.4: When the system is such that only the singly-occupied level of the localized orbital lies below the Fermi level  $E_F$  (*i.e.*, the Coulomb repulsion term prevents double-occupancy of this level) and the doubly-occupied level is not thermally populated, the Heisenberg uncertainty principle can allow a conduction electron to occupy the half-filled localized state for a very short period of time. The Pauli repulsion principle dictates that this second electron must have the opposite spin as the first one. Since this doubly-occupied state is an excited state and was populated by the Heisenberg uncertainty principle, the system has to relax to single-occupancy in a time-scale associated with the energetic cost of the excitation. The two localized electrons have the same probability to go to the conduction band. Consequently, the spin of the localized orbital, and thus of the magnetic impurity, may have been reversed with 50% probability. Depending on the relative energy of the system, another spin-reversal process may come into play (or even replace this first one): the Heisenberg uncertainty principle may allow the single localized electron to jump into the conduction band, being replaced with another electron with random spin. The consequence of these two processes is the same: after each process, there is a 50% probability for the spin of the magnetic impurity to be reversed, leading to magnetic screening of the impurity by conduction electrons.

This description is of course very schematic. A rigorous theoretical treatment of this problem, such as P. W. Anderson's perturbative treatment and "poor man's scaling" [45] and later, more precise works, demonstrate that below a characteristic temperature, referred to as the Kondo

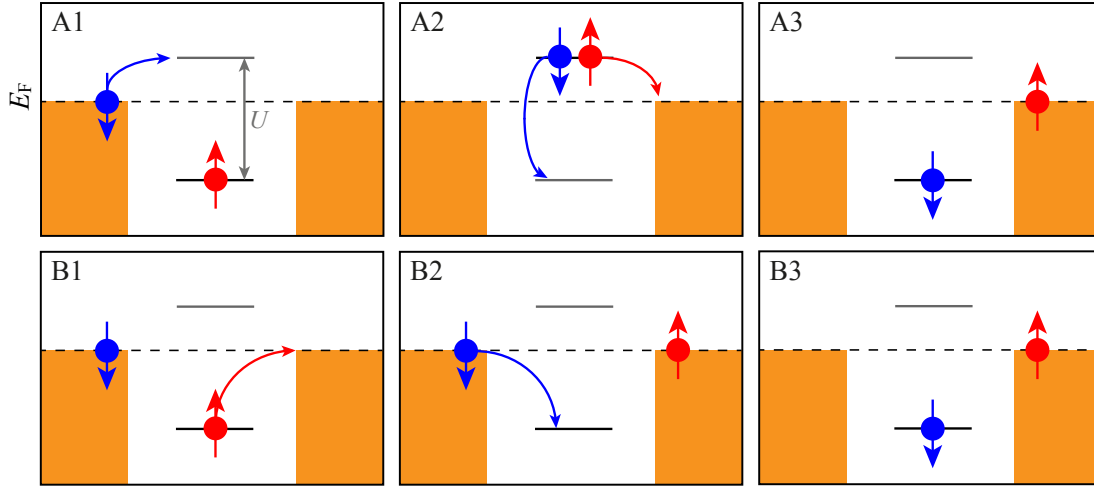


Figure 3.4: Schematic representation of the Kondo magnetic screening process. The orange rectangles represent the valence band of the metal, and the two lines in-between are the singly and doubly-occupied states of the localized orbital. The dashed line is the Fermi level, and the Coulomb repulsion energy is indicated in the first diagram. The upper three diagrams represent the three steps of a spin-reversal process implying momentary double occupancy of the localized level, the lower three correspond to a different process occurring through the emptying of the localized level. Both processes are made possible by the Heisenberg uncertainty principle, and lead to the same final state.

temperature  $T_K$ , the system is in a spin singlet state, *i.e.*, the localized spin on the impurity is fully screened by the interaction with conduction electrons. Above this temperature, the system behaves in the usual way, the conduction electrons passing by the magnetic impurity interacting only weakly with its magnetic moment.

The Kondo effect not only manifests itself in the low-temperature resistivity of the system, but also in its magnetic susceptibility and heat capacity, and a sharp resonance appears in the DOS, close to the Fermi level. It is usually called Kondo resonance or Abrikosov–Suhl resonance, its half-width at half-maximum (HWHM) is simply given by  $k_B T_K$ .<sup>4</sup>

The Kondo effect not only occurs in dilute magnetic impurity alloys, as first discovered, but also in many bulk compounds such as many Ce and Yb compounds, artificially constructed quantum dots, and magnetic adatoms on metallic surfaces, which is the subject of this work. Such a single-adatom Kondo effect was first reported for Co adatoms on Au(111) [48], manifesting itself through the Kondo resonance observed in STS. This resonance may take on a very different shape from the simple peak observed in Photoemission spectroscopy (PES) [49, 50]. The reason is that the orbitals mainly involved in quantum tunneling are the  $s$  and  $p$  orbitals. Quantum interference between the  $d$  (for transition metals) or  $f$  (for rare earth elements) orbital and the continuum of tunneling channels lead to a resonance feature corresponding to a Fano function [51]:

$$\frac{dI}{dV} = \frac{(\epsilon' + q)^2}{\epsilon'^2 + 1}, \quad \epsilon' = \frac{eV - \epsilon_0}{\Gamma} \quad (3.14)$$

where  $q$  corresponds to the quality of the coupling between the localized and tunneling states,  $\epsilon_0$  is the position of the resonance, and  $\Gamma$  its HWHM. Figure 3.5 illustrates how the value of  $q$  affects the lineshape of the Fano function: Kondo resonances in STS can assume lineshapes from a symmetric dip to a centrally symmetric dip-peak feature, and from an asymmetric dip-peak to an almost symmetric peak that tends to a Lorentzian.

The lineshape itself is usually not enough in order to prove the Kondo origin of a very low energy feature in STS. The most generally used criterion is the temperature dependence of the feature. The full-width at half-maximum (FWHM) of a Kondo resonance has an intrinsic temperature dependence that can be estimated from Fermi liquid theory to be [35, 52]:

$$2\Gamma = \sqrt{(\alpha k_B T)^2 + (2k_B T_K)^2} \quad (3.15)$$

where a value of 5.4 is expected for  $\alpha$  considering the usual smearing of the electron distribution in metals [53]. The temperature dependence of the peak height can be approximated by the empirical law [54]:

$$G(T) = G_0 \left( \frac{T_K'^2}{T^2 + T_K'^2} \right)^s, \quad T_K' = \frac{T_K}{\sqrt{2^{1/s} - 1}} \quad (3.16)$$

<sup>4</sup>For more information on the Kondo effect and its theoretical treatment, one may refer to [46] or [47].

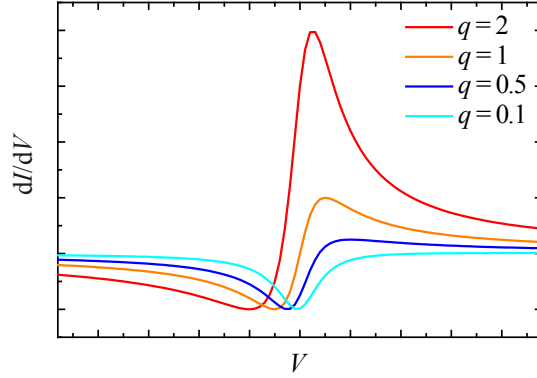


Figure 3.5: Fano functions calculated from equation 3.14 for  $q$  values between 0.1 and 2. The lineshape progressively evolves from a symmetric dip centred at  $\epsilon_0$  into an asymmetric dip-peak feature that tends to a symmetric peak as  $q$  increases.

where  $s = 0.22 \pm 0.01$  in the case of a spin-1/2 Kondo effect. Figures 3.6, **a** and **b** illustrates the thermal behaviour of the intrinsic width and height of a Kondo resonance.

Let us now briefly discuss the conditions for a Kondo effect to appear in a single transition metal adatom on a non-magnetic surface: a degenerate pair of  $m_S$  states separated by  $\Delta m = \pm 1$  is required [35], so that a single electron can excite a spin-reversal of the adatom at a very low energy cost, and a measurement temperature below or close to  $T_K$ . Note that a Kondo effect can also exist in integer spin systems, such as  $S = 1$  systems, provided that the  $m_S = 0, \pm 1$  states are degenerate. In that particular case, a single electron cannot completely flip the magnetization of the impurity, and the system is thus in a partially screened state, as demonstrated in an artificial quantum dot [55].

Transition metal adatom Kondo systems present a peculiarity as compared to some other Kondo systems: the large magnetic anisotropy that can arise due to the surface crystal field is not only determinant for the existence of a Kondo effect, but it also determines the way in which the Kondo resonance is affected by an external magnetic field [35, 56]. Indeed, while in isotropic systems the resonance is simply split by the Zeeman energy due to the lifting of degeneracy between the opposite spin states (the Zeeman energy has to be paid to flip the magnetization from parallel to anti-parallel with respect to the magnetic field direction), the behaviour of the resonance in anisotropic systems can yield information not only on the effective spin, but also on the peculiar anisotropy of the magnetic impurity-substrate system.



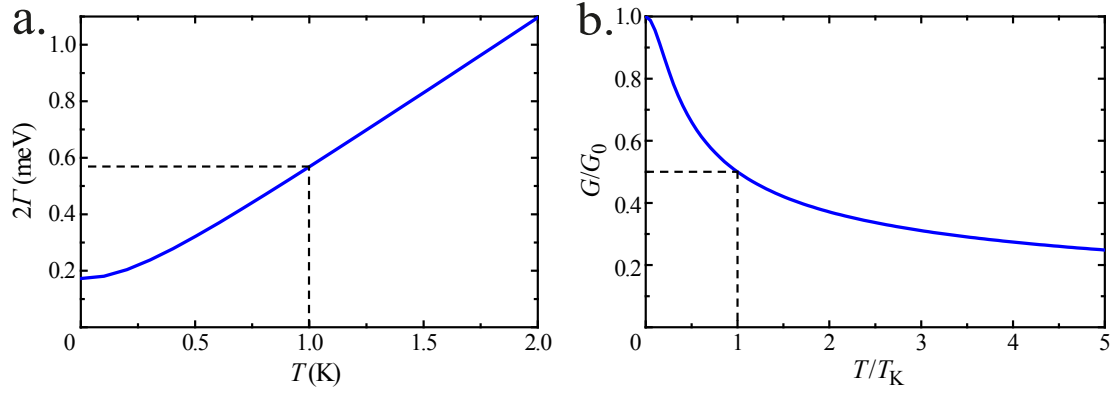


Figure 3.6: **a.** Intrinsic width (FWHM) of the Kondo resonance as a function of  $T$ , for a  $T_K$  of 1 K, calculated from equation 3.15. The dashed lines correspond to  $T_K$  and evidence how the behaviour changes from approximately parabolic below  $T_K$ , to nearly linear above it. **b.** Relative amplitude of the Kondo resonance versus  $T/T_K$ , calculated from equation 3.16. As in **a**, the dashed lines mark the position of  $T_K$ , where the amplitude is exactly half of the amplitude at 0 K.



## 4 Co and Co-hydrides on Pt(111): an attempt at discovering single-adatom magnetic remanence, and an unexpected Kondo effect

As presented in the introduction, the motivation behind this thesis work was to demonstrate magnetic remanence in single adatoms. We therefore very naturally chose the single adatom system that yields the largest anisotropy in the whole literature, Co/Pt(111) [57]. Equally important to the anisotropy value is its direction, namely, the necessity to have an easy magnetization axis ( $D < 0$ ), and therefore a ground state consisting of a pair of oppositely magnetized states,  $m_S = \pm S$ , separated by an anisotropy barrier  $K = -DS^2$  for integer spin, or  $K = -D(S^2 - 1/4)$  for half-integer spin (see section 3.3, page 22). Co/Pt(111) fulfils this criterion, having a negative  $D$  and a magnetic anisotropy energy  $K = 9.3 \pm 1.6$  meV as determined by X-ray Magnetic Circular Dichroism (XMCD) [57]. The anisotropy barrier separating the  $m_S = \pm S$  states therefore approximately corresponds to the thermal energy at 110 K, and should yield a stability time of about 50 s at 4 K according to equation 3.11, page 22, assuming a prefactor  $\tau_0 = 10^{-10}$  s, and greater than  $10^{99}$  s at 0.4 K under the same assumptions.

Single Co adatoms on Pt(111) have been the subject of several experimental investigations during the last 10 years [42, 57, 58, 59]. The XMCD measurements that first reported the giant magnetic anisotropy of this system also obtained a total magnetic moment of  $(5.0 \pm 0.6) \mu_B$ , due to the spin and orbital moments of both Co adatom and neighbouring Pt atoms. The exact value of the effective spin can however not be deduced without knowing the value of the Landé g-factor. These measurements were performed at 5.5 K, and did not exhibit signs of magnetic remanence [57], which would manifests itself as an hysteretic behaviour in the magnetization curves. The resolution of this technique as well as the temperature could however justify this observation, which is therefore not a proof of the absence of magnetic remanence.

A first STS study performed at  $T = 5$  K did not report any signs of inelastic excitations [58]. Here as well an insufficient resolution can be invoked, an inelastic signal below 10% of the

## Chapter 4. Co and Co-hydrides on Pt(111): an attempt at discovering single-adatom magnetic remanence, and an unexpected Kondo effect

---

conductance in the mV range would not have been observable in these conditions.

A very detailed SP-STM study produced full-magnetization curves of single Co adatoms on Pt(111) [59], giving magnetic moments for the two inequivalent adsorption sites  $\mu_{\text{HCP}} = (3.9 \pm 0.2) \mu_{\text{B}}$  and  $\mu_{\text{FCC}} = (3.5 \pm 0.2) \mu_{\text{B}}$  at  $T = 0.3$  K and no sign of remanence (S-shaped magnetization curves, no hysteresis). The tunnel parameters were  $V = 300$  mV,  $I = 0.8$  nA, it is therefore expected that even if the adatoms had their magnetic moment blocked, the tunneling electrons at such a high bias voltage would have enough energy to produce spin-excitations, giving a uniform magnetic signal over all the adatoms.

A third STM-based study presented STS at 4.3 K [42]. This work focused on a very small energy interval around the Fermi level, and reported an inelastic feature at  $10.25 \pm 0.15$  meV attributed to the  $m_S = \pm 1$  to  $m_S = 0$  transition. This would be a very encouraging observation regarding the possibility for observing magnetic remanence in Co/Pt(111) provided that the magnetic origin of these features could be ascertained. Unfortunately, no solid proof was provided, since no measurements in magnetic field were reported. Another concern is the very large tunnel current employed ( $I \approx 10$  nA), in this regime the adatom-tip interaction may not be negligible, thus the properties may not correspond to those of free Co/Pt(111).

All these investigations have therefore not refuted the existence of magnetic remanence in Co/Pt(111), and the possibility to access it with SP-STM. This constituted the very exciting starting point of this thesis work.

### 4.1 Co and Co hydrides on Pt(111)

Pt(111) was prepared with about a hundred cycles of  $\text{Ar}^+$ -ion sputtering ( $I = 0.8 \mu\text{A}$ ,  $E = 0.9$  keV,  $\Delta t = 600$  s) followed by flash annealing at 1400 K in a base pressure of  $\sim 5 \times 10^{-10}$  mbar, until surfaces with about  $2 \times 10^{-2}$  ML of impurities were obtained (ML stands for monolayer, 1 monolayer corresponding to one object per Pt(111) surface atom). The main bulk contaminant of Pt being C, an impurity that segregates at the surface upon annealing, several long high-temperature  $\text{Ar}^+$  sputtering cycles ( $I = 3 \mu\text{A}$ ,  $E = 4$  keV,  $T = 1500$  K,  $\Delta t = 3$  h) were found to help noticeably reduce the concentration of C near the surface, as observed performing Auger Electron Spectroscopy (AES). Co atoms were deposited *in situ* on the surface at a temperature  $T = 17$  K using a commercial electron beam evaporator with 99.995% purity Co rod, operated at a flux of  $4 \times 10^{-4}$  ML/s.

Figure 4.1, **a** presents an STM image of the Pt(111) surface after deposition of  $4.5 \times 10^{-3}$  ML of Co. Three different apparent heights are found for the Co-related protrusions, as evidenced by the displayed cut taken along the red line in figure 4.1, **b**:  $1.52 \pm 0.03$  Å,  $1.85 \pm 0.06$  Å, and  $1.44 \pm 0.01$  Å, given in decreasing order of abundance. These observations are in-line with a former report [60]. Three different kinds of impurities can also be observed:  $0.10$  Å (abundance:  $2 \times 10^{-2}$  ML) and  $0.28$  Å deep ( $2 \times 10^{-3}$  ML) depressions (also visible in the line-cut), and  $0.37$  Å high protrusions (below  $1 \times 10^{-3}$  ML). It is worth noting that these apparent heights

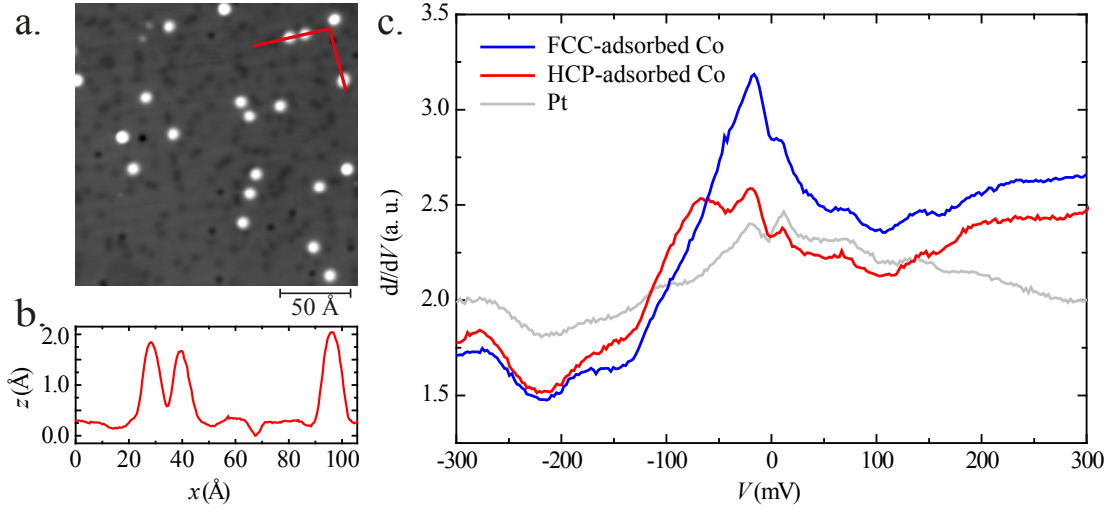


Figure 4.1: **a.** STM image of Co adatoms on Pt(111).  $I_t = 100$  pA,  $V = -50$  mV,  $T = 4.4$  K. **b.** Apparent height line cut along the red line presented in **a**, evidencing adsorbates with three different heights. **c.**  $dI/dV$  spectra taken over fcc- and hcp-adsorbed Co adatoms, as well as over the bare Pt surface.  $I_t = 0.7$  nA,  $V = -300$  mV,  $V_{mod} = 14$  mV<sub>pp</sub>,  $T = 4.4$  K.

depend on the bias voltage and the tip apex (the heights given here have been measured at a bias voltage  $V = -50$  mV and a constant current  $I_t = 100$  pA). This is particularly true for the first two types of impurities. However, the 6 features always exhibit significantly different apparent heights, by which they can be unequivocally distinguished.

The highest Co-related protrusions are readily identified as clean Co/Pt(111), their STS spectra presented in figure 4.1, **c** matching remarkably well the previously published ones [58, 59], which also allows to identify hcp- and fcc-adsorbed atoms.

In marked contrast, the intermediate-height ones, which we refer to as "type 1" Co complexes, display very prominent (20% of the conductance in total) inelastic conductance steps, as one can see in figure 4.2, **a** and **b**. Two slightly different spectra are observed, revealing in both cases several inelastic excitations in the 1 to 20 meV energy range. These differences were unequivocally ascribed to a different adsorption site, as explained below.

Interestingly, the energies of these excitations are quite close to the magnetocrystalline anisotropy energy (MAE) of Co on Pt(111) [57] and the spin excitation energy reported in a former STM study [42], though both our experimental conditions and observations differ noticeably.

A different behaviour was observed for the second type of Co complex, referred to as "type 2". STS spectra for this type reveal less intense inelastic steps (1-9%) at threshold energies of  $9.6 \pm 1.5$  meV and  $25.5 \pm 0.7$  meV, together with a very sharp zero-bias conductance peak, as one can see in figure 4.2, **c** and **d**.

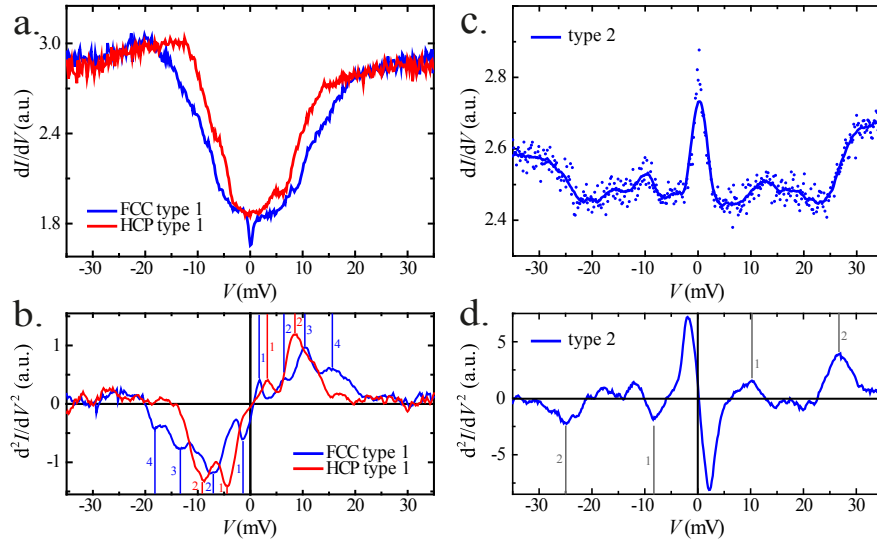


Figure 4.2: **a.**  $dI/dV$  spectra taken over fcc- and hcp-adsorbed Co complexes of type 1. Each pair of symmetric steps corresponds to the onset of an inelastic excitation process. The numerical derivatives of these spectra are shown in **b**, and allow for a straightforward reading of the threshold energies of the various excitations.  $I_t = 1$  nA,  $V = -50$  mV,  $V_{mod} = 0.3$  mV<sub>pp</sub>,  $T = 0.4$  K. **c.**  $dI/dV$  spectra taken over a Co complex of type 2. It exhibits two pairs of conductance steps as well as a narrow peak close to the Fermi level. The dots correspond to raw data, the solid line to numerically smoothed data. **d.** Numerical derivative of **c**.  $I_t = 0.75$  nA,  $V = -50$  mV,  $V_{mod} = 1$  mV<sub>pp</sub>,  $T = 0.4$  K.

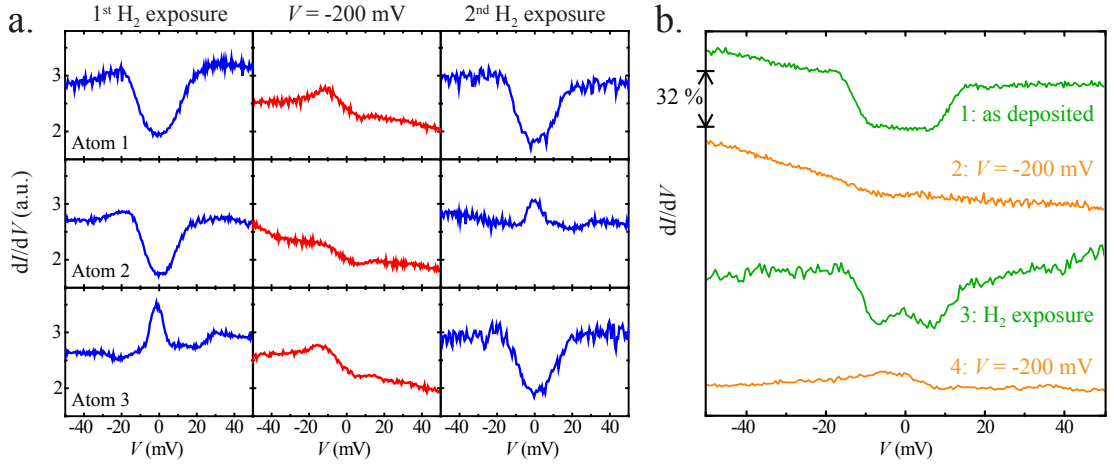


Figure 4.3: **a.**  $dI/dV$  spectra obtained over three different Co adatoms. After a first  $H_2$  exposure (first column), 1 and 2 are of type 1, and 3 is of type 2. After scanning the area with  $V = -200$  mV (second column), 1 and 3 show clean fcc-adsorbed Co/Pt(111) spectra, 2 shows clean hcp Co/Pt(111) spectrum. After a second  $H_2$  exposure (third column), 1 is still of type 1, while 2 and 3 changed into the other type (from type 1 to type 2 for 2, and the opposite for 3).  $I_t = 1$  nA,  $V = -50$  mV,  $V_{mod} = 2.8$  mV<sub>pp</sub>,  $T = 4.4$  K. **b.**  $dI/dV$  spectra taken over an Fe complex on Pt(111), displaying very similar inelastic features as type 1 Co complex. In this case as well, the inelastic features disappear after voltage pulses of -200 mV, and reappear upon exposure to  $H_2$ .  $V = -50$  mV,  $I_t = 1$  nA,  $V_{mod} = 2.8$  mV<sub>pp</sub>,  $T = 4.4$  K.

#### 4.1.1 Switching types with voltage pulses and exposure to $H_2$

It was found that the inelastic features could be suppressed, stabilizing the STM tip over the adatom at  $|V| \geq 175$  mV with  $I_t = 100$  pA. Type 1 and 2 complexes switch into clean Co adatoms, as proved by their STS spectra. The switching does not depend on the polarity of the bias, and is irreversible. We could then unequivocally relate the two slightly different type 1 spectra to a different adsorption site for the adatom, as indicated in figure 4.2, **a**. No such clear dependence on the adsorption site was seen for type 2.

Suspecting a H contamination, we exposed clean Co adatoms to molecular H, and they turned into type 1 and 2. Figure 4.3, **a** illustrates the evolution of two selected complexes of both types after tip-induced cleaning and exposure to  $H_2$ . It demonstrates that both types of complexes are Co hydrides, and can be transformed into the other type after voltage-cleaning and  $H_2$  exposure. The difference between the two types thus neither lies in a different adsorption site for the Co adatom nor in the proximity of a specific impurity. They must therefore correspond to two different  $CoH_n$  configurations (with different or identical  $n$ ).

Comparable results were found for Fe adatoms on Pt(111). Some Fe complexes show inelastic features with a single threshold energy of  $12.0 \pm 0.5$  meV, which disappear after a -200 mV voltage pulse and reappear upon H adsorption, as shown in figure 4.3, **b**. Other Fe complexes

## Chapter 4. Co and Co-hydrides on Pt(111): an attempt at discovering single-adatom magnetic remanence, and an unexpected Kondo effect

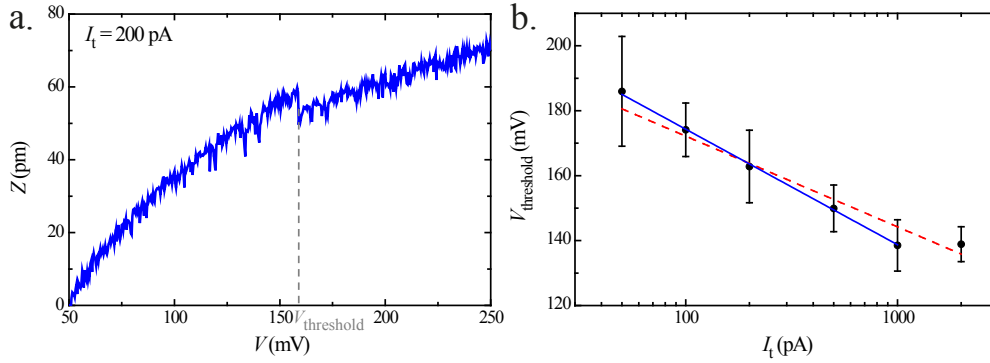


Figure 4.4: **a.**  $Z(V)$  curve acquired on top of a type 1 Co complex. Deprotonation is seen as a sharp downward step, as indicated by the grey dashed line.  $I_t = 200$  pA,  $T = 4.4$  K. **b.** Hydrogen desorption voltage versus tunnel current. Each data point corresponds to the average  $V_{\text{threshold}}$  value obtained from  $Z(V)$  curves as presented in **a**. Average over 10  $\text{CoH}_x$  complexes. The error bars correspond to the standard deviation, the solid blue line is a fit to the first five points and the dashed red line is a linear fit to the six points.  $V_{\text{threshold}}$  decreases exponentially with  $I_t$ , until it reaches a minimum value of about 0.14 V.

were found, but without conductance steps or peaks as clear as those observed for Co.

In order to get some insight regarding the desorption mechanism, we performed voltage ramps over type 1 complexes at constant current, while monitoring  $Z$ . The continuous increase is followed by a sharp jump or drop, depending on the STM tip, of several pm at a threshold voltage, as shown in figure 4.4, **a**. This discontinuity corresponds to tip-induced deprotonation of the adatom. Repeating this procedure over a range of tunnel current values, we obtain the relationship between threshold voltage and tunnel current presented in figure 4.4, **b**.  $V_{\text{threshold}}$  decreases exponentially with  $I_t$  between 50 pA and 1 nA, where it reaches a constant value. This behaviour is characteristic of a single-electron excitation process [61].

After exposing the surface to large amounts of  $\text{H}_2$ , another type of Co complex was also found. It has a triangular shape and does not show any inelastic feature in STS, as shown in figure 4.5. These triangular complexes certainly correspond to H-saturated Co adatoms, and were tentatively identified as  $\text{CoH}_3$  owing to their shape.<sup>1</sup>

To determine the physical origin of all these spectroscopic features, the consequences of isotopic substitution, temperature variations, and external magnetic fields were investigated.

<sup>1</sup>Their similarity with  $\text{CoH}_3$  on graphene/Pt(111), as described in the next chapter, also justifies this identification.



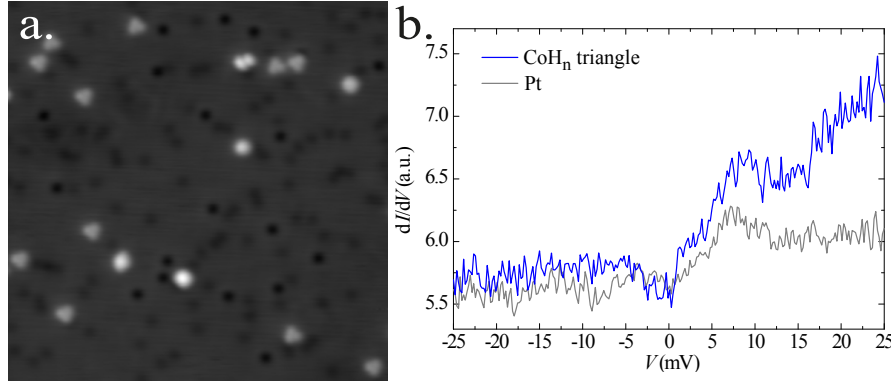


Figure 4.5: **a.** STM image of a much hydrogenated Co/Pt(111) sample. Most of the  $\text{CoH}_x$  complexes appear as triangles. Image size :  $17.5 \times 17.5 \text{ nm}^2$ , tunnel current  $I_t = 83 \text{ pA}$ , bias voltage  $V = -50 \text{ mV}$ , temperature  $T = 4.4 \text{ K}$ . **b.**  $dI/dV$  spectrum of a triangular  $\text{CoH}_x$  complex. A spectrum acquired directly over the Pt(111) surface is also shown for comparison.  $V = -25 \text{ mV}$ ,  $I = 0.5 \text{ nA}$ ,  $V_{\text{mod}} = 1 \text{ mV}_{\text{pp}}$ ,  $f = 919 \text{ Hz}$ ,  $T = 4.4 \text{ K}$

#### 4.1.2 Isotopic substitution

A sample with clean Co adatoms was exposed to molecular D instead of H. For type 1 complexes, no noticeable difference could be observed. Figure 4.6 presents the spectra obtained for type 2.

After exposure to  $\text{D}_2$ , the larger conductance steps appear at  $18.0 \pm 0.5 \text{ meV}$  and  $20.7 \pm 0.4 \text{ meV}$ . These energies relate to the former threshold energy of  $25.5 \pm 0.7 \text{ meV}$  by ratios of  $\sqrt{2}$  and  $\sqrt{3/2}$ , respectively. Such ratios correspond to masses of 2, 3, 4 u and suggest collective vibration of two H (respectively one H and one D, or two D) atoms. They are unlikely to correspond to Co-H stretching modes, since only two energies would be expected, corresponding to linear vibration of Co-H and Co-D. Neither can they originate from rotational modes, in which case the energies scale linearly with mass [62], or hydrogen bond modes, where the energy involves the mass of the heavier atom (see the beginning of section 4.1.4, page 43). We therefore believe that these inelastic features arise from a bending mode of  $\text{CoH}_2$ ,  $\text{CoHD}$ , and  $\text{CoD}_2$ , respectively [63].

The lower conductance steps located at  $10 \pm 1.5 \text{ meV}$  for H-exposed type 2 also seem to shift to  $8 \pm 1$  and  $7 \pm 1 \text{ meV}$  upon isotopic substitution, which tends to indicate a similar vibrational origin.

As one can also see from figure 4.6 the large conductance peak at the Fermi level is, within our experimental accuracy, invariant upon isotopic substitution. It is worth noting that type 2 complexes are deprotonated in the same conditions as type 1, and are usually switched into type 1 applying slightly lower voltages. We can therefore infer that type 1 corresponds to  $\text{CoH}$ , and type 2 to  $\text{CoH}_2$ .

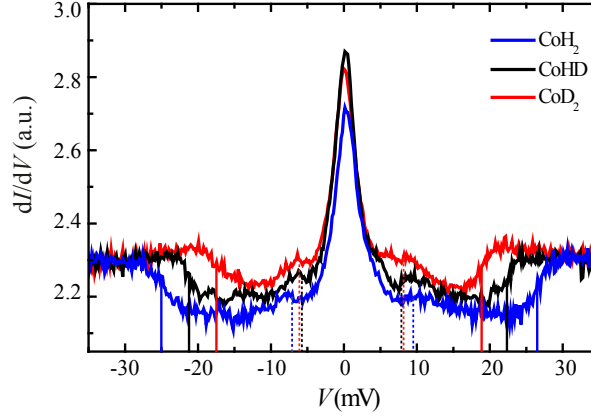


Figure 4.6:  $dI/dV$  spectra taken over three different  $\text{CoH}_2$  complexes after exposure to  $\text{D}_2$ . Vertical lines represent the threshold voltage of the conductance steps. A parabolic background was subtracted from each spectrum.  $V = -50$  mV,  $I_t = 0.75$  nA,  $V_{mod} = 1$  mV<sub>pp</sub>,  $T = 4.4$  K.

#### 4.1.3 Temperature dependence

$dI/dV$  spectra for  $\text{CoH}_2$  were acquired at 0.4, 2.6, 4.2 and 11 K, as shown in figure 4.7. Fitting the zero-bias peaks with a thermally and modulation broadened Fano function [51] (see section 3.5, page 27), as described in [52], we obtained the width versus temperature relationship presented in figure 4.8, **a**. This peculiar relationship can be relatively well fitted with equation 3.15, page 29 [35]:

$$2\Gamma = \sqrt{(\alpha k_B T)^2 + (2k_B T_K)^2}$$

We can thus unequivocally conclude that this Co-hydride complex is a Kondo system. The blue line correspond to a fit with two fit parameters,  $\alpha$  and  $T_K$ . It gives a Kondo temperature  $T_K = 10 \pm 1$  K, and  $\alpha = 8.5 \pm 1$ .

This last value is quite surprising since a value of 5.4 is expected (see section 3.5, page 27). Moreover, considering only Fermi-Dirac and modulation broadening implies that any noise-related broadening was neglected. This value of  $T_K$  thus constitutes an upper bound. To obtain a lower bound, we have performed another fit of the data points fixing  $\alpha = 5.4$  and including noise-related broadening as an effective temperature offset. Unfortunately, we did not have the necessary reference measurement to estimate the actual effective temperature offset of our STM set-up. Considering that the fit gives realistic values for  $T_K$  for effective temperature offsets up to 3 K, we took this fairly large value as an upper bound. We thus obtained the red line in figure 4.8, **a**, which corresponds to a Kondo temperature  $T_K = 4.5 \pm 1$  K. In conclusion, the temperature evolution of the Fermi-Dirac and modulation deconvoluted peak demonstrate that it originates from the Kondo effect, and the Kondo temperature of this system can be roughly estimated as  $T_K = 8 \pm 4$  K.

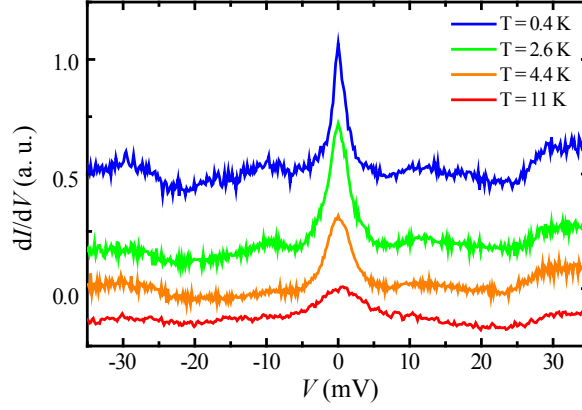


Figure 4.7:  $dI/dV$  spectra of  $\text{CoH}_2$  (type 2 complexes) acquired at different temperatures.  $I_t = 0.75$  nA,  $V = -45$  mV,  $V_{mod} = 1$  mV<sub>pp</sub>.

The height of the Kondo peak can also be used to estimate the Kondo temperature of the system, as explained in section 3.5, page 27. However, it is in principle less reliable than the width, considering that the  $dI/dV$  signal is proportional to the DOS of the tip (see equation 2.6, page 7), which certainly underwent significant changes between the different measurements, performed on different days. Extracting the intrinsic height of the peak from the same Fermi-Dirac and modulation broadened Fano function that were fitted to the experimental spectra to obtain the intrinsic width, the values presented in figure 4.8, **b** were obtained. These values were fitted with the empirical expression of equation 3.16, page 29 [54]:

$$G(T) = G_0 \left( \frac{T_K'^2}{T^2 + T_K'^2} \right)^s, \quad T_K' = \frac{T_K}{\sqrt{2^{1/s} - 1}}$$

The fit, represented as a blue line in figure 4.8, yields a Kondo temperature  $T_K = 3 \pm 1$  K, which conflicts with the value obtained from the width of the Kondo peak.<sup>2</sup> The value of  $s$  obtained from the fit,  $0.4 \pm 0.1$ , instead of the expected value of 0.22, adds some more concerns regarding the reliability of the method. It is therefore probable that significant changes happened in the density of states of the tip between the different measurements, leading to a biased value for  $T_K$ . The value obtained from the width should be considered much more reliable.

<sup>2</sup>Please note that no effective temperature offset was introduced in this fit, since it leads to a decrease in the Kondo temperature and a deterioration of the fit quality.

#### Chapter 4. Co and Co-hydrides on Pt(111): an attempt at discovering single-atom magnetic remanence, and an unexpected Kondo effect

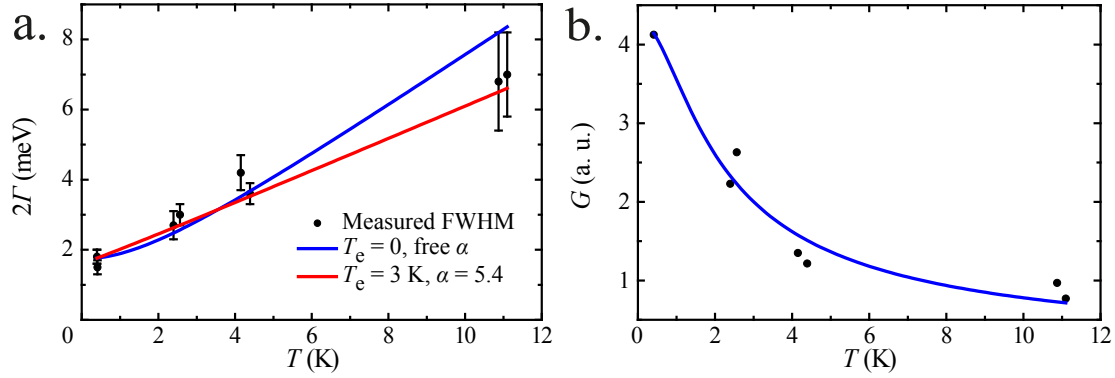


Figure 4.8: **a.** Full-width at half-maximum of the zero-bias peak versus temperature. Spectra such as those presented in figure 4.7 were fitted with the convolution of a Fano function and the Fermi-Dirac and modulation broadening functions. Assuming that there is no other significant source of broadening, the extracted value for the width corresponds to the intrinsic width. The blue line is a fit using equation 3.15, page 29. It gives a Kondo temperature  $T_K = 10 \pm 1$  K and a parameter  $\alpha = 8.5 \pm 1$ . The red line is intended to provide a lower bound to  $T_K$ . It is a fit using the same equation, but  $\alpha$  is fixed to 5.4 and electronic broadening corresponding to an increase in the temperature of 3 K has been added. The introduction of an effective temperature offset improves noticeably the quality of the fit, which corresponds to a Kondo temperature  $T_K = 4 \pm 1$  K. **b.** Intrinsic height of the Kondo peak extracted with the same procedure as the intrinsic width. The blue line is a fit using equation 3.16, page 29. It yields a Kondo temperature  $T_K = 3 \pm 1$  K for an  $s$  value of  $0.4 \pm 0.1$ .

#### 4.1.4 Effect of an out-of-plane magnetic field

STS spectra were acquired on top of CoH (type 1) and CoH<sub>2</sub> (type 2) in magnetic fields up to 8 T, applied perpendicularly to the surface. From inspection of figure 4.9, we can conclude that CoH spectra do not exhibit any significant difference while exposed to a high external field. No change in the energy position of the inelastic features can be observed within our error bars. We thus conclude on a vibrational origin for all the inelastic features of CoH. The absence of differences between H and D-related spectra implies that the mass of the H atom is not directly involved in the vibration. Moreover, the same mode exists for FeH/Pt(111), and presents a different energy, as shown in figure 4.3, **b**. Such low-energy vibrational modes for X-H bonds are commonly referred to as hydrogen bond modes. They are attributable to the attractive potential between the H and X atoms, and involve motion of the heavy X atom. Due to the large reduced mass of the system and the small force constant corresponding to the weak hydrogen bond, their energy typically lies in the 5 – 40 meV range for molecules in solution [64], well below that of the X-H stretching mode. These vibrational features are also very similar to those formerly reported for several singly-hydrogenated rare earth and transition metal atoms on Ag(100) [65], where they were attributed to H-induced frustrated translation of the adatom.

STS spectra of a CoHD complex in out-of-plane magnetic fields of 4, 6 and 8 T are shown in figure 4.10, **a**. None of the conductance steps exhibit any noticeable difference induced by the magnetic field in our measurement conditions ( $T = 0.4$  K,  $V_{mod} = 1$  mV<sub>pp</sub>). This further confirms their vibrational origin, as already concluded from the effect of isotopic substitution. On the other hand, the Kondo peak splits very clearly with the external field, what is better seen in the close-up displayed in figure 4.10, **b**. These measurements in magnetic field allow us to access the spin configuration of this Kondo system.

The transition energy given by the peak separation are reported in figure 4.11, **a**. In order to determine the spin configuration of the CoHD complex, we rationalize the spin excitation through the effective spin Hamiltonian of equation 3.13, page 24:

$$\hat{\mathcal{H}}_{spin} = g_{\mu\nu}\mu_B\hat{\vec{S}} \cdot \vec{B} + D\hat{S}_z^2 + E(\hat{S}_x^2 - \hat{S}_y^2)$$

where  $\vec{B}$  corresponds to the external magnetic field,  $D$  is the uniaxial anisotropy parameter,  $E$  the transverse anisotropy parameter for a twofold symmetry,  $\hat{\vec{S}} = (\hat{S}_x, \hat{S}_y, \hat{S}_z)$  is the adatom total effective spin, and  $g_{\mu\nu}$  is the electron Landé g-factor in its tensor form, which will simply be noted  $g$  in the following.

The presence of the Kondo effect indicates that the ground state is a degenerate doublet of states separated by  $\Delta m_S = 1$  (see section 3.5, page 27). We therefore consider the cases of  $S = 1/2$  and  $S = 3/2$  with  $D > 0$  [35]. Since the spin excitation energy corresponds to the energy difference between the ground state and the first excited state, the measured transition energy should be compared to this difference, as shown in figure 4.11, **a**. For the case of  $S = 1/2$ , the ground state doublet splits with a slope of  $\pm 1/2 g\mu_B B$ , giving an expected transition energy of

**Chapter 4. Co and Co-hydrides on Pt(111): an attempt at discovering single-atom magnetic remanence, and an unexpected Kondo effect**

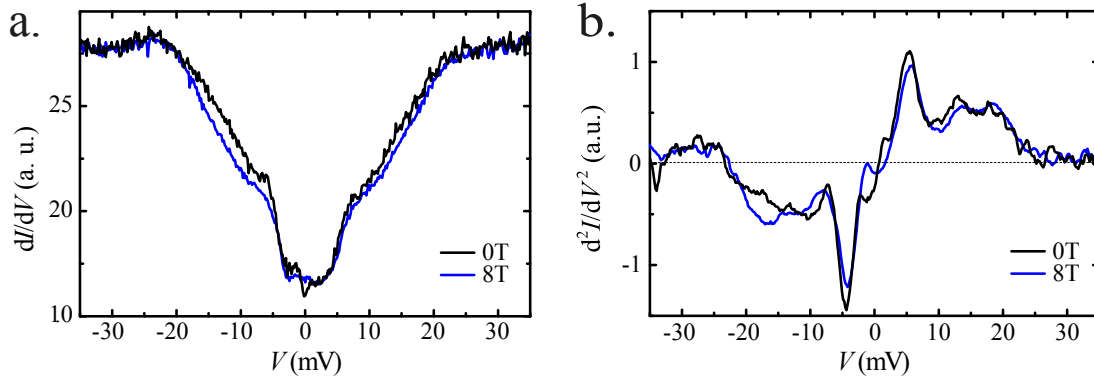


Figure 4.9: **a.**  $dI/dV$  spectra of two similar fcc-adsorbed CoH complexes acquired at 0 and 8 T applied perpendicularly to the sample.  $V = -45$  mV,  $I_t = 0.75$  nA,  $V_{mod} = 1$  mV<sub>pp</sub>,  $T = 0.4$  K. **b.** Numerical derivative of **a.** Although some minor differences are observable between 0 and 8 T, the position of the inelastic features remains the same, ruling out the hypothesis of spin-excitations.

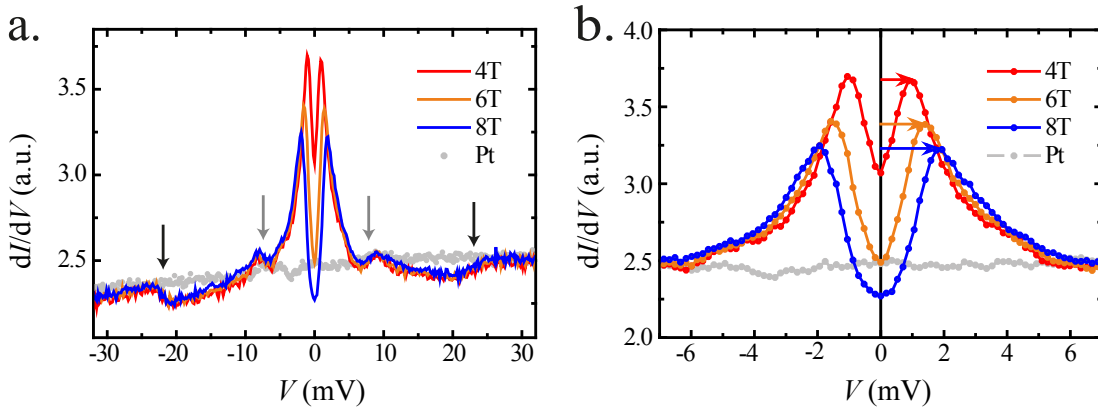


Figure 4.10: **a.**  $dI/dV$  spectra obtained over a CoHD complex while applying an out-of-plane magnetic field, together with a spectrum obtained on clean Pt(111). A parabolic background was subtracted from each spectrum.  $V = -45$  mV,  $I_t = 0.75$  nA,  $V_{mod} = 1$  mV<sub>pp</sub>,  $T = 0.4$  K. **b.** Close-up around the splitting conductance peak. The coloured arrows measure the peak splitting.

$g\mu_B B$ . From the figure it appears quite clearly that this energy is about half the energy of the measured transition for a realistic  $g$  value of 2.38 in the direction of the field.

The same result is found for a  $S = 3/2, D > 0, E = 0$  configuration assuming that its quantization axis lies in the out-of-plane direction (see figure 3.2, **a** in section 3.3, page 22). Instead, the experimental findings can be accounted for by considering a  $S = 3/2, D > 0, E = 0$  configuration with its quantization axis oriented in the surface plane. In this case, the magnetic field is perpendicular to the quantization axis and the ground state doublet splits into two states which are no longer  $m_S = \pm 1/2$  states but rather a linear combination of  $\hat{S}_z^2$  eigenstates. Compared to a pure  $m_S = \pm 1/2$  doublet, the field-induced split is larger, while at the same time the spin-flip transition is allowed since the partial projections of the doublet states onto the  $m_S$  basis fulfils the selection rules  $\Delta m_S = 0, \pm 1$  [34] (see figure 3.2, **b** in section 3.3, page 22).

For such a magnetic configuration, a spin-excitation is expected between the low- $|m_S|$  Kondo state and the high- $|m_S|$  states, at an energy of  $2D$ . Such an excitation, which should manifest itself as a pair of steps in  $dI/dV$ , could not be evidenced in our spectra. Once again, the inelastic features above 6 mV do not display any field-dependence and have already been ascribed to vibrational modes due to their shift upon isotopic substitution. Such a spin-excitation could be masked by the Kondo peak, provided that its energy lies below 6 meV, *i.e.*,  $D \leq 3$  meV, and that its intensity is below 5%, which is realistic for a metallic substrate [41]. The solid blue line and dashed green line in figure 4.11, **a** are fits with  $D = 3$  and 1 meV, respectively. They give a value of 2.38 for  $g$ . One can see that  $D$  values of 3 meV and higher yield a rather straight evolution of the transition energy with field, in excellent agreement with our measurements. Although the fit quality is a little lower for  $D = 1$  meV, it still falls well into the error bars.

In conclusion, our results are compatible with a uniaxial magnetic anisotropy with in-plane hard axis,  $1 < D < 3$  meV, and  $g = 2.38$ . Figure 4.11, **b** shows the behaviour of the two energy levels involved in the Kondo resonance with a magnetic field applied perpendicularly to the hard magnetization axis, for a  $D$  value of 3 meV. Our results could be equally well fitted with  $S = 5/2$ , although with different values for  $g$  ( $g \approx 1.7$ ). However, such a large value for the effective spin appears unconventional for a Co adatom. It is worth mentioning that Configuration Interaction (CI) calculations for a linear  $\text{CoH}_2$  molecule predict a spin  $S = 3/2$  in the ground state [66].

We eventually verified that a finite transverse anisotropy term  $E$  only produces negligible differences in the evolution of the magnetic states with field. Having the quantization axis lying in the surface plane is surprising since the Pt(111) symmetry shows three equivalent in-plane directions. The two H atoms may however considerably alter the threefold symmetry. Another possible interpretation arises when considering an important transverse anisotropy. We note that our data can be equally well fitted with an easy axis out-of-plane ( $D < 0$ , quantization axis out-of-plane) provided that  $E \sim D$ .  $E$  then constitutes an extra free parameter, and the choice of the expression for transverse anisotropy in the spin Hamiltonian is not trivial since

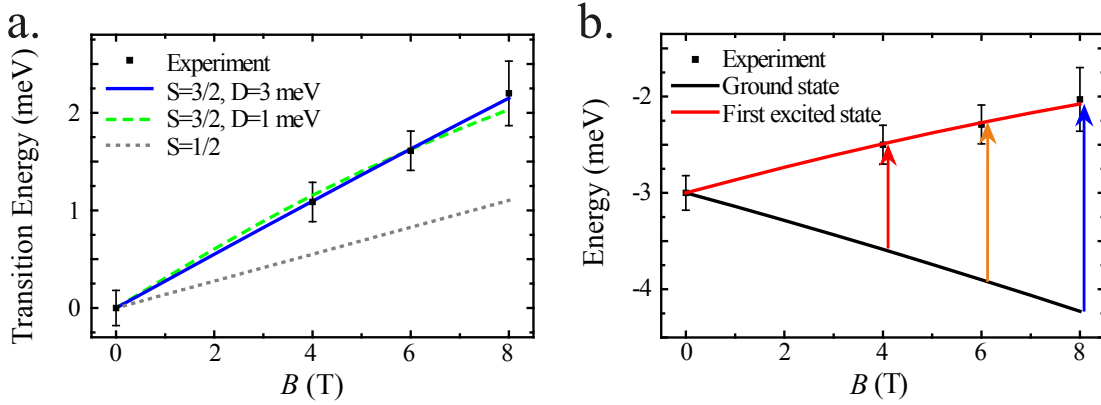


Figure 4.11: **a.** Transition energy measured from figure 4.10, **b** plotted against magnetic field, together with fits from different spin Hamiltonians with realistic values. The error bars correspond to statistical dispersion. **b.** Magnetic ground state and first excited state versus magnetic field, as obtained from the spin Hamiltonian with  $S = 3/2$ ,  $D = 3$  meV, and  $g = 2.38$ . The coloured arrows correspond to the Kondo peak splitting, as in figure 4.10, **b**.

the peculiar symmetry of the system is not known (*i. e.*, is transverse anisotropy defined by the threefold symmetry of Pt(111), by the unknown symmetry of the  $\text{CoH}_2$  complex, or by a combination of both). First-principle calculations and measurements with another technique could allow for a precise determination of the magnetic configuration of the Kondo-system  $\text{CoH}_2/\text{Pt}(111)$ .

We have demonstrated that Co adatoms on Pt(111) can be transformed into a Kondo system upon H adsorption. Among the different  $\text{CoH}_x$  complexes, we have found  $\text{CoH}_2$  to behave as an effective spin  $3/2$  system with positive magnetic anisotropy, thus giving rise to a Kondo effect. Other inelastic features observed in  $dI/dV$  spectra were ascribed to vibrational modes of the whole complex (for  $\text{CoH}$ ) or of the adsorbed hydrogen atoms (for  $\text{CoH}_2$ ).  $\text{Co}/\text{Pt}(111)$  is the very first reported single adatom system displaying a Kondo effect induced by H adsorption. The opposite situation, namely quenching of a Kondo effect upon H adsorption, has already been demonstrated for  $\text{Co}/\text{Cu}(111)$  [67]. It is also interesting to note that although Kondo effect and vibrational modes coexist in  $\text{CoH}_2$ , no replica of the Kondo peak are observed at the vibration energies, in contrast to what has been reported for a tetracyanoquinodimethane (TCNQ) molecule adsorbed on  $\text{Au}(111)$  [68]. Our results clearly show that H adsorption can be exploited as an easy and reversible way to tailor magnetic properties of single atoms.



## 4.2 Magnetic remanence in single adatoms

With such knowledge of the system, and a method to identify and produce clean Co adatoms available, we looked for hypothetical signs of magnetic remanence in single adatoms using spin-polarized STM.

SP-STM requires a magnetic reference. We chose bilayer Co islands, since they are known to display very large spin contrast at known bias voltages [69, 70], and are magnetized perpendicular to the surface, like Co adatoms. Bilayer Co islands were prepared as follows: 0.5 ML of Co was deposited on a clean Pt(111) surface at a flux of  $4.2 \times 10^{-3}$  ML/s and a temperature of 130 K, in a typical base pressure of  $2 \times 10^{-10}$  mbar. The sample was then annealed at 340 K for 10 mins [71]. Figure 4.12, **a** and **d** present STM images of bilayer Co islands as well as subsequently deposited Co adatoms on Pt(111).

In order to confer spin-sensitivity to the STM W tip, it was coated *in situ* with Cr (coverage estimated to 1 ML).<sup>3</sup> No spin-contrast could be observed immediately afterwards and after several mild voltage pulses over the Pt surface, neither in standard STM images nor in  $dI/dV$  images. The tip was then indented into bilayer Co islands until its length increased (meaning that it probably picked some Co from the island). This operation was found to produce tips with a decent level of out-of-plane magnetic sensitivity with a reasonable success rate, even for non-Cr-coated W tips, as shown in figure 4.12, **b** and **c**.

After having prepared a tip yielding a satisfactory level of out-of-plane spin-sensitivity, we looked for spin-contrast over Co adatoms at 0.4 K and biases well below, as in figure 4.12, **d**, and above the expected spin-excitation threshold of 9 meV [42, 57]. The apparent height of every atom was then carefully extracted using a routine that fits a Gaussian peak on every adatom and calculates the difference between the summit of the peak and the average height of a ring surrounding the adatom. Figure 4.13 presents the statistical distributions of heights at  $V = 2$  and 20 mV. Both of these distribution can be reasonably well fitted with a single Gaussian, with almost identical full-width at half-maximum, namely  $0.11 \pm 0.01$  Å at 2 mV, and  $0.10 \pm 0.01$  Å at 20 mV. From these values we can conclude that there is no magnetic contrast over the adatoms in these conditions.

This experiment was repeated several times at  $T = 0.4$  K and with a tip that was previously checked for spin-contrast over bilayer Co islands, yielding similar results. However this set of experiment does not provide a solid conclusion, since no evidence of spin-contrast was found at such low biases on bilayer Co islands either. This tends to indicate that the tips used in these experiments, although displaying strong spin-sensitivity at biases of several hundreds of mV's, probably did not have the adequate DOS to provide enough spin-sensitivity so close to the Fermi level. Other tip preparation methods could be used to try to solve this problem, depositing a thicker layer of Cr on the tip for example.

<sup>3</sup>This very low value reflects the limitation of our set-up regarding in-STM tip-preparation, justifying the need for *in situ* tip-exchange implementation, as presented in section 2.5.2, page 14.

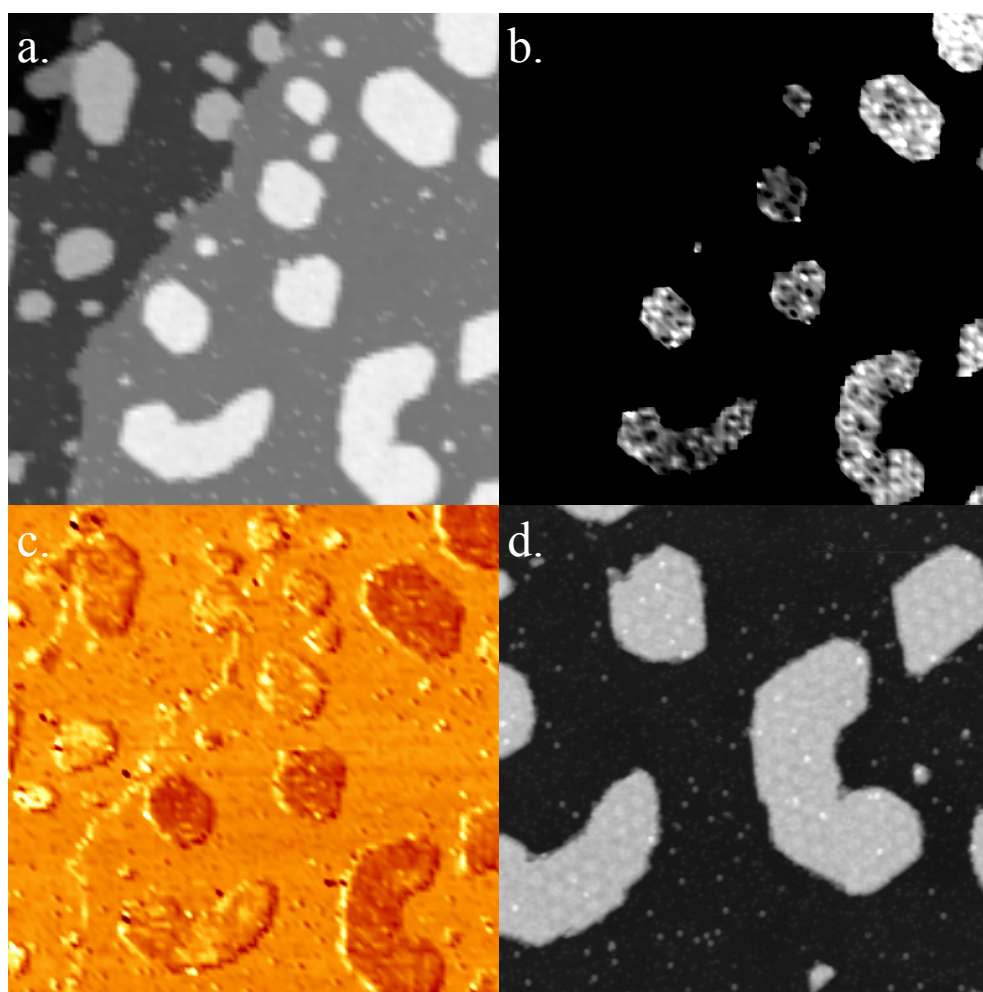


Figure 4.12: **a.** Bilayer Co islands and Co monomers on Pt(111). No spin-contrast can be seen with this contrast settings. Image size:  $100 \times 100 \text{ nm}^2$ .  $V = -800 \text{ mV}$ ,  $I_t = 1 \text{ nA}$ ,  $T = 5.0 \text{ K}$ . **b.** Same STM image, where the contrast range has been reduced to the bilayer Co islands only. A very faint magnetic contrast is visible. **c.**  $dI/dV$  image acquired simultaneously to **a**, displaying a relatively strong spin-contrast. The bilayer islands can readily be separated into two categories, light or dark, depending on the relative orientation of their magnetization compared to that of the tip.  $V_{\text{mod}} = 30 \text{ mV}_{pp}$ . **d.** STM image acquired in the the bottom-right corner of image **a** at a voltage well below the spin-excitation threshold of Co. No tip-change was observed between the acquisition of images **a** and **d**. No evident spin-contrast is visible, neither on the adatoms nor on the bilayer islands. Image size:  $75 \times 75 \text{ nm}^2$ .  $V = 2 \text{ mV}$ ,  $I_t = 75 \text{ pA}$ ,  $T = 5.0 \text{ K}$ .

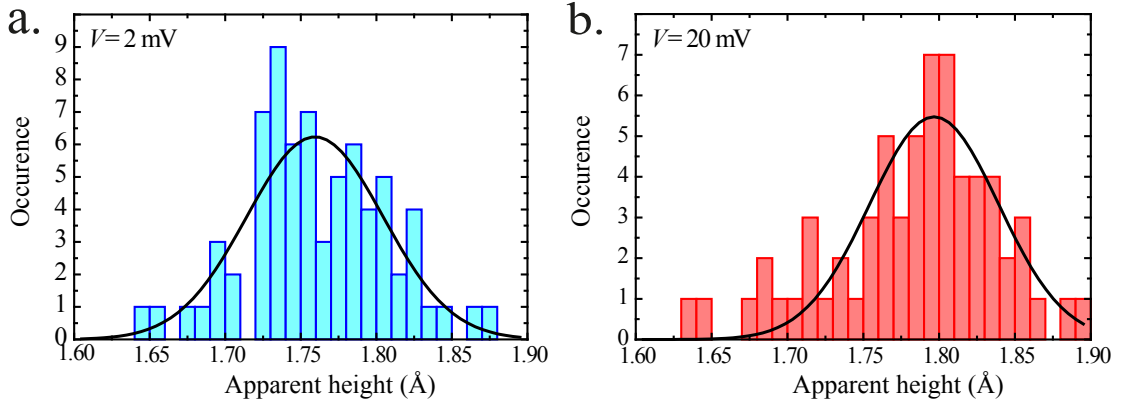


Figure 4.13: Apparent height histograms of clean Co adatoms on Pt(111), measured below and above the theoretical spin-excitation threshold. **a.**  $V = 2$  mV, **b.**  $V = 20$  mV,  $I_t = 75$  pA,  $T = 0.4$  K. These heights were extracted from two images acquired consecutively, right after controlling that the tip was giving a strong spin contrast on bilayer Co islands at  $V = -800$  mV. No tip change was observed between this control and the end of the second image. The solid black lines represent Gaussian fits.

Spin-sensitivity at such low biases is achievable since it has been reported in a couple of publications that appeared during the course of this thesis, once indirectly, studying its effect on spin relaxation dynamics of FeCu dimers on  $\text{Cu}_2\text{N}/\text{Cu}(100)$  at  $V = -1.2$  mV in  $B = 7$  T and  $T = 0.6$  K [37] (using a single Mn atom on a Cu-covered W tip) and directly in the second case, estimated to  $\approx 10\%$  at  $\pm 10$  mV and  $T = 0.3$  K, using a W tip coated with  $\approx 50$  ML of Cr, looking at the temporal evolution with different biases of the height of small Fe clusters on Cu(111) [28]. This second case is of particular interest since it reports magnetic remanence for  $\text{Fe}_5$  clusters on Cu(111) at  $T = 0.3$  K,  $|V| = 2$  mV,  $I = 3$  nA, making  $\text{Fe}_5$  the smallest observed stable magnet to date.

It could also be that the bilayer Co islands themselves do not have a strong magnetic polarization of their DOS close to the Fermi level, and may therefore not constitute an optimal reference for this measurement. Another approach could be attempting to reproduce a reported experiment [59], placing Co atoms at distances between 1 and 5 nm from a monolayer Co island (or stripe), and look for spin-contrast over these adatoms that are magnetically coupled to the island by conduction electrons from the substrate through the Ruderman-Kittel-Kasuya-Yosida (RKKY) interaction [72, 73, 74]. This interaction stabilizes the magnetic moment of the adatoms either parallel or anti-parallel to that of the island depending on the distance between them. These adatoms could then be used as references for spin-contrast, and compared to non-stabilized adatoms.

Another way to tackle the challenge of remanence in Co/Pt(111) is also suggested by [28]: instead of seeking magnetic contrast over large Co islands and acquiring images over adatoms below and above the spin-excitation threshold, one could look for signs of spin-excitations

#### **Chapter 4. Co and Co-hydrides on Pt(111): an attempt at discovering single-adatom magnetic remanence, and an unexpected Kondo effect**

---

over an adatom, carefully monitoring the height  $Z$  at a bias close to the excitation threshold, where excitations with a time constant larger than a millisecond are expected, and re-prepare the tip until such spin-excitations are observed. One could also start with small Co clusters (e.g.  $\text{Co}_5$ ) where remanence is more probable due to a higher anisotropy, and the magnetic moment (and thus spin-contrast) larger, and check whether spin-excitations are still visible on adatoms.

In conclusion, it could be that Co adatoms on Pt(111) are not stable magnets at 0.4 K, possibly due to a transverse anisotropy term introducing quantum tunneling of the magnetization. However our experimental observation did not allow us to conclude in this direction, and magnetic remanence in single adatoms is still an open question.

## 5 Co and Co-hydrides on graphene on Pt(111)

Graphene is expected to be an ideal host for magnetic impurities, as exceptionally high uniaxial anisotropies have been predicted [75, 76, 77], and very small transverse terms are expected for the sixfold adsorption site, potentially yielding very long spin lifetimes, and maybe magnetic remanence at finite temperature for single adatoms. In addition, the electronic and magnetic properties of graphene strongly change upon adsorption or embedding of magnetic impurities [78, 79, 80, 81]. Adsorbates carrying a magnetic moment have been predicted to induce the formation of extended magnetic phases [82], quantum critical Kondo anomalies [83, 84], and have a strong influence on the scattering of spin currents [85].

Although several experimental studies of magnetic adatoms on graphene have been reported [80, 81, 86, 87] during this thesis work, they focused on the electronic properties of the system, and none provided the magnetic properties of the adatoms. The theoretical predictions vary dramatically: for Co adatoms on graphene, spin moments between 1 and  $3 \mu_B$ , and anisotropies of various sign and values have been calculated [75, 77, 88, 89].

We attempted to perform the first experimental determination of the magnetic moment and anisotropy of adatoms on graphene, as a potential candidate to demonstrate remanence. We chose Co as a prototypical magnetic adatom, and Pt(111) as substrate for the growth of graphene, due to their very weak binding [90]. Furthermore, Pt(111) presented the advantage of being a well-characterized substrate for Co adatoms, especially useful to evidence the presence of H contamination.

## **5.1 Graphene/Pt(111): preparation and observations**

Pt(111) was prepared by means of Ar<sup>+</sup> sputtering (300 K, 900 eV, 1.3  $\mu\text{A}/\text{cm}^2$ , 10 min) and flash annealing cycles (1400 K,  $p_{\text{tot}} \leq 5 \times 10^{-10}$  mbar) leading to surface impurity concentrations below 0.5% of ML.

Graphene was grown by both C segregation (1500 K, 1–3 min) and CVD (10 Langmuir C<sub>2</sub>H<sub>4</sub> at 1230 K, flash to 1400 K). Figure 5.1 presents STM images of four different types of graphene patches obtained with these two methods. All these images present different moiré patterns caused by the misfit with the substrate [91]. Graphene on Pt(111) is known to exhibit a variety of moiré structures [92, 93]. The first growth method resulted in small patches with 10–100 nm diameter and small moiré unit cells, whereas the second one yielded up to several  $\mu\text{m}$ -large domains with larger moiré unit cells. The results presented in the following were principally obtained on the moiré structure with a period of (4×4) graphene unit cells, shown in figure 5.1, **b**, however, they are also representative for Co adatoms on the other superstructures.

Figure 5.1, **b** and **c** display a hexagonal lattice of protrusions. There is one protrusion per graphene unit cell, in line with former observations [92, 94] (see also next chapter). Therefore the substrate binding difference between the two C atoms in the unit cell is very small and the contrast is dominated by the difference between C<sub>6</sub> rings and sixfold hollow sites. Contrary to what would be expected from the geometry, the latter are imaged as protrusions with this peculiar tip and tunnel parameters. Conversely, figure 5.1, **a** and **d** exhibit a hexagonal lattice of depressions instead of protrusion, which can be identified as the sixfold hollow sites from the same argument. The difference of contrast between these two sets of images is attributable to a different tip orbital structure.

We intentionally prepared sub-monolayer coverages of graphene for several reasons: firstly, the Pt(111) surface can be used for tip-preparation and as a reference for STS. Secondly, the density of deposited adatoms on graphene and Pt can be compared, in order to verify that atomic diffusion is also blocked on graphene. Thirdly, owing to our knowledge of Co hydrides on Pt(111) (see previous chapter), we can estimate the amount of H to which our sample has been exposed looking at Co on Pt(111).

## **5.2 Co/G/Pt(111): four types of complexes**

Co was deposited *in situ* at 16 K and  $p_{\text{tot}} = 8 \times 10^{-10}$  mbar using a commercial electron beam evaporator with a thoroughly degassed 99.995% purity Co rod. Test depositions at 2 K yielded identical results. At both temperatures the adsorbates are immobile, as can be seen by direct comparison between the density of adsorbates on graphene and Pt. Therefore growth is statistical and leads, at the chosen coverage of  $(5.0 \pm 0.5) \times 10^{-3}$  ML.

After evaporating Co onto graphene, one identifies four species at the surface. They clearly distinguish themselves by their apparent height and inelastic conductance steps, as shown

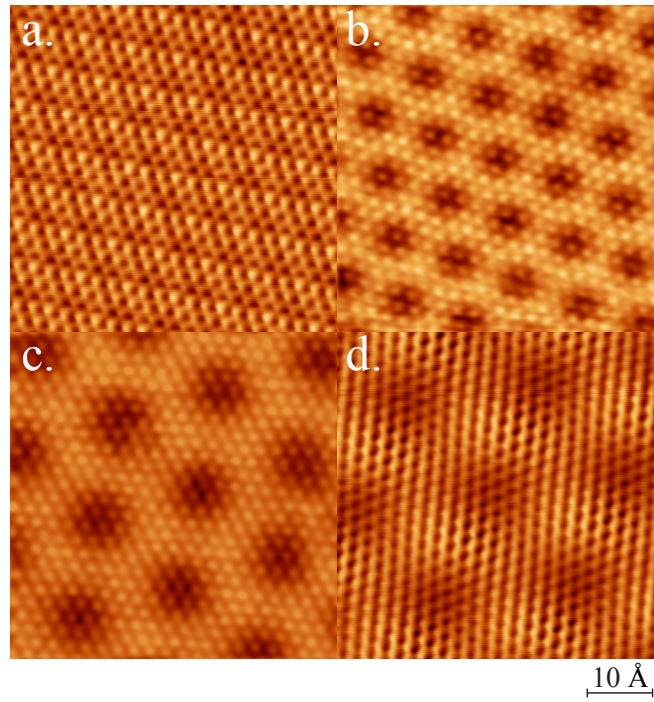


Figure 5.1: STM images of four graphene patches on Pt(111) displaying different moiré patterns. In images **a** and **d**, the centres of the graphene  $C_6$  rings are imaged as depressions, whereas in images **b** and **c**, they are seen as protrusions. Size of the images:  $5 \times 5 \text{ nm}^2$ . Temperature of acquisition:  $T = 4.5 \text{ K}$ . **a.**  $V_t = -50 \text{ mV}$ ,  $I_t = 0.5 \text{ nA}$ . **b.**  $V_t = -1 \text{ mV}$ ,  $I_t = 8 \text{ nA}$ . **c.**  $V_t = -50 \text{ mV}$ ,  $I_t = 0.1 \text{ nA}$ . **d.**  $V_t = -50 \text{ mV}$ ,  $I_t = 0.5 \text{ nA}$ .

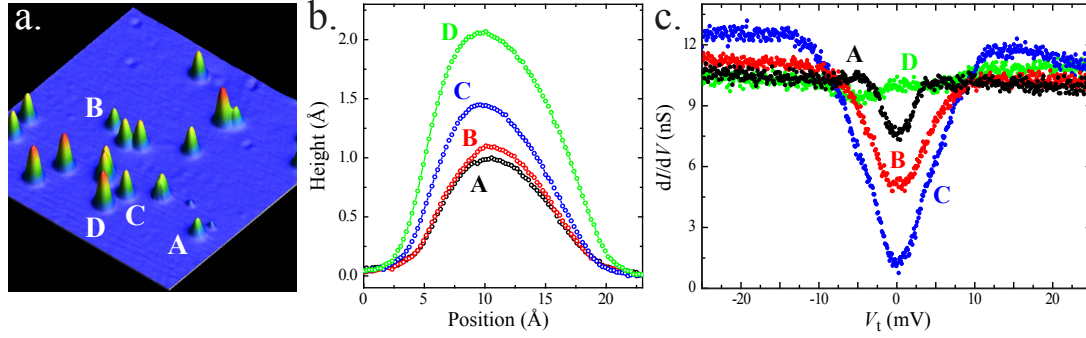


Figure 5.2: **a.** Four different types of Co complexes on graphene, with distinct apparent heights.  $V_t = -100$  mV,  $I_t = 50$  pA,  $T = 4.5$  K. **b.** Profile of the four complexes.  $V_t = -25$  mV,  $I_t = 50$  pA,  $T = 4.5$  K. **c.** Characteristic STS spectra of the four species, displaying a variety of inelastic conductance steps.  $V_t = -25$  mV,  $I_t = 250$  pA,  $V_{\text{mod}} = 1$  mV  $pp$ ,  $T = 4.5$  K.

in figure 5.2, **a**, **b**, and **c**. We label them A, B, C and D, in order of increasing height. Their relative abundance for a freshly prepared sample is shown in figure 5.3, **a**. Our experience with Co/Pt(111) (see previous chapter) lead us to immediately suspect a H contamination in this case as well, considering that a significant part of the Co adatoms sitting directly on Pt were hydrogenated.

In order to verify that these different types indeed correspond to different Co hydrides and pure Co, we exposed the sample to molecular H. A control experiment was done first, exposing the sample to the residual gas ( $p = 7 \times 10^{-10}$  mbar) from which the STM is usually protected by the cold radiation shields, which have to be opened for H exposure, during 60 s. This led to a noticeable decrease in the abundance of type D, and a very small increase of the other three types, as shown in figure 5.3, **b**.

Direct exposure of the sample to  $4 \times 10^{-9}$  mbar of  $H_2$  for  $\Delta t = 10$  s was found to result in a very large increase in the abundance of type A, a very small increase for type B, and a dramatic decrease of type C and D, the latter having almost disappeared. We thus conclude that we naturally have Co hydrides, that type A is the most hydrogenated of them, and type D the least, possibly pure Co.

As for  $CoH_x$  complexes on Pt(111), deprotonation can be induced by voltage pulses. Type A is readily transformed into type B applying a voltage pulse of  $|V_t| = 155 \pm 11$  mV, further into C with  $|V_t| = 180 \pm 7$  mV, and finally into D with  $|V_t| = 454 \pm 31$  mV. These values apply to a tunnel current of 100 pA. Further increase of the pulse amplitude leads to a jump of the adatom to another site, without altering its type D character. Figure 5.4 presents the H-desorption voltages versus current for the three types, and allows to conclude on a single-electron process in every case.

Figure 5.5, **a** shows that type A has a triangular structure, in striking agreement with the



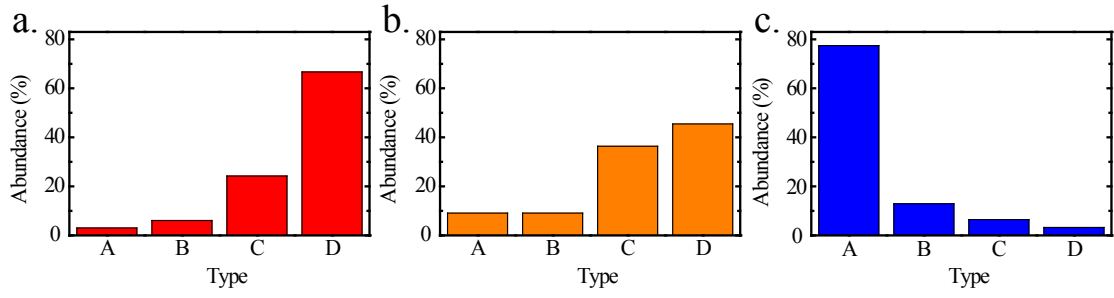


Figure 5.3: Statistical distribution of the four different types: **a.** for a freshly prepared sample, **b.** after exposing the sample to the residual gas of the vacuum chamber (radiation shields open, sample in transfer position) for  $\Delta t = 1$  min, **c.** after dosing  $H_2$  while the sample is in the same position as in **b.** The complete inversion of the distribution upon exposure to  $H_2$  allows us to identify type A as the most hydrogenated species, and D as the least.

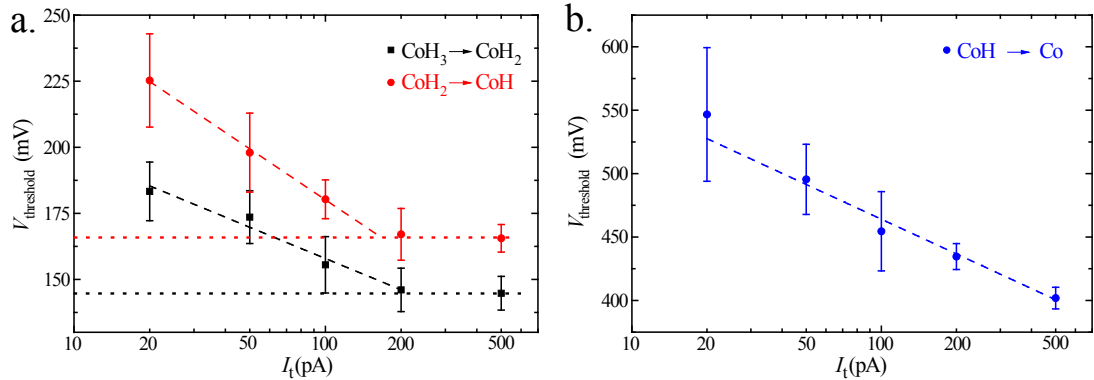


Figure 5.4: H-desorption threshold voltages versus current. **a.** Threshold voltages to switch  $CoH_3$  into  $CoH_2$  and  $CoH_2$  into  $CoH$ . **b.** Threshold voltages to remove the last H atom from  $CoH$ . The dashed lines in **a** are exponential fits to the first four points, and the dotted lines evidence the saturation at higher stabilization current, as a guide to the eye (average over 5 to 20 atoms,  $T = 4.5$  K). In **b**, the dashed line corresponds to an exponential fit of the 5 data points (average over 20 atoms,  $T = 4.5$  K). These plots were obtained in the same way as those presented in figure 4.4 for deprotonation of Co/Pt(111) (page 38), and display a very similar behaviour. Here as well, we conclude that de-hydrogenation occurs through a single-electron process.

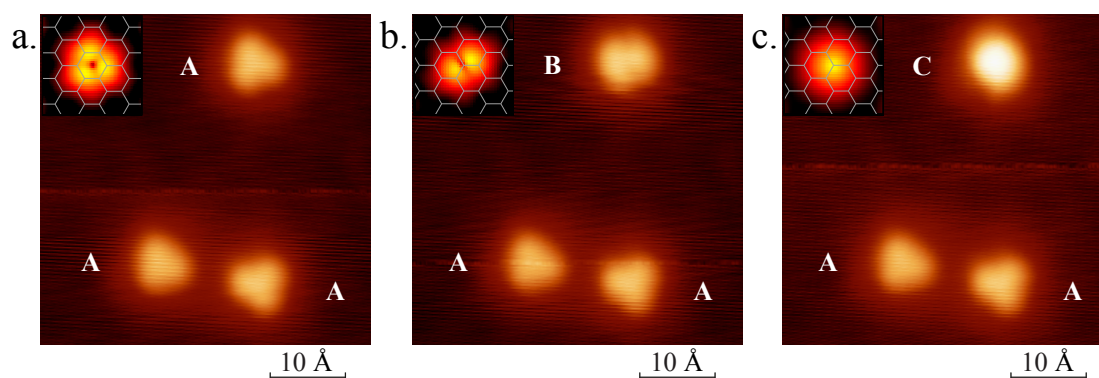


Figure 5.5: **a.** Three  $\text{CoH}_x$  complexes imaged as triangles. The different orientation of the two triangles on the bottom rules out the interpretation of these triangular shapes as an artifact coming from the shape of the tip. **b.** and **c.** Successive deprotonation of the upper Co complex by voltage pulses.  $V_t = -100$  mV,  $I_t = 50$  pA,  $T = 0.4$  K. The triangular shape successively turns into a two-lobe structure (**b**) and a circular structure (**c**). Insets: Simulated STM images of the corresponding  $\text{CoH}_x$  complexes, obtained from first-principle calculations (details in the text). The agreement between the real and simulated images allows for the identification of type A as  $\text{CoH}_3$ , type B as  $\text{CoH}_2$ , and type C as  $\text{CoH}$ . Calculations performed by Dr. G. Autès and Prof. O. V. Yazyev.

simulated STM image of  $\text{CoH}_3$  shown as inset. The upper adsorbate in figures 5.5, **a**, **b** and **c** has successively been transformed with voltage pulses, while the lower two adsorbates remained unchanged in nature and appearance, proving that the tip apex did not change in this experiment. Type B is imaged as two distinct protrusions, while type C as a single one, both in excellent agreement with the simulated STM images for  $\text{CoH}_2$  and  $\text{CoH}$ , see insets. The ensemble of these observations unequivocally identifies the species A, B, and C, as  $\text{CoH}_3$ ,  $\text{CoH}_2$ , and  $\text{CoH}$ , and species D as clean Co.

Figure 5.6, **a.** shows three clean Co adatoms (type D) on graphene, which displays a similar moiré pattern as in figure 5.1, **b.** A close-up of one Co adatom is shown together with the atomically resolved graphene lattice in figure 5.6, **b.** From the extrapolation of the graphene lattice onto the vicinity of the adsorbate, one sees that its apex is located on the sixfold hollow site. This adsorption site is found as the lowest energy configuration in our calculations, and the simulated STM image shown in the inset agrees very well with experiment. The lateral extent of the adsorbate is with a full width at half maximum (FWHM) of  $9.0 \text{ Å}$ , in perfect agreement with  $8.3 \text{ Å}$  found with the same tip and tunnel parameters for  $\text{Co}/\text{Pt}(111)$ , where the atoms appear lower by  $1.0 \text{ Å}$  (see figure 5.7). Therefore we can conclude that the adsorbate and the electron charge are very well localized.

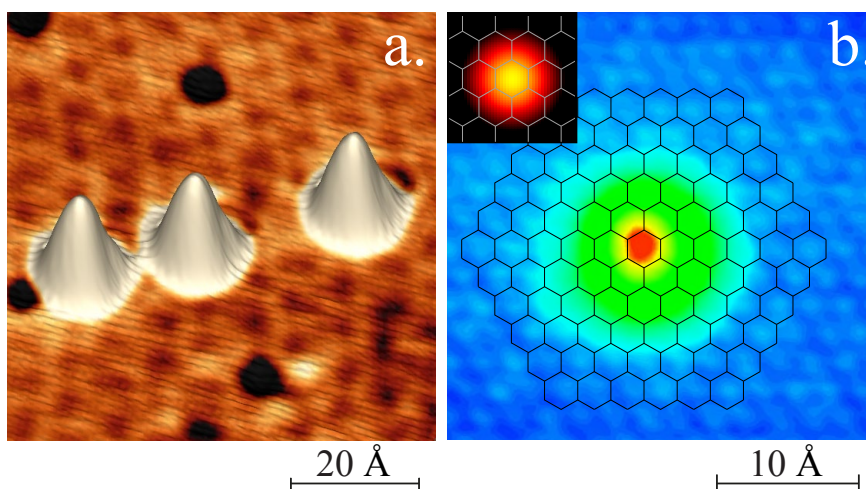


Figure 5.6: Co atoms adsorbed on graphene/Pt(111). **a.** STM image of three Co adatoms.  $V_t = -20$  mV,  $I_t = 1$  nA,  $T = 1.7$  K. **b.** Co adsorbs on the sixfold hollow site as inferred from the lateral position of the adsorbate apex with respect to the atomically resolved C-lattice, sketched in black.  $V_t = -50$  mV,  $I_t = 100$  pA,  $T = 4.5$  K. Inset: DFT confirms this site and leads to the shown simulated STM image.

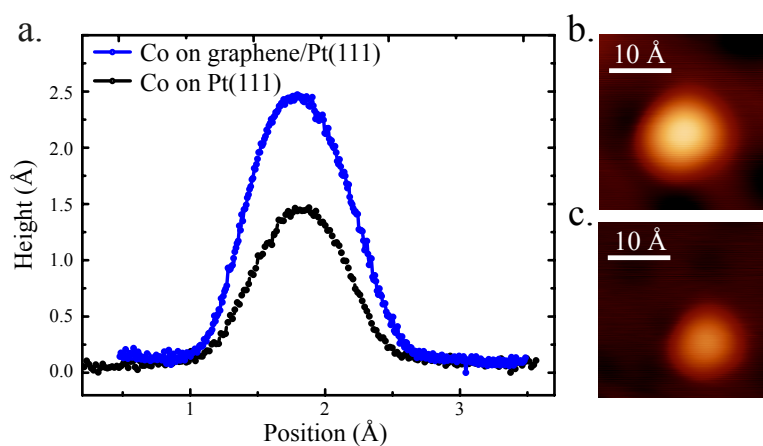


Figure 5.7: Comparison between the appearance of Co adatoms on graphene and on Pt(111). **a.** Profile of a Co adatom on graphene and on Pt obtained from a single STM image acquired at the frontier of a graphene patch. Close-up of the Co adatoms sitting on graphene (**b.**) and on Pt (**c.**) used to produce the profiles shown in **a.** Imaging parameters:  $V_t = -100$  mV,  $I_t = 100$  pA,  $T = 4.5$  K.

### 5.3 Co/G/Pt(111): Magnetic properties

The differential conductance of clean Co monomers reveals clear steps at  $\pm 8$  mV, as becomes evident from inspection of figure 5.8, **a**. These steps progressively split in increasing out-of-plane magnetic fields, what is best seen in the second derivative  $d^2I/dV^2$  shown in figure 5.8, **b**. Therefore, we conclude that they are due to spin-excitations [29] (see section 3.4, page 25). The field-dependent threshold energies  $E_{\text{step}}$  averaged over 26 Co adatoms are presented in figure 5.8, **d**. The spin-excitation energies can be rationalized by the spin Hamiltonian of equation 3.12, page 22:

$$\hat{\mathcal{H}}_{\text{spin}} = g_{\mu\nu}\mu_B\hat{\mathbf{S}} \cdot \vec{B} + D\hat{S}_z^2$$

The presence of two degenerate spin-excitations that shift in opposite directions with magnetic field implies transitions between a singlet and a doublet state. The doublet could in principle either be the ground state or the excited state. In the case of excitations from a doublet ground state, the external field would split the doublet into two non-degenerate states leading to the depopulation of the higher-lying one. Therefore, only a single spin-excitation should be measured at low temperature and high external field [41]. Conversely, if the ground state is a singlet, two spin-excitations with comparable amplitude should be observed, as in the present case (see figure 5.8, **a**). This allows us to assign a positive value to the uniaxial anisotropy parameter  $D$ , as well as an integer value for the effective spin. Since a free atom of Co has a spin of  $3/2$ , we tentatively assign a value of  $S = 1$  to Co/graphene. This is confirmed by our first-principle calculations finding an electronic configuration with  $S = 1$  (see figure 5.8, **c**). Co adatoms in their magnetic ground state have therefore  $m_S = 0$ , and can be excited into two Zeeman-split  $m_S = \pm 1$  states, as illustrated in figure 5.8, **e**.

Fitting the field-dependent excitation energies of figure 5.8, **d**, we obtain  $D = 8.1 \pm 0.4$  meV and  $g = 2.2 \pm 0.4$ , close to the free electron  $g$  factor of 2.0. This gives a total magnetic moment of  $(2.2 \pm 0.4) \mu_B$  and a magnetic anisotropy energy  $K = -DS_z^2 = -8.1 \pm 0.4$  meV.

LDA+ $U$  calculations performed by Dr. G. Autès and Prof. O. V. Yazyev for Co on free-standing graphene show an in-plane easy axis, an anisotropy value of  $K = -9.55$  meV and a local magnetic moment of  $\mu_S = 1.84 \mu_B$ , in good agreement with our experimental findings. They also confirm that the effect of the Pt(111) substrate on the magnetic properties of Co adatoms is very weak, as shown in figure 5.9, and can safely be neglected in the present case, assuming a graphene-Pt distance of  $3.70 \pm 0.05$  Å as measured in Low-Energy Electron Diffraction (LEED) [95].

These first-principle calculations were performed within the DFT framework employing the local density approximation with a mean-field Hubbard correction (LDA+ $U$ ) [96, 97], as implemented in the QUANTUM-ESPRESSO package [98]. A Hubbard  $U = 4$  eV was chosen for Co in agreement with previous calculations [77]. Spin-orbit effects were accounted for

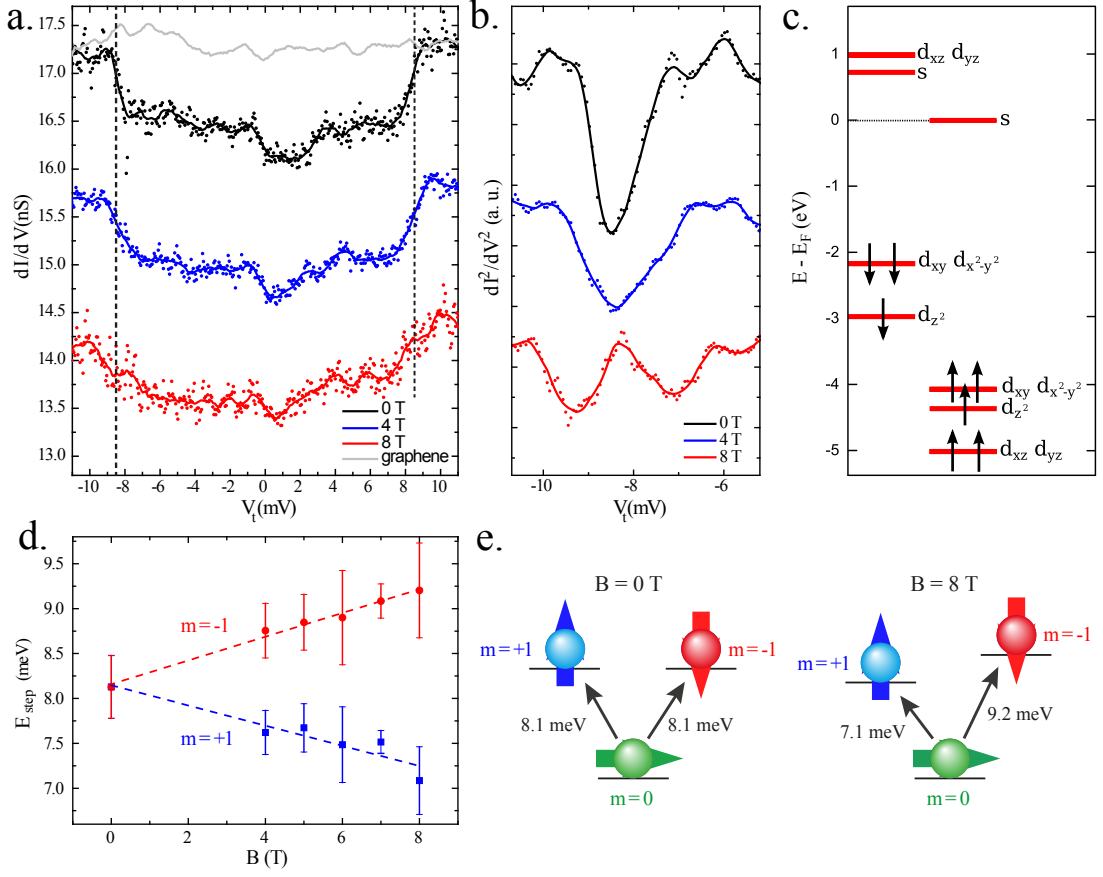


Figure 5.8: Magnetic moment and anisotropy of Co atoms on graphene. **a.** Field-dependent  $dI/dV$  demonstrating the magnetic origin of conductance steps at  $\pm 8.1$  mV. Dots: raw data, lines: smoothed,  $V_t = -15$  mV,  $I_t = 250$  pA,  $V_{\text{mod}} = 200 \mu\text{V}_{pp}$ ,  $T = 0.4$  K. **b.**  $d^2I/dV^2$  of left-hand conductance step in **a** showing its Zeeman splitting. **c.** DFT-calculated spin-dependent energies and filling of Co 3d and 4s levels hybridized with graphene. Calculations performed by Dr. G. Autès and Prof. O. V. Yazyev. **d.** Field-dependent spin-excitation energies averaged over 26 adatoms (error bars show standard deviation). **e.** Schematic of the magnetic states of Co/G/Pt(111). An external out-of-plane field lifts the excited state degeneracy leading to the observed Zeeman splitting of the spin-excitation energies.

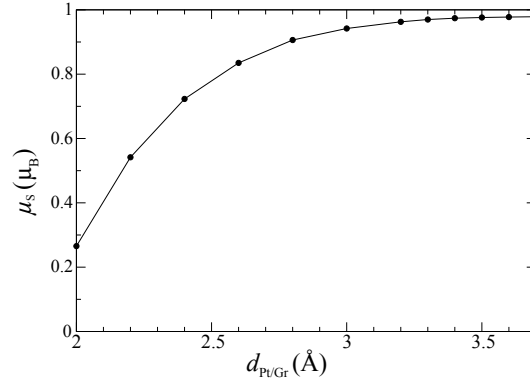


Figure 5.9: Magnetic moment of the Co adatom as a function of the distance between the graphene layer and the Pt substrate, obtained from first-principle calculations performed by Dr. G. Autès and Prof. O. V. Yazyev. Due to the increased complexity of the system, the calculations were only done in the LDA framework, thus yielding lower magnetic moments. The experimentally determined distance range from 3.3 [100] to  $3.70 \pm 0.05$  Å [95].

using the fully relativistic norm-conserving pseudopotentials acting on valence electron wavefunctions represented in the two-component spinor form [99]. The  $\text{CoH}_x$ ,  $x \in \{0, 1, 2, 3\}$ , adsorption complexes were placed in a  $(4 \times 4)$  supercell of graphene and the structures were fully relaxed. The magnetic anisotropy energy was obtained from the difference of total energies of the out-of-plane and in-plane spin configurations. The first-principle simulated STM images show the tunnel current at a constant height of  $z = 4$  Å above the Co adatom and use the Tersoff-Hamann approximation [11] (see section 2.2, page 6). The atomic spin moment and the atomic configuration of the Co adatom were obtained by projecting the wavefunctions of the total system onto atomic orbitals of the Co atom.

The spin Hamiltonian we used does not include a transverse anisotropy term. This is justified by the symmetry of the graphene lattice. For the hexagonal symmetry, the first transverse anisotropy term is of sixth order.  $S$  being 1, only the terms up to second order have to be considered [101], therefore the anisotropy is, to a very good approximation, purely uniaxial. This peculiar energy landscape gives no in-plane preferential orientation, we thus have a hard axis anisotropy with all in-plane directions of  $S$  being degenerate.

The negative anisotropy  $K$  has a surprisingly large value: it is comparable with the record value of  $K = 9.3 \pm 1.6$  meV measured for Co/Pt(111) [57], and is the absolute record for a single adatom with hard axis anisotropy. This large magnetic anisotropy is mostly an effect of the hybridization between Co and graphene states, in contrast to the Co/Pt(111) system where such a high anisotropy originates from the large spin-orbit coupling of the heavy Pt atoms. Such a magnetic configuration also corresponds to one of the possible scenarios identified for Co adatoms on graphene in a recent DFT study [77].

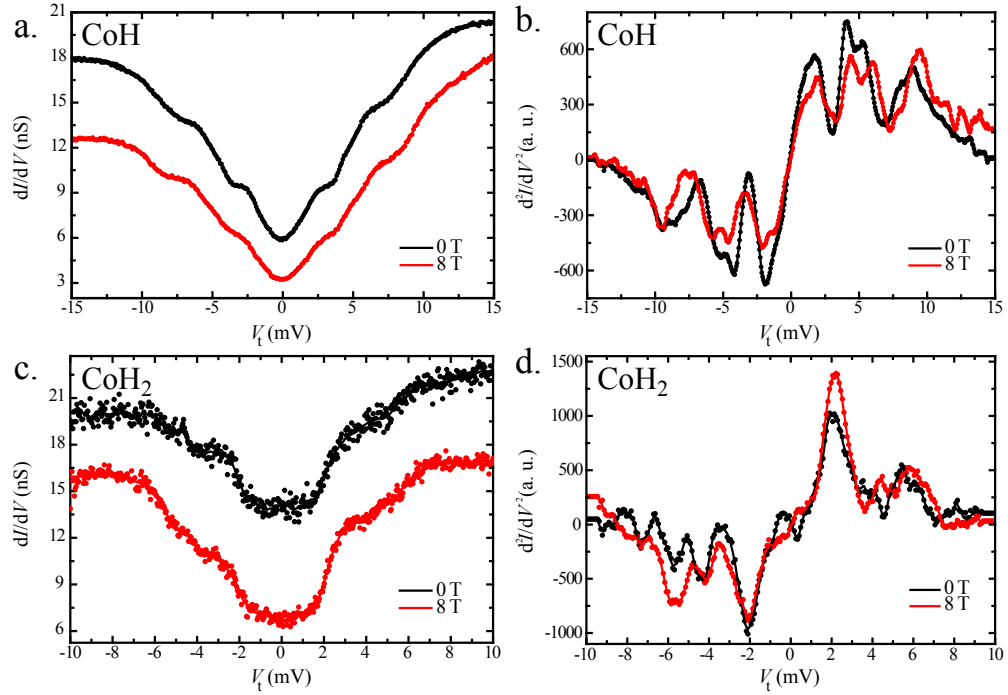


Figure 5.10: **a.** Differential conductance spectra of CoH at 0 and 8 T out-of-plane. Average over 7 atoms,  $V_t = -15$  mV,  $I_t = 200$  pA,  $V_{\text{mod}} = 300 \mu\text{V}_{pp}$ ,  $T = 0.4$  K. **b.** Numerical derivative of **a.** **c.** Differential conductance spectra of  $\text{CoH}_2$  at 0 and 8 T out-of-plane. The 0 T spectrum was acquired on top of a single complex, the 8 T one is the average of spectra taken for two complexes.  $V_t = -20$  mV,  $I_t = 100$  pA,  $V_{\text{mod}} = 200 \mu\text{V}_{pp}$ ,  $f = 611$  Hz,  $T = 0.4$  K. **d.** Numerical derivative of **c.** For both CoH and  $\text{CoH}_2$ , although the shape of the inelastic features seem to change a little with the field, most probably due to small changes of the tip, their position is not modified, ruling out a possible magnetic origin. They must therefore correspond to vibrational modes.

## 5.4 $\text{CoH}_x$ ( $x=1,2,3$ ): vibrational and magnetic properties

We finally investigated the origin of the different spectroscopic features of  $\text{CoH}_x$  ( $x = 1, 2, 3$ ). For CoH and  $\text{CoH}_2$ , they are not affected by magnetic fields up to 8 T, as shown in figure 5.10, and were thus attributed to vibrational modes of the complexes [18, 65], as in the case of CoH/Pt(111) (see section 4.1.4, page 43).

The single conductance step of  $\text{CoH}_3$  splits into a pair of comparable amplitude steps in a finite magnetic field, as one can see in figure 5.11, **a**. This behaviour is very similar to that observed for clean Co, although the steps are much more pronounced and lie at a significantly lower energy. Performing the same type of analysis for this complex (see figure 5.11, **b** and **c**), we find, for an effective spin  $S = 1$ , a uniaxial anisotropy parameter  $D = 1.7 \pm 0.05$  meV and a Landé  $g$  factor  $g = 2.19 \pm 0.13$ . The much larger amplitude ( $\sim 30\%$  instead of  $\sim 5\%$  for pure Co) indicates a significantly larger cross section for the spin excitation in this case.

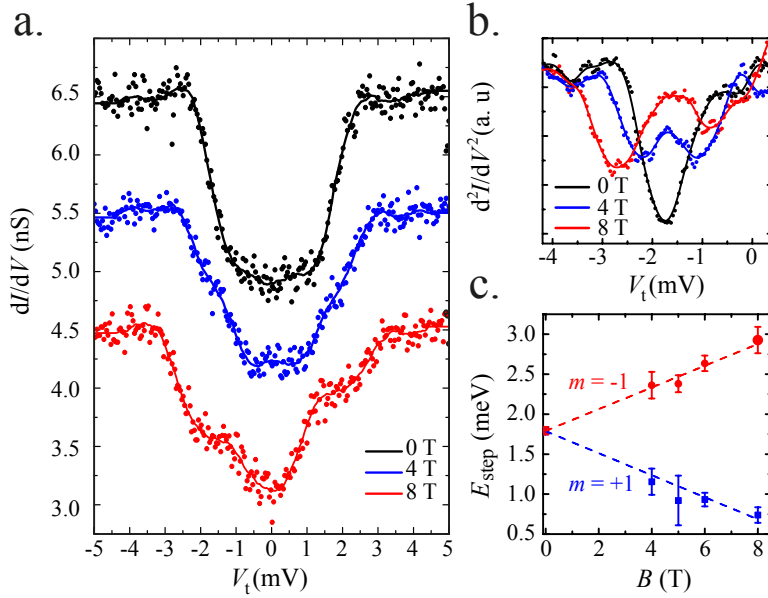


Figure 5.11: Spin-excitation of  $\text{CoH}_3$  on graphene. **a.** Field-induced splitting of the conductance steps.  $V_t = -20$  mV,  $I_t = 100$  pA,  $V_{\text{mod}} = 200 \mu\text{V}_{pp}$ ,  $T = 0.4$  K. **b.** Numerical derivative of the negative bias part of **a** showing each step as a minimum. **c.** Zeeman splitting of spin-excitation energies averaged over 15  $\text{CoH}_3$  complexes (error bars show standard deviation).

In conclusion, we have performed the first experimental determination of the magnetic moment and anisotropy of transition metal adatoms on graphene. A very high uniaxial anisotropy energy of  $D = 8.1 \pm 0.4$  meV and a magnetic moment of  $(2.2 \pm 0.4) \mu_B$  were found and confirmed by fully-relativistic DFT calculations. Magnetic anisotropy in graphene is peculiar, in the sense that it is mostly an effect of the crystal field.

Co adatoms have positive uniaxial anisotropy, and can therefore not exhibit magnetic remanence. However, that may not be the case for other elements, dimers and small clusters, justifying further experimental investigations of transition metal adatoms on graphene.

Transverse anisotropies for systems with low effective spins are very small in this system, due to the high symmetry of the adatom environment. Consequently, quantum tunneling of the magnetization can be neglected. These properties could be exploited to engineer atomic structures with high temporal stability of magnetic moments over thermal fluctuations and quantum tunneling.

Moreover, we demonstrated a direct and reversible way to switch the anisotropy energy between  $8.1 \pm 0.4$  meV and  $1.7 \pm 0.05$  meV, with  $\text{H}_2$  exposure and deprotonation through voltage pulses. It is a rather straightforward process, these two values respectively corresponding to fully-cleaned Co and H-saturated Co complexes. Furthermore, deprotonation can be performed locally on a single complex.



#### 5.4. $\text{CoH}_x$ ( $x=1,2,3$ ): vibrational and magnetic properties

---

Finally, it is also important to note that H is the dominant contaminant in most low-temperature UHV systems, and we expect that similar hydrogenation happens for most metallic adatoms, and not only for Co. One should therefore seriously consider the issue of H-contamination when measuring metallic adatoms, especially on graphene. This is particularly important for spatially-averaging techniques, such as XMCD for example, where the measured properties could easily correspond to a mixture of species.



## 6 Mono- and bilayer graphene on Ru(0001): Structure, stacking, and distortions

The previous chapter demonstrated the relevance of graphene as a substrate for magnetic nanostructures. For many potential applications, large defect-free patches of graphene are required. This can be achieved by growing graphene on the surface of several metallic single crystals, what also offers the possibility to tune the properties of graphene through charge transfer [102], strain [103], hybridization with a magnetic substrate [104], proximity-effect with a superconducting material [105], *etc.* Furthermore, a good understanding of graphene-metal interfaces is crucial for most electronic and spintronic applications that need to electrically contact graphene. A lot of efforts are also currently made to transfer graphene from one substrate to another one, and to intercalate clusters and thin films between the graphene and the substrate it was grown on. All these considerations justify the study of graphene grown on metallic substrates for fundamental research and technological applications.

Graphene on Pt(111), as presented and exploited in the previous chapter, has the advantage of exhibiting a very weak graphene-substrate coupling [90], and thus almost behaves as free-standing graphene. However, it also has a major disadvantage: it tends to form small patches presenting a variety of moiré structures and a high density of defects [92, 93].

We chose to investigate graphene grown on Ru(0001), where perfect monolayers with a single, large moiré pattern are readily produced [106, 107]. Although monolayer graphene is well known to hybridize strongly with Ru and thus lose its gapless, linearly dispersing band structure [108], a second monolayer of graphene grown on top of it retains most of its free-standing graphene character [109]. Moreover, an important spatial modulation of the hybridization between graphene and Ru was found to coincide with the moiré pattern [107, 110, 111]. Graphene on Ru(0001) thus constitutes an interesting system for the study of the effects of this hybridization.

Despite the large number of experimental and theoretical studies devoted to graphene on Ru(0001), some points remained unclear regarding the structure of this system, with lack of consensus for monolayer graphene (1 ML) [106, 107, 110, 112, 113, 114, 115, 116] and limited

data for bilayer graphene (2 ML) [114, 117]. We therefore undertook a precise determination of the moiré structure of 1 and 2 ML graphene on Ru(0001), as well as of their relative stacking.

We also addressed the issue of the very large lattice distortions observed with STM. Such distortions have already been reported and qualitatively explained as an imaging artefact [118]. However, an in-depth study of this issue was justified by the importance of strain regarding the properties of graphene. Variations in the local strain are held responsible for phenomena like the redistribution of charge density, the opening of energy gaps or the formation of giant local pseudo-magnetic fields [103, 119, 120], and strain engineering has recently been proposed as a possible way to tailor the properties of graphene [103].

### 6.1 Two different stackings for bilayer graphene/Ru(0001)

Our graphene/Ru(0001) sample was prepared by Dr. M. Papagno at the Elettra synchrotron radiation facility in Trieste, Italy, using CVD: The Ru(0001) crystal was cleaned by repeated cycles of Ar<sup>+</sup> sputtering and annealing at 1500 K. The clean Ru(0001) surface was then exposed to 10<sup>5</sup> L ( $2.5 \times 10^{-4}$  mbar for 530 s) of C<sub>2</sub>H<sub>4</sub> at a temperature of 1600 K. It was transported from Trieste to Lausanne in air and flash-annealed to ~ 800 K in our STM set-up, in a base pressure below  $1 \times 10^{-9}$  mbar.

Although some residual contamination from exposure to air remained, most of the surface appeared to be clean, as can be seen in figure 6.1, **a**. This STM image presents three different types of surfaces. The largest area displays the regular hexagonal array of protrusions readily identified as the moiré formed by monolayer graphene (1 ML) on Ru(0001) [106]. The second largest area (right-hand side), representing  $25 \pm 5\%$  of the total surface, appears very flat. The third type of surface (bottom-left part of the image), which covers about  $12 \pm 2\%$  of the sample, is characterized by an incomplete moiré pattern with a maximum corrugation of  $1.10 \pm 0.05$  Å. Figure 6.1, **b** is a line profile of these three regions. Analysing their relative apparent height, we conclude that the two minor regions must correspond to bilayer graphene (2 ML), and will be referred to as "2 ML-f" and "2 ML-c" respectively, standing for "flat" and "corrugated" bilayer graphene. 2 ML-c, which has already been observed in STM [117], lies  $3.3 \pm 0.1$  Å above 1 ML graphene, what corresponds to the distance between the atomic layers in graphite. Graphite being AB-stacked, this constitutes a first indication that so must 2 ML-c be [109, 117, 121]. 2 ML-f, on the other hand, lies only  $2.1 \pm 0.1$  Å above 1 ML graphene, and should therefore not be AB stacked. We also measure a height difference of  $2.2 \pm 0.1$  Å between two 1 ML graphene terraces, which corresponds very well to the measured value of 2.14 Å for the interplane distance in Ru [122].

Figure 6.2, **a** is an STM image acquired over a frontier between 1 ML and 2 ML-f graphene. The presence of a substrate step in the image could readily be excluded from the analysis of the surrounding area in a larger scale image. A hexagonal array of depressions for 1 ML, or protrusions for 2 ML-f, can be resolved and related to their respective atomic honeycomb network. In the case of 1 ML graphene, the fact that a single hexagonal lattice is resolved

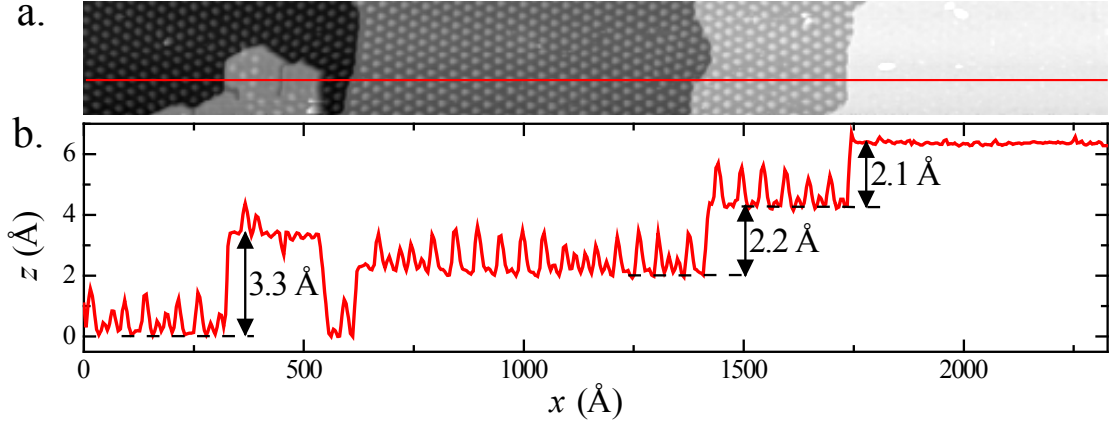


Figure 6.1: **a.** STM image of graphene on Ru(0001), displaying mono- and bilayer domains. Image size:  $2320 \times 283 \text{ Å}^2$ .  $V_t = -3 \text{ V}$ ,  $I_t = 75 \text{ pA}$ ,  $T = 4.5 \text{ K}$ . **b.** Apparent height profile along the red line displayed in **a**.

implies that the local minima must correspond to the centres of the carbon rings. Otherwise, if the local minima were associated with one of the two subsets of C atoms, referred to as  $C_a$  and  $C_b$ , they would form two different hexagonal lattices, each one occupying one half of the moiré cell [106, 111]. Concerning 2 ML-f, the same argument implies that the protrusions should correspond to the ring centres. Their hexagonal shape actually evokes the honeycomb itself. Having the two atomic lattices in the same image enables us to deduce their relative stacking: tracing lines along the high symmetry directions of 1 ML graphene (plotted in yellow in figure 6.2, **a**), or hexagons over the carbon rings (in red, cyan and green in the same figure), we conclude that 2 ML-f is AA-stacked on top of 1 ML graphene. This type of stacking has already been observed for Li-intercalated graphite [123], oxidized C nanofilms [124], as well as for DC-enhanced Plasma CVD-grown graphite on diamond (111) films [125], but never on a transition metal surface.

The measured height difference between 2 ML-f and 1 ML is much smaller than the theoretical value expected for an AA stacking bound by van der Waals interaction, namely  $3.66 \text{ Å}$  [126]. A covalently bound AA stacking has also been predicted by first-principle calculations to be energetically less favourable than a van der Waals bound AB stacking by only  $0.02 \text{ eV}/(2 \times 2)$  unit cell [127]. However, in that case, the distance between C planes is reduced to  $1.56 \text{ Å}$ , comparable to the in-plane C-C distance, and both the structure and electronic properties of the upper C layer would be quite different from those of graphene. This scenario can be ruled out here given the electronic band structure observed in ARPES on this same sample [94]. Nevertheless, the discrepancy regarding the measured interplane distance can be explained considering that STM probes the local density of states (LDOS) as well as the topography (see section 2.2, page 6). We therefore conclude that 2 ML-f graphene must have a much lower DOS than 1 ML graphene between the Fermi level and the energy at which the STM image was acquired.

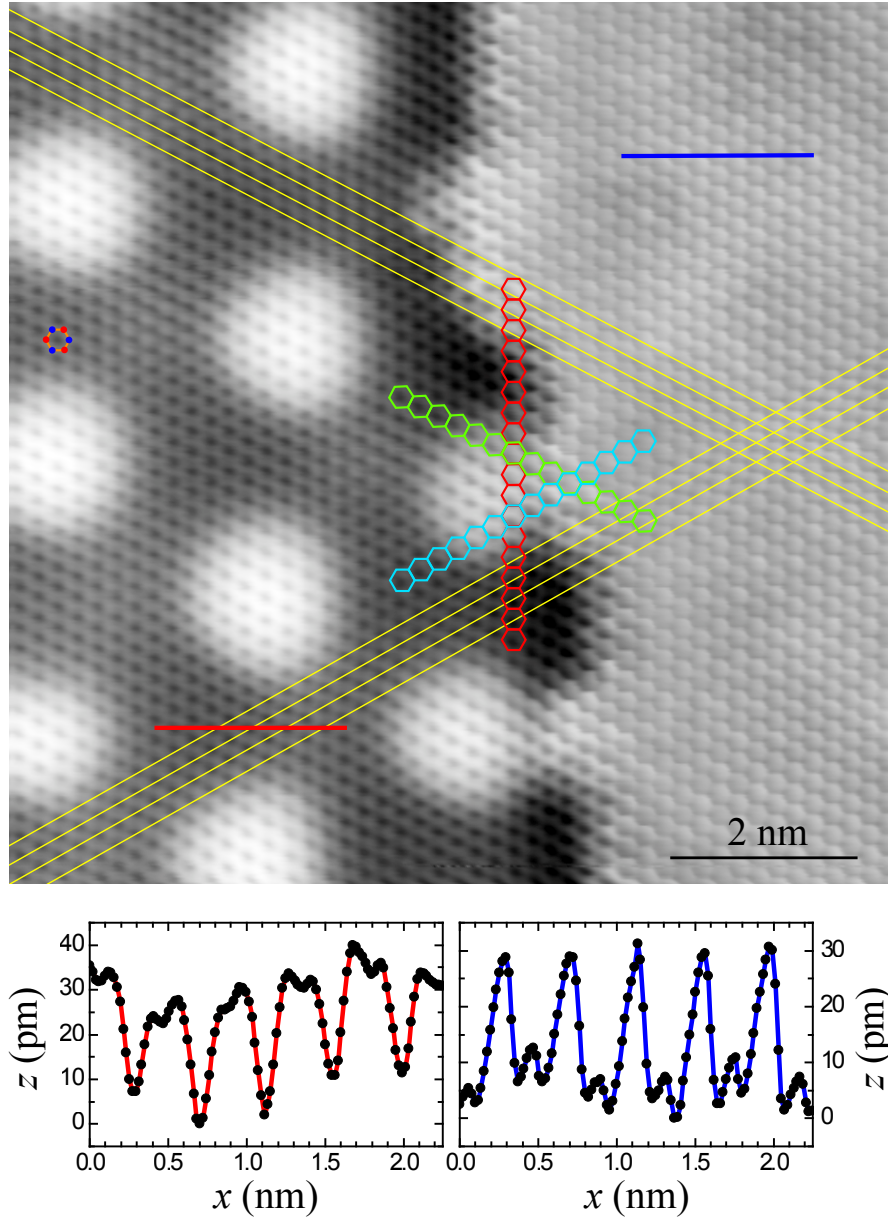


Figure 6.2: **a.** STM image acquired over a 1 ML – 2 ML-f frontier. A C<sub>6</sub> ring is evidenced on the left-hand side, with the two inequivalent C atoms, referred to as C<sub>a</sub> and C<sub>b</sub>, represented by blue and red circles. The red, cyan and green hexagons, drawn on top of C<sub>6</sub> rings over the MLG and f-BLG parts, demonstrate the continuity between their respective graphene planes in the three high-symmetry directions. The yellow lines connect the centres of the C<sub>6</sub> rings in two high-symmetry directions, evidencing continuity as well.  $V_t = -100$  mV,  $I_t = 100$  pA,  $T = 5.0$  K. **b.** STM apparent height profiles of 1 ML (red) and 2 ML-f (blue) corresponding to the coloured lines of image **a**.

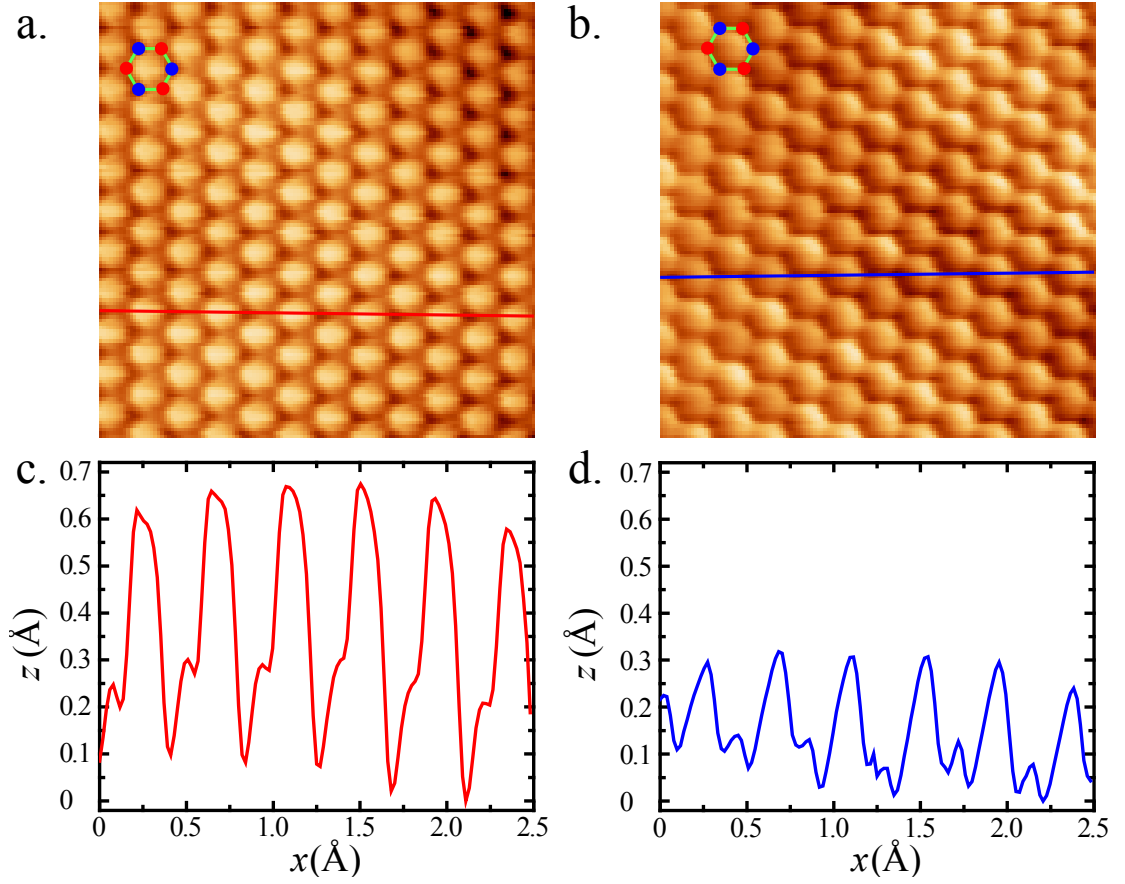


Figure 6.3: **a.** and **b.** Atomically resolved STM images of the two types of bilayer graphene on Ru(0001). **a** corresponds to 2 ML-c, and **b** to 2 ML-f. A  $C_6$  ring is sketched on the top-left corner of each image, with the two inequivalent C atoms in blue and red. Image size:  $25 \times 25 \text{ \AA}^2$ .  $V_t = -0.1 \text{ V}$ ,  $I_t = 200 \text{ pA}$  for image **a**,  $V_t = -0.1 \text{ V}$ ,  $I_t = 100 \text{ pA}$  for **b**,  $T = 4.5 \text{ K}$ . **c.** and **d.** Apparent height profile along the red and blue lines displayed in **a** and **b**. 2 ML-c displays a height difference of  $0.25 \pm 0.06 \text{ \AA}$  between each pair of nearest-neighbour C atoms (red and blue circles in the schematic), whereas this difference is  $0.04 \pm 0.07 \text{ \AA}$  for 2 ML-f.

The deduced stacking of 2 ML-f and 2 ML-c is further confirmed by comparison of their appearance at the atomic level, as can be seen in figures 6.3, **a** and **b**. From the same argument as for 2 ML-f, the protrusions of 2 ML-c must correspond to the centre of the  $C_6$  rings. As made clear by the line profiles presented in figures 6.3, **c** and **d**, for 2 ML-f, nearest-neighbour C atoms  $C_a$  and  $C_b$  appear at the same height within our error bars, their height difference being  $0.04 \pm 0.07 \text{ \AA}$ , while a height difference of  $0.25 \pm 0.06 \text{ \AA}$  is found between  $C_a$  and  $C_b$  for 2 ML-c. Thus, in 2 ML-f,  $C_a$  and  $C_b$  must occupy equivalent positions on 1 ML graphene, *i.e.*, be AA-stacked, whereas in 2 ML-c, they must see a rather different atomic environment, as it is the case for AB stacking.

## 6.2 Structure of monolayer and flat bilayer graphene on Ru(0001)

Quite a few different claims have been made regarding the structure of 1 ML G/Ru(0001). An early low energy electron diffraction (LEED) and scanning tunneling microscopy (STM) study reported an  $(11 \times 11)$  superstructure<sup>1</sup> [112], which has later been confirmed by further STM measurements [106], selected area diffraction patterns taken with low energy electron microscopy (LEEM) [114], and DFT calculations [115]. Conversely, other STM studies reported a  $(10 \times 10)$  structure [110, 113], and surface X-ray diffraction (SXRD) revealed a  $(23 \times 23)$  unit cell [107], implying an  $(11.5 \times 11.5)$  moiré cell. All these structures suppose a perfect alignment of the graphene and Ru lattices, although misalignments have already been found in some of the first STM images [106]. While these misalignments were originally associated with the presence of local structural defects, a more recent STM study has reported an intrinsic rotation angle of  $0.5^\circ$  between both atomic lattices [116]. Concerning the second monolayer, a moiré structure has not been proposed so far since it is usually considered to be unperturbed by the substrate [117]. Our STM measurements show that there is indeed a moiré pattern for 2 ML-f G/Ru(0001), and allow us to propose a model for its structure, as well as for the long debated 1 ML structure.

2 ML-c presents a rather irregular moiré pattern, making a precise study of its structure a rather difficult task. We therefore concentrated our structural analysis on 1 ML and 2 ML-f graphene, simply referred to as "2 ML" in the following.

The image presented in figure 6.2, **a** allows us to measure the relative lattice parameter of 1 ML and 2 ML with high precision, since the error coming from the STM piezo calibration will be the same for both measurements. Averaging over several line profiles along the fast scan direction (such as those sketched in figure 6.2, **b**) we obtain  $a_{1\text{ ML}} = 249.7 \pm 0.6$  pm and  $a_{2\text{ ML}} = 246.6 \pm 0.6$  pm for the respective lattice parameters, after slightly correcting the STM piezo calibration, as explained below.

2 ML exhibits a moiré pattern, similar to the 1 ML moiré, although much less pronounced: its apparent corrugation is  $0.05 \pm 0.02$  Å, that of 1 ML is  $1.30 \pm 0.05$  Å. These moiré patterns are clearly resolved in the larger scale images presented in figure 6.4, **a** and **b**, which were Fourier-transformed in order to allow for a precise determination of the atomic structure of 1 ML and 2 ML, as presented in figure 6.5, **a** and **b**. Several spots of the moiré ( $\vec{M}$ ) and graphene ( $\vec{G}$ ) reciprocal lattices are present. Measuring the  $G/M$  ratios, we obtain  $12.57 \pm 0.06$  and  $11.57 \pm 0.06$  for 1 ML and 2 ML, respectively. Angles of  $4.0 \pm 0.2^\circ$  and  $4.0 \pm 0.7^\circ$  between the moiré and graphene lattices ( $\alpha$ ) were obtained, after normalization of the angle between the first order graphene spots to  $60^\circ$ , in order to compensate for the piezo creep along the slow scan direction. The rotation between the moiré and graphene lattices in the case of 1 ML can easily be seen: the successive order spots of the moiré lattice (circled in red) and the first order spot of the atomic lattice (blue square) are not aligned, but one row of moiré spots apart, in complete agreement with a previous STM study [116]. In the case of 2 ML graphene, there

---

<sup>1</sup>The structures are given with respect to the primitive vectors of the substrate surface unit cell.



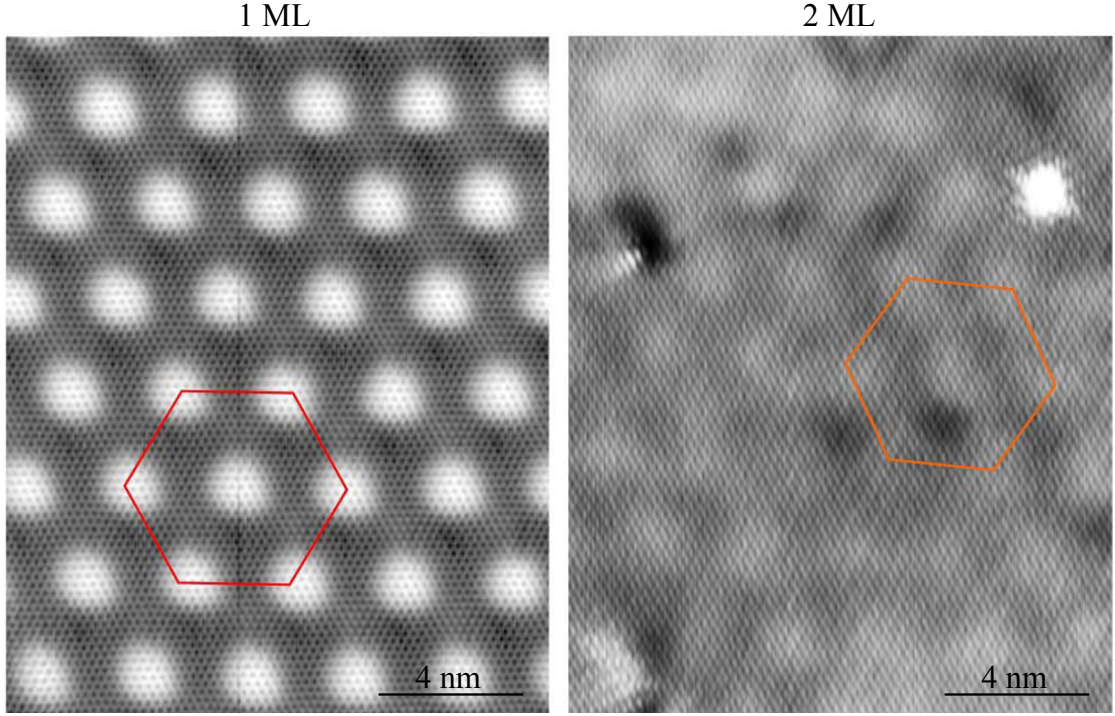


Figure 6.4: 1 ML and 2 ML moiré patterns in real space. Imaging conditions:  $V_t = -100$  mV,  $I_t = 300$  pA for 1 ML and  $V_t = -1$  V,  $I_t = 100$  pA for 2 ML,  $T = 5.0$  K. Both images present atomic resolution. The red and orange hexagons are guides to the eye for the respective moiré patterns.

are no multiple order spots from the moiré lattice, hence the larger error associated with its corresponding angle measurement.

Taking into account all these measurements, we established the two models sketched in figure 6.5, **c** and **d**, where the black dots represent the moiré reciprocal lattices. Both lattices have been expanded by a factor of 5 in the vertical direction for clarity and, again,  $\vec{G}$  and  $\vec{M}$  represent the graphene and moiré reciprocal lattice vectors. From the definition of a moiré pattern, the Ru substrate vector  $\vec{S}$  can simply be identified as the difference between the former two,  $\vec{S} = \vec{G} - \vec{M}$  [116, 128, 129]. The  $G/M$  and  $\alpha$  values resulting from these models, summarized in figure 6.5, **e** and **f**, in the row labelled *mod*, agree with the measured values within the experimental error, and the expected real space lattice parameters ( $a$ ) also agree with the measurements presented in figure 6.2 after correcting our former piezo calibration by 1.18%, a factor well within the uncertainty related to the calibration process. Therefore, the moiré cells for 1 ML and 2 ML graphene with respect to the Ru substrate lattice, given by  $S/M$  and  $\beta$ , are  $(11.57 \times 11.57) \text{ R}4.3^\circ$  and  $(10.54 \times 10.54) \text{ R}4.7^\circ$ , respectively, according to the experimental values, or  $(\sqrt{133} \times \sqrt{133}) \text{ R}4.3^\circ$  and  $(\sqrt{111} \times \sqrt{111}) \text{ R}4.3^\circ$ , respectively, according to the model. The angles between moiré and substrate  $\beta$  correspond to rotations of only  $0.3^\circ$  and  $0.7^\circ$  between graphene and substrate for 1 and 2 ML graphene, respectively, the moiré

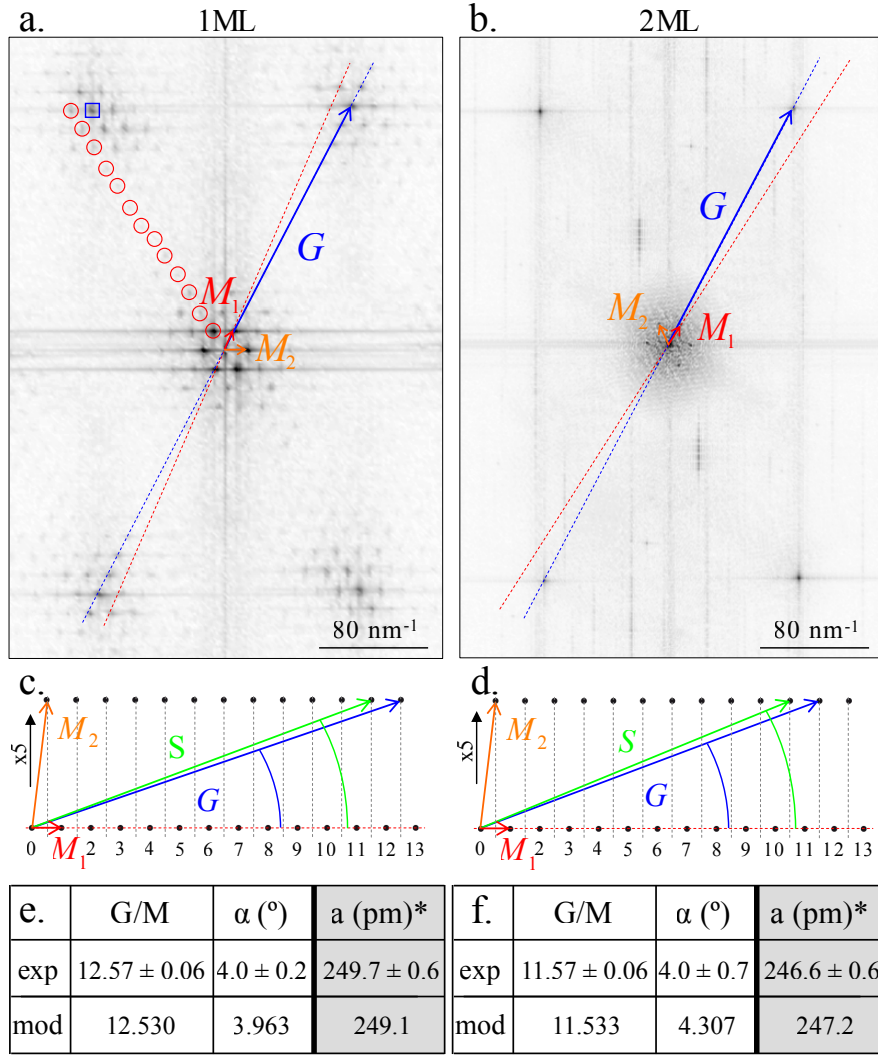


Figure 6.5: **a, b.** Fourier transforms of STM images 6.4, acquired on 1 ML and 2 ML. **c, d.** Reciprocal lattice models. The black dots represent the moiré reciprocal lattice points, such as the successive order spots visible in **a** and circled in red. Both lattices have been expanded by a factor of 5 in the vertical direction for clarity.  $\vec{M}$ ,  $\vec{G}$  and  $\vec{S}$  are the moiré, graphene and substrate reciprocal vectors, respectively. **e, f.**  $G/M$  ratios and  $\alpha$  angles measured in the Fourier transforms shown in **a** and **b** (exp), and expected from the models proposed in **c** and **d** (mod). The lattice parameters expected from the models and measured in real space from image 6.2, **a** (\* after correcting the piezo calibration as explained in the text) are also given.

pattern amplifying these rotations considerably. This is in agreement with the results of a former STM study of 1 ML graphene/Ru(0001) [116].

The  $\vec{G}$  and  $\vec{S}$  vectors have been chosen in such a way that both end on points of the respective reciprocal moiré lattices, which implies that both structures are commensurate. The commensurability period, which defines the real unit cell of the system, is however extremely large compared to the moiré cell, and close incommensurate structures would be compatible with our measurements as well. The difference between such large unit cells or incommensurate structures being irrelevant from a physical point of view anyway, the unit cells of both systems can safely be approximated by the moiré cells.

### 6.3 Apparent distortions in graphene on Ru(0001)

So far, 1 ML and 2 ML graphene have been treated as perfect hexagonal structures. However, there are some experimental evidences for important lattice distortions in the 1 ML case. Reciprocal space techniques such as LEED  $I(V)$  [130] and SXRD [131] suggest variations in the C-C bond lengths of up to 1% and 7%, respectively. An STM study also reported distortions beyond 10% in a graphene bubble formed by oxygen intercalation, where the local strain was deduced from an atomic resolution image [132]. Another STM study reported large distortions in the images and invoked the directionality and tilt of the  $\pi$ -orbitals of graphene as a qualitative explanation for their presence [118].

A surprisingly large wiggling of the atomic rows can be seen in the high resolution STM images acquired over 1 ML graphene, as one can readily see in figure 6.2, **a**, following the atomic rows in the 1 ML part. This effect could be interpreted as a mere manifestation of the local strain, and therefore exploited as a way to measure it. In order to explore this possibility, we have constructed C-C bond length maps from the  $xy$  positions of the local minima of atomic resolution STM images after filtering out the corrugation associated with the moiré and identifying the local minima as the centres of the carbon rings, as explained previously. The procedure is illustrated in figure 6.6.

Figure 6.7, **a** presents an experimental bond length map obtained from an image recorded at 1 G $\Omega$  tunneling gap resistance. The resulting C-C bonds are superimposed onto the original moiré pattern, obtained by removing the atomic details from the STM image by Fourier-filtering, and coloured according to their normalized length. The bond map shows a deformed honeycomb network subject to an inhomogeneous strain, both compressive (blue bonds) and tensile (red bonds). The spatial distribution of the strain clearly follows the periodicity of the underlying moiré pattern, with the tensile strain located prevalently on top of the moiré hills. Therefore, within the quasi-periodic  $11 \times 11$  unit cell (also traced in the same figure), the regions where the graphene is weakly bound to the substrate and forms the hills (C atoms on threefold position [129]) present the maximal expansion of the graphene lattice, while the covalently bound regions (one C atop and another in threefold position) present more variability, from slightly elongated to strongly compressed bonds.

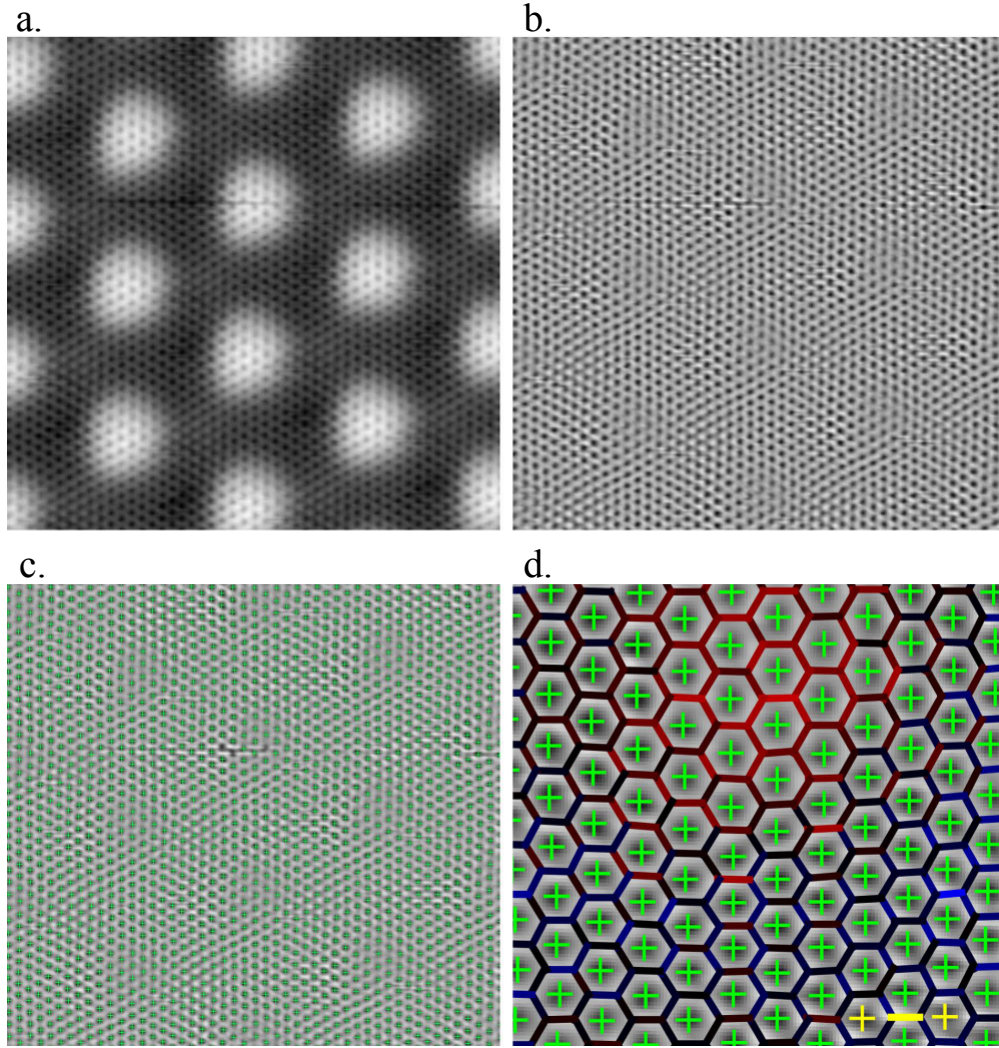


Figure 6.6: Construction of the C-C bond length map. **a.** STM image acquired at  $V_t = -100$  mV,  $I_t = 300$  pA,  $T = 5.0$  K. Image size:  $100 \times 100$  Å. **b.** Moiré corrugation removed from image **a** by means of Fourier-filtering. **c.**  $xy$  positions of the local minima in **b** obtained by Gaussian fits. **d.** Portion of the C-C bond map obtained from the  $xy$  positions in **c** as explained in the text. Image size:  $20 \times 20$  Å.



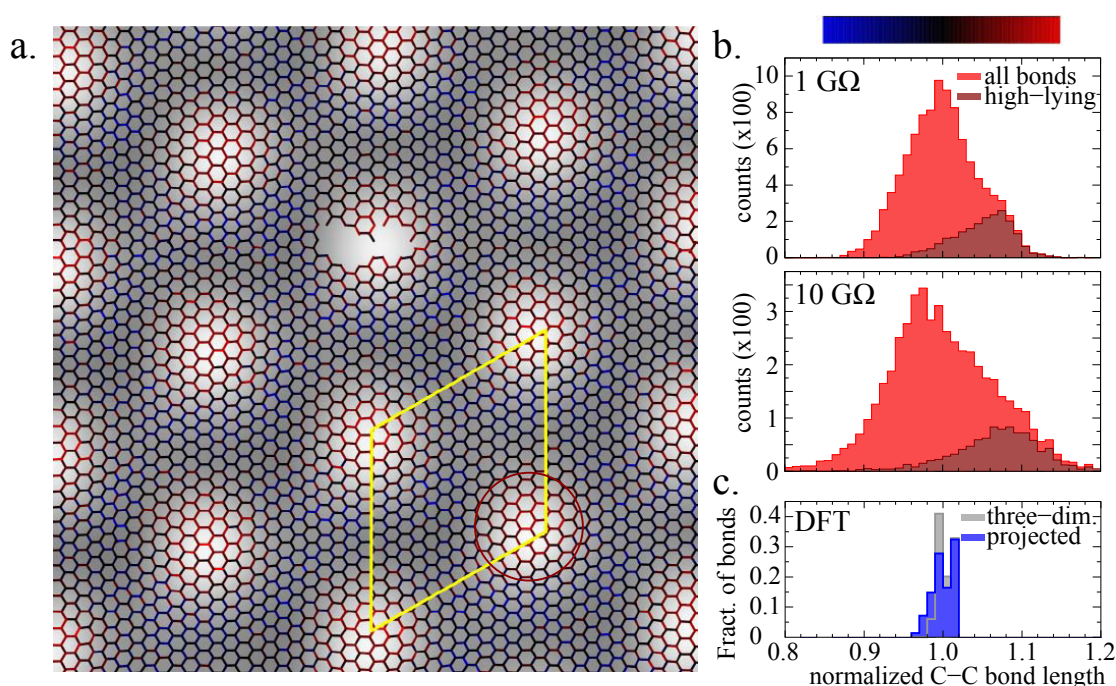


Figure 6.7: **a**. Apparent C-C bond length map obtained from the local minima of an atomic resolution STM image acquired at 1 GΩ, where the colour scale associated with the bond length is defined on top of the histograms in **b**. The moiré pseudo-unit cell is indicated in yellow. **b**. Histograms of C-C bond lengths normalized to the average measured lattice parameter obtained from STM images acquired at 1 GΩ (top) and 10 GΩ (bottom). The shaded histograms correspond to the contribution of the high-lying atoms, that is, the atoms that sit higher than half-height of the moiré hills (evidenced as a red circle in **a**). **c**. Bond length histograms from DFT simulations performed by Dr. G. Sciauzero and Prof. A. Pasquarello, normalized to the average length. Histograms for both the actual (three-dimensional) and the *xy*-projected C-C distances are shown.

To quantify the local strain in the graphene layer, the bond lengths in the map of figure 6.7, **a** were used to build the bond length histogram shown in figure 6.7, **b** (top panel): the resulting maximal local strain can exceed 10%, and a shoulder around 7% of strain is clearly visible. The C-C bonds that give rise to this shoulder are in fact those lying in the hill regions, as verified by selecting only bonds located in the highest-lying part of the moiré (indicated by a red circle in figure 6.7, **a**) to build the shaded histogram superimposed onto the original one. The observation of such a high level of strain is puzzling given the large in-plane stiffness of graphene, making highly-strained geometries energetically unfavourable. Moreover, the high level of strain in the hill regions, where the graphene-metal interaction is supposed to be weak and the strain could be easily relieved with a flatter overlayer, is even more surprising. Another bond map was constructed from an STM image acquired with a ten-times-higher tunneling gap resistance (10 G $\Omega$ , image not shown). The corresponding bond-length histogram, shown in figure 6.7, **b** (lower panel), presents an even larger maximal strain (up to  $\sim 12\%$ ) and a broader shoulder due to the high-lying graphene regions at about 9% of strain.

The fact that the observed distortions increase with tip-sample distance casts serious doubt on the realness of these distortions. We therefore looked for possible sources of apparent distortions in the STM images.

### 6.3.1 Shortening factor in the 2D-projected C-C distances

Graphene on Ru(0001) being strongly corrugated, some of its C-C bonds have a finite component along the Ru surface normal direction. STM images corresponding to a projection on the surface plane, this component is lost. This could result in an apparent shortening of some C-C distances. The maximum shortening was estimated by taking into account the approximate geometrical shape of graphene/Ru(0001) as inferred from the STM images and DFT simulations (details in the next section).<sup>2</sup>

The quasi-periodic  $12 \times 12$  graphene cell can be partitioned into almost flat regions, which occupy about 70% of the surface, and spherical hills, which are represented schematically in Fig. 6.8, **a**. The most shortened C-C bonds are those at the basal perimeter of the hill and the maximum shortening factor  $d'/d$  can be expressed as a function of the actual (three-dimensional) C-C bond length  $d$ , the radius  $a$ , and the height  $h$  of the hill (see figure 6.8, **a**):

$$d'/d = \sin \gamma, \quad \gamma = \arcsin \frac{d}{2R} + 2 \arctan \frac{a}{h} - \frac{\pi}{2}, \quad (6.1)$$

where  $d'$  is the 2D-projected bond length,  $\gamma$  is the angle indicated in figure 6.8, **a**, and the radius  $R$  depends only on  $a$  and  $h$ . In figure 6.8 **b**, the ratio  $d'/d$  is plotted as a function of  $a$  and  $h$  for a C-C bond length  $d = 0.14$  nm, close to the average C-C bond distance in supported graphene.<sup>3</sup>

<sup>2</sup>Calculations performed by Dr. G. Sclauzero and Prof. A. Pasquarello.

<sup>3</sup> $d$  is related to the lattice parameter  $a_{1\text{ ML}}$  by a factor of  $\sqrt{3}$ .

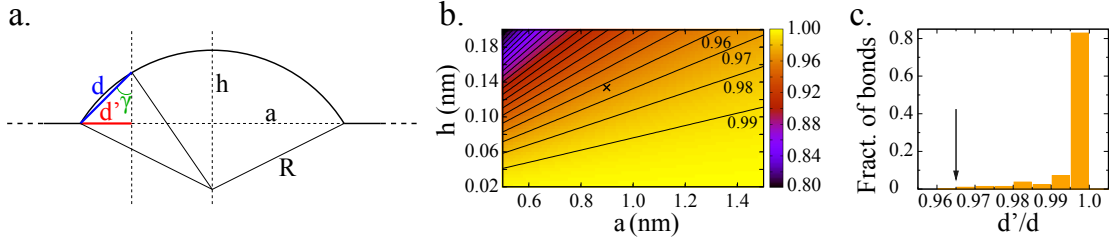


Figure 6.8: 2D-projection shortening factor. **a.** Geometric construction representing the graphene hill as a spherical cap.  $d$  and  $d'$  are the 3D and the 2D-projected C-C bond distances, respectively, for the worst-case configuration (largest shortening). **b.** Colour plot of the worst-case  $d'/d$  ratio as a function of the geometrical parameters of the hill in **a** for a representative C-C distance  $d = 0.14$  nm. The solid lines correspond to isovalues of  $d'/d$  and are spaced by 0.01. The cross indicates the parameters which best reproduce the actual size of the hill. Calculation and figure realized by Dr. G. Sclauzero. **c.** Distribution of the  $d'/d$  ratio for the C-C bonds in the DFT structure. The arrow indicates the worst-case estimate obtained in **b**, which is the lower bound of  $d'/d$ .

The height of the hill as determined from the simulations is about 0.12 nm [133, 134], while the hill radius is approximatively 0.8 nm (consistent with the experimental image in figure 6.4, **a**). With these parameters the estimated maximum shortening factor is below 4% (cross in figure 6.8, **b**). It is worth stressing that only the bonds between C atoms sitting close to the hill perimeter are shortened by 3–4%, while C-C bonds lying in the flat region and at the centre of the hill are affected by a much smaller shortening factor. The observed distortions can therefore not be accounted for by a simple projection effect.

### 6.3.2 DFT calculations of the structure

Subtle effects related to the electronic structure of the system may come into play in the STM imaging process, and the direct identification of atomic positions with local maxima in the image (or ring centres with minima, as in this specific case) may require special care. In order to investigate this possibility, Dr. G. Sclauzero and Prof. A. Pasquarello carried out a theoretical study of the graphene/Ru(0001) system within the framework of density functional theory (DFT) using the plane wave-based electronic structure code implemented in the QUANTUM-ESPRESSO package [98]. A  $12 \times 12$  graphene on  $11 \times 11$  Ru periodic cell was used here, since the main features of the graphene overlayer studied in the much larger  $25 \times 25$  on  $23 \times 23$  cell can be reproduced with this smaller one [133]. The observed rotation between graphene and Ru was thus neglected, which is justified by its small value ( $\sim 0.3^\circ$ , see section 6.2 page 70). Semi-empirical corrections to van der Waals dispersion forces [135] were included in order to better reproduce the STM features, especially on top of the hills [134]. The bond length histogram resulting from the DFT-optimized graphene/Ru(0001) structure is reported in figure 6.7, **c**. The actual (three-dimensional) C-C bond lengths from the simulations show strains below 3%, and the effect of the geometrical projection of the bonds on the Ru(0001) plane is exclusively

a bond compression, and concerns only a very small fraction of the distances, as shown in figure 6.8, **c**. This suggests that the very large strains obtained from the STM bond maps are fictitious, and in great part attributable to an electronic structure effect.

### **6.3.3 Directionality of the $\pi$ -orbitals of graphene and corrugation**

The next step towards the understanding of these apparent distortions was to consider a theoretical model of the STM imaging process of graphene based on the high directionality of the  $\pi$ -orbitals. Since a single honeycomb lattice is well resolved over most of the moiré cell and hexagonal features related to the underlying metal surface appear only in limited regions, we can assume that the largest contribution to the tunneling current under these imaging conditions comes from the graphene  $\pi$ -orbitals. In conjugated carbon systems, the approximate orthogonality of the  $\pi$ -orbitals with respect to the  $\sigma$ -bonds can be expressed in terms of the pyramidalization angle and the  $\pi$ -axial vector [136], which represents the direction of the  $\pi$ -orbital. In strongly corrugated or rippled graphene systems, one may expect substantial deviations of these pyramidalization angle and  $\pi$ -axial vector as compared to an ideal (flat) graphene layer [137], however their correlation with the STM imaging was still unexplored. Dr. G. Sclauzero and Prof. A. Pasquarello computed the  $\pi$ -axial vector of each C atom in the simulated structure [136, 137] and used it with a fixed length (comparable to the tip-sample distance in the STM experiment) to build the apparent C position that would result from the density maximum of the  $\pi$ -orbital. This procedure, shown schematically in figure 6.9, **a** results in electron density maxima that are not always directly atop the C atoms, due to the deviation of  $\pi$ -axial vector from the Ru(0001) normal in regions where the graphene layer presents high slopes.

The bond length histograms obtained from these apparent C-positions are shown in figure 6.9, **b** for two simulated tip-sample distances. In contrast to the actual DFT bond lengths (figure 6.7, **c**), the histogram presents a broadening analogous to that seen in the STM-derived ones and fictitious strains up to 10% or more, depending on the tip-sample distance. Moreover, the origin of the shoulder at large strains (which is resolved as a peak in the theoretical histograms) is the same as in the experiments, namely the subset of C-C bonds lying in the hill regions of the moiré. The shift of the shoulder toward larger lengths, as well as the general broadening of the distribution with the tip-sample increase are also qualitatively reproduced by this simple model, which, in conclusion, provides a very satisfactory explanation to the presence of large C-C bond distortions in the STM images.

### **6.3.4 Apparent distortions in 2 ML graphene**

A similar analysis applied to 2 ML graphene yielded the results presented in figure 6.10, which further confirm this interpretation: the bond lengths present a significantly lower amount of apparent distortions in comparison to 1 ML graphene, as expected from its smaller structural corrugation.



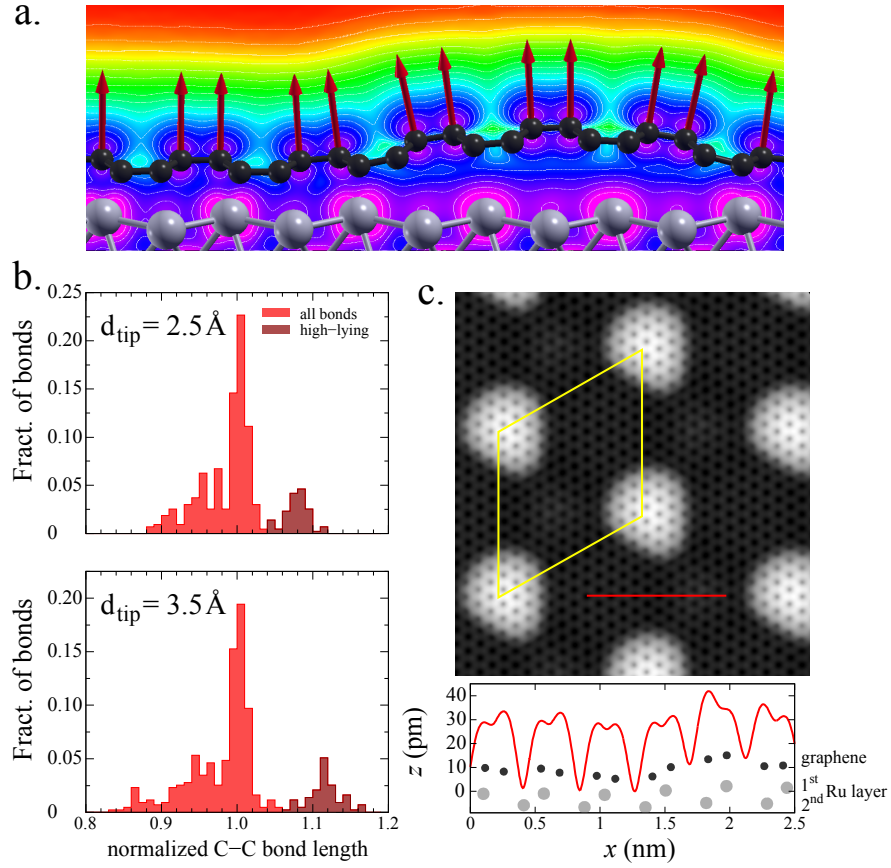


Figure 6.9: **a.** Illustration of the  $\pi$ -axial vector model used to build the histograms in **b.** A contour plot of the LDOS integrated between  $-2.5 \text{ eV}$  and the Fermi level is superimposed onto a cross section of the simulated atomic structure. The  $\pi$ -axial vectors are represented by red arrows. **b.** Histograms of bond lengths obtained from the  $\pi$ -axial vector model applied to the graphene geometry from DFT simulations. Two tip-sample distances are considered, namely  $2.5$  and  $3.5 \text{ \AA}$ , and the shaded histograms are obtained from the high-lying C-C bonds identified with the same criteria as in figure 6.7. **c.** Simulated STM image (top) and linescan (bottom) from LDOS integrated between  $-2.5 \text{ eV}$  and the Fermi level. The linescan is taken along the red line, while the level of electron density has been chosen to give the same apparent height as in the experimental linescan of figure 6.2, **b.** All the results presented in this figure were obtained by Dr. G. Sclauzero and Prof. A. Pasquarello.

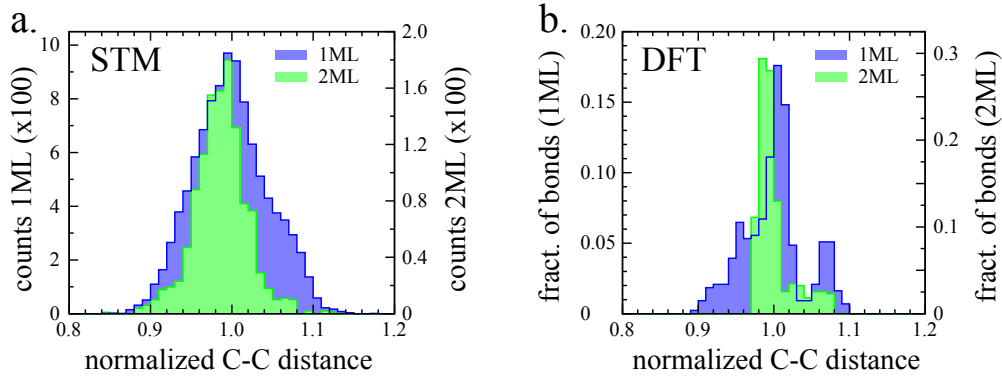


Figure 6.10: **a.** Histogram of apparent bond lengths for 1 ML (blue) and 2 ML (green), obtained from images recorded at 1 G $\Omega$  and normalized to the measured average lattice parameter of 1 ML. **b.** Similar histograms of apparent bond lengths obtained from simulations.

The differences between the experimental and theoretical distributions are mainly attributable to the smaller unit cell in the simulations, the neglected angle between the graphene and Ru lattices, some noise-related effects in the STM measurement, and the extrapolation of the C positions from those of the ring-centres. This last point was investigated, comparing theoretical bond length histograms obtained from the actual projected C positions to that obtained from the projected position of the C<sub>6</sub> ring centres. For both 1 ML graphene in figure 6.11, **a** and 2 ML graphene in figure 6.11, **b**, the two methods yield very similar results.

### 6.3.5 DFT-simulated STM images

The  $\pi$ -axial vector model provides a clear interpretation of the strain observed in the graphene network as a fictitious distortion related to the rippling of graphene on Ru and the high directionality of its  $\pi$ -orbitals. In order to corroborate this model, we compared our STM images with DFT-simulated ones. Dr. G. Sclausero and Prof. A. Pasquarello were able to reproduce reasonably well the experimental STM images of 1 ML graphene (figure 6.2, **a**) by integrating the local electronic density of states (LDOS) between the Fermi level ( $E_F$ ) down to electron binding energies of about -2.5 eV, as shown in figure 6.9, **c**, top panel. A simulated linescan shown in figure 6.9, **c**, lower panel, shows a good agreement with the experimental features in figure 6.2, **b**, such as a sharp contrast between atomic positions and ring centres, and the slight asymmetry of the two graphene sublattices in the covalently bound region. In figure 6.9, **a** the integrated LDOS is plotted on a plane normal to the Ru(0001) surface, showing that the  $\pi$ -axial vectors are aligned with the  $\pi$ -orbitals to a good approximation. The standard Tersoff-Hamann method for the simulation of STM images [10] (see section 2.2, page 6), in which the tunneling current is proportional to the LDOS integrated between  $E_F$  and the tip-sample bias voltage (about 100 meV in our case), gives a different image (not shown) that agrees with previously simulated images [133, 134] and also with some previous STM measurements [117, 86], but is in clear disagreement with the images obtained in this work.

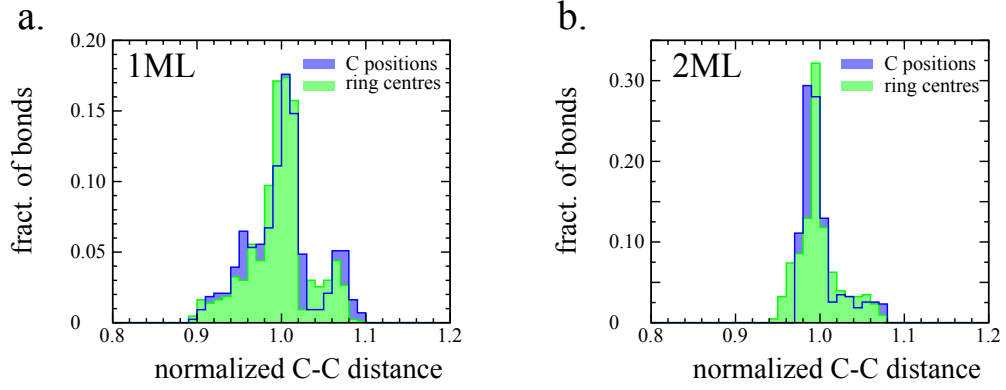


Figure 6.11: **a.** Bond length histograms built from C positions (blue) and ring centres (green), using the atomic positions obtained from the DFT-simulated 1 ML system and a 2.5 Å-long  $\pi$ -axial vector. **b.** Similar comparison for the topmost layer in the 2 ML system. In both cases, the difference between the two methods is negligible.

Indeed, simulated images at -0.1 eV [133] and 1.0 eV [134] voltage bias present a marked hexagonal pattern in the covalently bound regions of the moiré, where the interaction with the Ru surface breaks the equivalence of the two graphene sublattices. This symmetry breaking, only barely visible in our STM images, can be partially removed from the simulated images by extending the LDOS integration in order to compensate for the unbalance of  $\pi$ -electron density at  $E_F$  between the two sublattices.

Therefore, our main conclusion is that, rather than the local strain, it is the local curvature of the graphene sheet that is mapped by the method presented in figure 6.7, **a**, as suggested in a recent publication [118]. These findings also prove that the STM corrugation mainly stems from a real corrugation of graphene, and not from a pure electronic effect [138]. Moreover, this result should be taken into account in future STM studies of supported graphene systems, as well as other strongly corrugated surfaces with highly directional orbitals.



## 7 Conclusion and outlook

In conclusion, the choice of Co/Pt(111) was motivated by the initial objective of demonstrating magnetic remanence in single adatoms. We have realized an in-depth characterization of Co and Co-hydrides adsorbed on Pt(111), presented in chapter 4. CoH, CoH<sub>2</sub> and CoH<sub>3</sub> have been clearly identified. Their general appearance in STM, vibrational modes, and magnetic properties have been reported, as well as a method to deprotonate them individually. Most interestingly, a Kondo effect was discovered for CoH<sub>2</sub>/Pt(111), with Kondo temperature  $T_K = 8 \pm 4$  K, demonstrating how H<sub>2</sub> adsorption can drastically alter the orbital environment of an adatom, and thus its magnetic properties. This is the very first report of the appearance of a Kondo effect in a non-Kondo system through H-adsorption.

A methodology to observe magnetic remanence in Co adatoms was established. Several attempts have been performed, and no magnetic contrast could be evidenced. We can however not conclude on the absence of remanence in this system since no magnetic contrast was observed on Co islands either in the same measurement conditions. Consequently, magnetic remanence in single adatoms is still an open question. A report that appeared at the very end of this thesis work holds the current record for the smallest stable magnet, five adatom-large Fe clusters on Cu(111) [28].

SP-STM has proven itself as a technique of choice to tackle this very exciting problem, and different approaches, possibly more efficient, have been suggested in the conclusion of the chapter. However, this technique still presents several experimental challenges, such as achieving a high-level of spin-contrast at extremely low bias, or producing a spin-polarized tip that presents a negligible stray-field close to the adatoms. Other emerging techniques are positioning themselves as very interesting alternatives. The nano-Superconducting QUantum Interference Device (nano-SQUID) magnetometer [139], for example, constitutes a serious concurrent to SP-STM in the field of atomic and molecular magnetism. Ultralow-temperature XMCD may also provide an answer to our initial question [140]. The main difficulty in this case comes from the fact that it is a spatially-averaging technique. A very homogeneous ensemble

of adatoms is required (negligible amount of contaminated adatoms, adatoms on defects, dimers or clusters), as well as a high sensitivity and excellent vacuum conditions.

The rest of this thesis work involved graphene which, once again, justified itself as an extremely surprising and promising material for a wide range of applications. What drew our interest to this material were the numerous predictions of unprecedented high magnetic anisotropy energies for transition metal adatoms on graphene. Although many theoretical studies existed on this matter, no experimental measurement had been reported so far. In chapter 5, we have presented the very first measurement of the magnetic moment and anisotropy of single adatoms on graphene. Our results are fully supported by *ab initio* calculations. A magnetic moment of  $2.2 \pm 0.4 \mu_B$  was obtained for Co/G/Pt(111), and a giant anisotropy energy of  $8.1 \pm 0.4$  meV was found, comparable to the absolute record value held by Co/Pt(111). Interestingly, this very high anisotropy value mainly originates from the crystal field generated by the graphene, and not from the interaction with a substrate having a high spin-orbit coupling, such as Pt and other such high anisotropy substrates. Co/G/Pt(111) was found to have an easy magnetization plane/hard magnetization axis, and can therefore not exhibit magnetic remanence.

Co-hydrides were also found for this system, and their respective properties have been thoroughly investigated. While two of them only present vibrational excitations, CoH<sub>3</sub> was found to yield similar magnetic properties as compared to clean Co. A comparable magnetic moment and magnetic axes orientation were observed, with an anisotropy energy smaller by a factor of  $\sim 5$ . Furthermore, controlled deprotonation, *i.e.*, switching of any CoH<sub>*x*</sub> (*x* = 1, 2, 3) complex into CoH<sub>*x*-1</sub>, was demonstrated. The presence of H was shown to alter dramatically the magnetic properties of Co/G/Pt(111), and should imperatively be checked for in any future study of the magnetic properties of metallic adatoms on graphene.

Graphene will undoubtedly remain a substrate of choice for magnetic adsorbates, and we expect to hear of many further theoretical and experimental studies in a near future. And it would not be too surprising to encounter one day a technologically-relevant device based on the peculiar magnetic anisotropy of nanostructures on graphene, for magnetic data storage, spintronic applications, or else.

---

Although purely concerned with structural aspects, our study of mono- and bilayer graphene on Ru(0001), presented in chapter 6, may prove itself decisive in the choice of a substrate for graphene-based magnetic nanostructures. G/Ru(0001) is a promising system due to its homogeneity, its unique moiré pattern, and the possibility to grow a well-decoupled second layer of graphene. In addition to a clear determination of the long-debated unit cell of monolayer graphene, two differently stacked bilayers were identified in STM, what allowed for a solid interpretation of ARPES data obtained on the very same sample [94]. This photoemission study reported electronic properties very close to those of free-standing graphene for the newly-discovered AA-stacked bilayer graphene, which is therefore a very promising substrate for fundamental studies and potential applications related to graphene.

Strain is a major issue in graphene, impacting its electronic properties dramatically, and strain-engineering has even been proposed as a realistic way to tailor them [103]. We therefore performed a detailed study of the very large distortions (beyond 10%) of the C-C bonds observed in the STM images of monolayer graphene. Although such apparent distortions had already been reported and qualitatively accounted for [118], we have provided the first systematic and quantitative analysis based on the comparison of STM images and simulations from van der Waals-corrected DFT and  $\pi$ -axial model. The presented model provides an excellent agreement with our STM images for real distortions of the C-C bonds below 3%. These findings should be taken into account in any future STM-based structure study of corrugated graphene.





# Bibliography

- [1] G. Binnig and H. Rohrer. Scanning tunneling microscopy. *Surface Science*, 126(1-3):236–244, 1983.
- [2] G. Binnig and H. Rohrer. Scanning tunneling microscopy from birth to adolescence. *Reviews of Modern Physics*, 59(3):615–625, 1987.
- [3] F. C. Tabak, E. C. M. Disseldorp, G. H. Wortel, A. J. Katan, M. B. S. Hesselberth, T. H. Oosterkamp, J. W. M. Frenken, and W. M. van Spengen. MEMS-based fast scanning probe microscopes. *Ultramicroscopy*, 110(6):599–604, 2010.
- [4] D. M. Eigler and E. K. Schweizer. Positioning single atoms with a scanning tunnelling microscope. *Nature*, 344(6266):524–526, 1990.
- [5] J. A. Stroscio and D. M. Eigler. Atomic and molecular manipulation with the scanning tunneling microscope. *Science*, 254(5036):1319–1326, 1991.
- [6] M. F. Crommie, C. P. Lutz, and D. M. Eigler. Confinement of electrons to quantum corrals on a metal surface. *Science*, 262(5131):218–220, 1993.
- [7] H. J. Lee and W. Ho. Single-bond formation and characterization with a scanning tunneling microscope. *Science*, 286(5445):1719–1722, 1999.
- [8] J. Bardeen. Tunnelling from a many-particle point of view. *Physical Review Letters*, 6(2):57–59, 1961.
- [9] C. J. Chen. *Introduction to scanning tunneling microscopy*. Oxford series on optical and imaging sciences. Oxford University Press, 1993.
- [10] J. Tersoff and D. R. Hamann. Theory and application for the scanning tunneling microscope. *Physical Review Letters*, 50(25):1998–2001, 1983.
- [11] J. Tersoff and D. R. Hamann. Theory of the scanning tunneling microscope. *Physical Review B*, 31(2):805–813, 1985.
- [12] R. Wiesendanger, H.-J. Güntherodt, G. Güntherodt, R. J. Gambino, and R. Ruf. Observation of vacuum tunneling of spin-polarized electrons with the scanning tunneling microscope. *Physical Review Letters*, 65(2):247–250, 1990.

## Bibliography

---

- [13] M. Bode. Spin-polarized scanning tunnelling microscopy. *Reports on Progress in Physics*, 66(4):523–582, 2003.
- [14] R. Wiesendanger. Spin mapping at the nanoscale and atomic scale. *Reviews of Modern Physics*, 81(4):1495–1550, 2009.
- [15] M. Julliere. Tunneling between ferromagnetic films. *Physics Letters A*, 54(3):225–226, 1975.
- [16] D. Wortmann, S. Heinze, P. Kurz, G. Bihlmayer, and S. Blügel. Resolving complex atomic-scale spin structures by spin-polarized scanning tunneling microscopy. *Physical Review Letters*, 86(18):4132–4135, 2001.
- [17] R. C. Jaklevic and J. Lambe. Molecular vibration spectra by electron tunneling. *Physical Review Letters*, 17(22):1139–1140, 1966.
- [18] B. C. Stipe, M. A. Rezaei, and W. Ho. Single-molecule vibrational spectroscopy and microscopy. *Science*, 280(5370):1732–1735, 1998.
- [19] L. Claude. *Construction d'un microscope à effet tunnel à basse température et études d'impuretés magnétiques en surfaces*. PhD thesis, EPFL, 2005.
- [20] S. R. Koebley, R. A. Outlaw, and R. R. Dellwo. Degassing a vacuum system with in-situ UV radiation. *Journal of Vacuum Science and Technology A*, 30(6):060601, 2012.
- [21] R. M. White. *Quantum theory of magnetism: magnetic properties of materials*. Springer series in solid-state sciences. Springer, 2007.
- [22] J. Stöhr and H. C. Siegmann. *Magnetism - From Fundamentals to Nanoscale Dynamics*. Springer, Berlin, 2006.
- [23] W. Wernsdorfer. Classical and quantum magnetization reversal studied in nanometer-sized particles and clusters. *Advances In Chemical Physics*, Vol 118, 118:99–190, 2001.
- [24] A. Abragam and B. Bleaney. *Electron paramagnetic resonance of transition ions*. Clarendon Press, Oxford, 1970.
- [25] H. A. Kramers. General theory of the paramagnetic rotation in crystals. *Proceedings of the Koninklijke Akademie Van Wetenschappen Te Amsterdam*, 33(6/10):959–972, 1930.
- [26] B. Barbara, W. Wernsdorfer, L. C. Sampaio, J. G. Park, C. Paulsen, M. A. Novak, R. Ferré, D. Mailly, R. Sessoli, A. Caneschi, K. Hasselbach, A. Benoit, and L. Thomas. Mesoscopic quantum tunneling of the magnetization. *Journal of Magnetism and Magnetic Materials*, 140–144:1825–1828, 1995.
- [27] W. Wernsdorfer and R. Sessoli. Quantum phase interference and parity effects in magnetic molecular clusters. *Science*, 284(5411):133–135, 1999.

- 
- [28] A. A. Khajetoorians, B. Baxevanis, C. Hübner, T. Schlenk, S. Krause, T. O. Wehling, S. Lounis, A. Lichtenstein, D. Pfannkuche, J. Wiebe, and R. Wiesendanger. Current-driven spin dynamics of artificially constructed quantum magnets. *Science*, 339(6115):55–59, 2013.
- [29] A. J. Heinrich, J. A. Gupta, C. P. Lutz, and D. M. Eigler. Single-atom spin-flip spectroscopy. *Science*, 306:466, 2004.
- [30] L. Y. L. Shen and J. M. Rowell. Zero-bias tunneling anomalies – temperature, voltage, and magnetic field dependence. *Physical Review*, 165(2):566–577, 1968.
- [31] R. H. Wallis and A. F. G. Wyatt. Exchange scattering in Ti-doped Al/Al oxide/Ag tunnel junctions. II. magnetic field. *Journal of Physics C: Solid State Physics*, 7(7):1293, 1974.
- [32] S. Bermon, D. E. Paraskevopoulos, and P. M. Tedrow. Ultra-high magnetic field study of the Kondo-type zero-bias conductance peak in magnetically doped metal-insulator-metal tunnel junctions. *Physical Review B*, 17(5):2110–2123, 1978.
- [33] C. F. Hirjibehedin, C. P. Lutz, and A. J. Heinrich. Spin coupling in engineered atomic structures. *Science*, 312(5776):1021–1024, 2006.
- [34] C. F. Hirjibehedin, C. Y. Lin, A. F. Otte, M. Ternes, C. P. Lutz, B. A. Jones, and A. J. Heinrich. Large magnetic anisotropy of a single atomic spin embedded in a surface molecular network. *Science*, 317:1199, 2007.
- [35] A. F. Otte, M. Ternes, K. Von Bergmann, S. Loth, H. Brune, C. P. Lutz, C. F. Hirjibehedin, and A. J. Heinrich. The role of magnetic anisotropy in the Kondo effect. *Nature Physics*, 4(11):847–850, 2008.
- [36] A. F. Otte, M. Ternes, S. Loth, C. P. Lutz, C. F. Hirjibehedin, and A. J. Heinrich. Spin excitations of a Kondo-screened atom coupled to a second magnetic atom. *Physical Review Letters*, 103(10):107203, 2009.
- [37] S. Loth, K. Von Bergmann, M. Ternes, A. F. Otte, C. P. Lutz, and A. J. Heinrich. Controlling the state of quantum spins with electric currents. *Nature Physics*, 6(5):340–344, 2010.
- [38] S. Loth, C. P. Lutz, and A. J. Heinrich. Spin-polarized spin excitation spectroscopy. *New Journal of Physics*, 12(12):125021, 2010.
- [39] S. Loth, M. Etzkorn, C. P. Lutz, D. M. Eigler, and A. J. Heinrich. Measurement of fast electron spin relaxation times with atomic resolution. *Science*, 329(5999):1628–1630, 2010.
- [40] A. A. Khajetoorians, B. Chilian, J. Wiebe, S. Schuwalow, F. Lechermann, and R. Wiesendanger. Detecting excitation and magnetization of individual dopants in a semiconductor. *Nature*, 467(7319):1084–1087, 2010.

## Bibliography

---

- [41] A. A. Khajetoorians, S. Lounis, B. Chilian, A. T. Costa, L. Zhou, D. L. Mills, J. Wiebe, and R. Wiesendanger. Itinerant nature of atom-magnetization excitation by tunneling electrons. *Physical Review Letters*, 106(3):037205, 2011.
- [42] T. Balashov, T. Schuh, A. F. Takács, A. Ernst, S. Ostanin, J. Henk, I. Mertig, P. Bruno, T. Miyamachi, S. Suga, and W. Wulfhekel. Magnetic anisotropy and magnetization dynamics of individual atoms and clusters of Fe and Co on Pt(111). *Physical Review Letters*, 102(25):257203, 2009.
- [43] J. Kondo. Resistance minimum in dilute magnetic alloys. *Progress of Theoretical Physics*, 32(1):37–49, 1964.
- [44] P. W. Anderson. Localized magnetic states in metals. *Physical Review*, 124(1):41–53, 1961.
- [45] P. W. Anderson. A poor man's derivation of scaling laws for the Kondo problem. *Journal of Physics C: Solid State Physics*, 3(12):2436–2441, 1970.
- [46] G. Gruner and A. Zawadowski. Magnetic impurities in non-magnetic metals. *Reports on Progress in Physics*, 37(12):1497, 1974.
- [47] A. C. Hewson. *The Kondo Problem to Heavy Fermions*. Cambridge Studies in Magnetism. Cambridge University Press, 1997.
- [48] V. Madhavan, W. Chen, T. Jamneala, M. F. Crommie, and N. S. Wingreen. Tunneling into a single magnetic atom: Spectroscopic evidence of the Kondo resonance. *Science*, 280(5363):567–569, 1998.
- [49] F. Patthey, J.-M. Imer, W.-D. Schneider, H. Beck, Y. Baer, and B. Delley. High-resolution photoemission study of the low-energy excitations in 4f-electron systems. *Physical Review B*, 42(14):8864–8881, 1990.
- [50] D. Malterre, M. Grioni, and Y. Baer. Recent developments in high-energy spectroscopies of Kondo systems. *Advances in Physics*, 45(4):299–348, 1996.
- [51] U. Fano. Effects of configuration interaction on intensities and phase shifts. *Physical Review*, 124(6):1866–1878, 1961.
- [52] K. Nagaoka, T. Jamneala, M. Grobis, and M. F. Crommie. Temperature dependence of a single Kondo impurity. *Physical Review Letters*, 88(7):077205, 2002.
- [53] J. Lambe and R. C. Jaklevic. Molecular vibration spectra by inelastic electron tunneling. *Physical Review*, 165(3):821–832, 1968.
- [54] D. Goldhaber-Gordon, H. Shtrikmant, D. Mahalu, D. Abusch-Magder, U. Meirav, and M. A. Kastner. Kondo effect in a single-electron transistor. *Nature*, 391(6663):156–159, 1998.

- 
- [55] S. Sasaki, S. De Franceschi, J. M. Elzerman, W. G. Van Der Wiel, M. Eto, S. Tarucha, and L. P. Kouwenhoven. Kondo effect in an integer-spin quantum dot. *Nature*, 405(6788):764–767, 2000.
- [56] R. Žitko, R. Peters, and T. Pruschke. Splitting of the Kondo resonance in anisotropic magnetic impurities on surfaces. *New Journal of Physics*, 11:053003, 2009.
- [57] P. Gambardella, S. Rusponi, M. Veronese, S. S. Dhesi, C. Grazioli, A. Dallmeyer, I. Cabria, R. Zeller, P. H. Dederichs, K. Kern, C. Carbone, and H. Brune. Giant magnetic anisotropy of single cobalt atoms and nanoparticles. *Science*, 300(5622):1130–1133, 2003.
- [58] Y. Yayan, Xinghua Lu, and M. F. Crommie. Bimodal electronic structure of isolated Co atoms on Pt(111). *Physical Review B*, 73(15):155401, 2006.
- [59] F. Meier, L. Zhou, J. Wiebe, and R. Wiesendanger. Revealing magnetic interactions from single-atom magnetization curves. *Science*, 320(5872):82–86, 2008.
- [60] F. Meier. *Co on Pt(111) studied by spin-polarized scanning tunneling microscopy and spectroscopy*. PhD thesis, Universität Hamburg, 2006.
- [61] W. Ho. Single-molecule chemistry. *Journal of Chemical Physics*, 117(24):11033–11061, 2002.
- [62] J. M. Hollas. *Basic Atomic and Molecular Spectroscopy*. Tutorial Chemistry Texts. The Royal Society of Chemistry, 2002.
- [63] M. Reichenbacher and J. Popp. *Challenges in Molecular Structure Determination*. Springer, 2012.
- [64] T. Elsaesser. Coherent dynamics of hydrogen bonds in liquids studied by femtosecond vibrational spectroscopy. In *Practical Spectroscopy*, pages 49–91. CRC Press, 2007.
- [65] M. Pivetta, M. Ternes, F. Patthey, and W.-D. Schneider. Diatomic molecular switches to enable the observation of very-low-energy vibrations. *Physical Review Letters*, 99(12):126104, 2007.
- [66] P. E. M. Siegbahn, M. R. A. Blomberg, and C. W. Bauschlicher Jr. Potential energy surfaces of MH<sub>2</sub> (M=Co, Fe, and Cu). *The Journal of Chemical Physics*, 81:1373–1382, 1984.
- [67] M. Ternes, A. J. Heinrich, and W.-D. Schneider. Spectroscopic manifestations of the Kondo effect on single adatoms. *Journal of Physics: Condensed Matter*, 21:053001, 2009.
- [68] I. Fernández-Torrente, K. J. Franke, and J. I. Pascual. Vibrational Kondo effect in pure organic charge-transfer assemblies. *Physical Review Letters*, 101(21):217203, 2008.
- [69] S. Rusponi, N. Weiss, T. Cren, M. Epplé, and H. Brune. High tunnel magnetoresistance in spin-polarized scanning tunneling microscopy of Co nanoparticles on Pt(111). *Applied Physics Letters*, 87(16):1–3, 2005.

- [70] F. Meier, K. Von Bergmann, P. Ferriani, J. Wiebe, M. Bode, K. Hashimoto, S. Heinze, and R. Wiesendanger. Spin-dependent electronic and magnetic properties of Co nanostructures on Pt(111) studied by spin-resolved scanning tunneling spectroscopy. *Physical Review B*, 74(19):195411, 2006.
- [71] S. Rusponi, T. Cren, N. Weiss, M. Epple, P. Bulushek, L. Claude, and H. Brune. The remarkable difference between surface and step atoms in the magnetic anisotropy of two-dimensional nanostructures. *Nature Materials*, 2(8):546–551, 2003.
- [72] M. A. Ruderman and C. Kittel. Indirect exchange coupling of nuclear magnetic moments by conduction electrons. *Physical Review*, 96(1):99–102, 1954.
- [73] T. Kasuya. A theory of metallic ferro- and antiferromagnetism on Zener’s model. *Progress of Theoretical Physics*, 16(1):45–57, 1956.
- [74] K. Yosida. Magnetic properties of Cu-Mn alloys. *Physical Review*, 106(5):893–898, 1957.
- [75] R. J. Xiao, D. Fritsch, M. D. Kuz’mín, K. Koepernik, H. Eschrig, M. Richter, K. Vietze, and G. Seifert. Co dimers on hexagonal carbon rings proposed as subnanometer magnetic storage bits. *Physical Review Letters*, 103:187201, 2009.
- [76] R. J. Xiao, D. Fritsch, M. D. Kuz’mín, K. Koepernik, M. Richter, K. Vietze, and G. Seifert. Prediction of huge magnetic anisotropies of transition-metal dimer-benzene complexes from density functional theory calculations. *Physical Review B*, 82:205125, 2010.
- [77] T. O. Wehling, A. V. Balatsky, M. I. Katsnelson, A. I. Lichtenstein, and A. Rosch. Orbitally controlled Kondo effect of Co adatoms on graphene. *Physical Review B*, 81:115427, 2010.
- [78] K. Pi, K. M. McCreary, W. Bao, W. Han, Y. F. Chiang, Y. Li, S. W. Tsai, C. N. Lau, and R. K. Kawakami. Electronic doping and scattering by transition metals on graphene. *Physical Review B*, 80:075406, 2009.
- [79] A. V. Krashenninnikov, P. O. Lehtinen, A. S. Foster, P. Pyykkö, and R. M. Nieminen. Embedding transition-metal atoms in graphene: Structure, bonding, and magnetism. *Physical Review Letters*, 102:126807, 2009.
- [80] V. W. Brar, R. Decker, H.-M. Solowan, Y. Wang, L. Maserati, K. T. Chan, H. Lee, C. O. Girit, A. Zettl, S. G. Louie, M. L. Cohen, and M. F. Crommie. Gate-controlled ionization and screening of cobalt adatoms on a graphene surface. *Nature Physics*, 7(1):43–47, 2011.
- [81] Y. Wang, V. W. Brar, A. V. Shytov, Q. Wu, W. Regan, H. Z. Tsai, A. Zettl, L. S. Levitov, and M. F. Crommie. Mapping Dirac quasiparticles near a single Coulomb impurity on graphene. *Nature Physics*, 8:653, 2012.
- [82] H. Sevinçli, M. Topsakal, E. Durgun, and S. Ciraci. Electronic and magnetic properties of 3d transition-metal atom adsorbed graphene and graphene nanoribbons. *Physical Review B*, 77(19):195434, 2008.

- [83] B. Uchoa, T. G. Rappoport, and A. H. Castro Neto. Kondo quantum criticality of magnetic adatoms in graphene. *Physical Review Letters*, 106(1):016801, 2011.
- [84] K. Sengupta and G. Baskaran. Tuning Kondo physics in graphene with gate voltage. *Physical Review B*, 77(4):045417, 2008.
- [85] K. M. McCreary, A. G. Swartz, W. Han, J. Fabian, and R. K. Kawakami. Magnetic moment formation in graphene detected by scattering of pure spin currents. *Physical Review Letters*, 109(18):186604, 2012.
- [86] M. Gyamfi, T. Eelbo, M. Waśniowska, and R. Wiesendanger. Inhomogeneous electronic properties of monolayer graphene on Ru(0001). *Physical Review B*, 83:153418, 2011.
- [87] M. Gyamfi, T. Eelbo, M. Waśniowska, T. O. Wehling, S. Forti, U. Starke, A. I. Lichtenstein, M. I. Katsnelson, and R. Wiesendanger. Orbital selective coupling between Ni adatoms and graphene Dirac electrons. *Physical Review B*, 85:161406, 2012.
- [88] O. V. Yazyev and A. Pasquarello. Metal adatoms on graphene and hexagonal boron nitride: Towards rational design of self-assembly templates. *Physical Review B*, 82:045407, 2010.
- [89] A. N. Rudenko, F. J. Keil, M. I. Katsnelson, and A. I. Lichtenstein. Adsorption of cobalt on graphene: Electron correlation effects from a quantum chemical perspective. *Physical Review B*, 86:075422, 2012.
- [90] J. Wintterlin and M. L. Bocquet. Graphene on metal surfaces. *Surface Science*, 603:1841, 2009.
- [91] T. A. Land, T. Michely, R. J. Behm, J. C. Hemminger, and G. Comsa. Direct observation of surface reactions by scanning tunneling microscopy: Ethylene - ethynidyne - carbon particles - graphite on Pt(111). *Journal of Chemical Physics*, 97:6774, 1992.
- [92] M. Gao, Y. Pan, L. Huang, H. Hu, L. Z. Zhang, H. M. Guo, S. X. Du, and H. J. Gao. Epitaxial growth and structural property of graphene on Pt(111). *Applied Physics Letters*, 98:033101, 2011.
- [93] P. Merino, M. Švec, A. L. Pinardi, G. Otero, and J. A. Martín-Gago. Strain-driven moiré superstructures of epitaxial graphene on transition metal surfaces. *ACS Nano*, 5(7):5627, 2011.
- [94] M. Papagno, D. Pacilé, D. Topwal, P. Moras, P. M. Sheverdyeva, F. D. Natterer, A. Lehnert, S. Rusponi, Q. Dubout, F. Calleja, E. Frantzeskakis, S. Pons, J. Fujii, I. Vobornik, M. Grioni, C. Carbone, and H. Brune. Two distinct phases of bilayer graphene films on Ru(0001). *ACS Nano*, 6:9299, 2012.
- [95] Z.-P. Hu, D. F. Ogletree, M. A. Van Hove, and G. A. Somorjai. Leed theory for incommensurate overlayers: Application to graphite on Pt(111). *Surface Science*, 180:433–459, 1987.

## Bibliography

---

- [96] V. I. Anisimov, J. Zaanen, and O. K. Andersen. Band theory and Mott insulators: Hubbard U instead of Stoner I. *Physical Review B*, 44:943, 1991.
- [97] M. Cococcioni and S. de Gironcoli. Linear response approach to the calculation of the effective interaction parameters in the LDA+U method. *Physical Review B*, 71:035105, 2005.
- [98] P. Giannozzi, Stefano Baroni, Nicola Bonini, Matteo Calandra, Roberto Car, Carlo Cavazzoni, Davide Ceresoli, Guido L Chiarotti, Matteo Cococcioni, Ismaila Dabo, Andrea Dal Corso, Stefano de Gironcoli, Stefano Fabris, Guido Fratesi, Ralph Gebauer, Uwe Gerstmann, Christos Gougoussis, Anton Kokalj, Michele Lazzeri, Layla Martin-Samos, Nicola Marzari, Francesco Mauri, Riccardo Mazzarello, Stefano Paolini, Alfredo Pasquarello, Lorenzo Paulatto, Carlo Sbraccia, Sandro Scandolo, Gabriele Sclauzero, Ari P Seitsonen, Alexander Smogunov, Paolo Umari, and Renata M Wentzcovitch. QUANTUM ESPRESSO: a modular and open-source software project for quantum simulations of materials. *Journal of Physics: Condensed Matter*, 21:395502, 2009.
- [99] A. Dal Corso and A. Mosca Conte. Spin-orbit coupling with ultrasoft pseudopotentials: Application to Au and Pt. *Physical Review B*, 71:115106, 2005.
- [100] P. Sutter, J. T. Sadowski, and E. Sutter. Graphene on Pt(111): Growth and substrate interaction. *Physical Review B*, 80(24):245411, 2009.
- [101] S. K. Misra, C. P. Poole, and H. A. Farach. A review of spin hamiltonian forms for various point-group site symmetries. *Applied Magnetic Resonance*, 11:29, 1996.
- [102] G. Giovannetti, P. A. Khomyakov, G. Brocks, V. M. Karpan, J. van den Brink, and P. J. Kelly. Doping graphene with metal contacts. *Physical Review Letters*, 101:026803, 2008.
- [103] F. Guinea, M. I. Katsnelson, and A. K. Geim. Energy gaps and zero-field quantum Hall effect in graphene by strain engineering. *Nature Physics*, 6:30–33, 2010.
- [104] V. M. Karpan, P. A. Khomyakov, A. A. Starikov, G. Giovannetti, M. Zwierzycki, M. Talanana, G. Brocks, J. van den Brink, and P. J. Kelly. Theoretical prediction of perfect spin filtering at interfaces between close-packed surfaces of Ni or Co and graphite or graphene. *Physical Review B*, 78:195419, 2008.
- [105] H. B. Heersche, P. Jarillo-Herrero, J. B. Oostinga, L. M. K. Vandersypen, and A. F. Morpurgo. Bipolar supercurrent in graphene. *Nature*, 446(7131):56–59, 2007.
- [106] S. Marchini, S. Günther, and J. Wintterlin. Scanning tunneling microscopy of graphene on Ru(0001). *Physical Review B*, 76:075429, 2007.
- [107] D. Martocchia, P. R. Willmott, T. Brugger, M. Björck, S. Günther, C. M. Schlepütz, A. Cervellino, S. A. Pauli, B. D. Patterson, S. Marchini, J. Wintterlin, W. Moritz, and T. Greber. Graphene on Ru(0001): A  $25 \times 25$  supercell. *Physical Review Letters*, 101:126102, 2008.



- 
- [108] T. Brugger, S. Günther, B. Wang, J. H. Dil, M.-L. Bocquet, J. Osterwalder, J. Wintterlin, and T. Greber. Comparison of electronic structure and template function of single-layer graphene and a hexagonal boron nitride nanomesh on Ru(0001). *Physical Review B*, 79(4):045407, 2009.
- [109] P. Sutter, M. S. Hybertsen, J. T. Sadowski, and E. Sutter. Electronic structure of few-layer epitaxial graphene on Ru(0001). *Nano Letters*, 9(7):2654–2660, 2009.
- [110] A. L. Vázquez de Parga, F. Calleja, M. Borca, M. C. G. Passeggi, J. J. Hinarejos, F. Guinea, and R. Miranda. Periodically rippled graphene: Growth and spatially resolved electronic structure. *Physical Review Letters*, 100:056807, 2008.
- [111] B. Wang, M.-L. Bocquet, S. Marchini, S. Günther, and J. Wintterlin. Chemical origin of a graphene moiré overlayer on Ru(0001). *Physical Chemistry Chemical Physics*, 10:3530–3534, 2008.
- [112] M. C. Wu, Q. Xu, and D. W. Goodman. Investigations of graphitic overlayers formed from methane decomposition on Ru(0001) and Ru(1120) catalysts with scanning tunneling microscopy and high-resolution electron energy loss spectroscopy. *Journal of Physical Chemistry*, 98:5104–5110, 1994.
- [113] Y. Pan, D. X. Shi, and H. J. Gao. Formation of graphene on Ru(0001) surface. *Chinese Physics*, 16:3151–3153, 2007.
- [114] P. W. Sutter, J. I. Flege, and E. A. Sutter. Epitaxial graphene on ruthenium. *Nature Materials*, 7:406–411, 2008.
- [115] B. Wang, S. Günther, J. Wintterlin, and M.-L. Bocquet. Periodicity, work function and reactivity of graphene on Ru(0001) from first principles. *New Journal of Physics*, 12:043041, 2010.
- [116] B. Borca, S. Barja, M. Garnica, M. Minniti, A. Politano, J. M. Rodríguez-García, J. J. Hinarejos, D. Farías, A. L. Vázquez de Parga, and R. Miranda. Electronic and geometric corrugation of periodically rippled, self-nanostructured graphene epitaxially grown on Ru(0001). *New Journal of Physics*, 12:093018, 2010.
- [117] E. Sutter, D. P. Acharya, J. T. Sadowski, and P. Sutter. Scanning tunneling microscopy on epitaxial bilayer graphene on ruthenium (0001). *Applied Physics Letters*, 94:133101, 2009.
- [118] T. Mashoff, M. Pratzner, V. Geringer, T. J. Echtermeyer, M. C. Lemme, M. Liebmann, and M. Morgenstern. Bistability and oscillatory motion of natural nanomembranes appearing within monolayer graphene on silicon dioxide. *Nano Letters*, 10(2):461–465, 2010.
- [119] P. Partovi-Azar, N. Nafari, and M. Reza Rahimi Tabar. Interplay between geometrical structure and electronic properties in rippled free-standing graphene. *Physical Review B*, 83:165434, 2011.

## Bibliography

---

- [120] N. Levy, S. A. Burke, K. L. Meaker, M. Panlasigui, A. Zettl, F. Guinea, A. H. Castro Neto, and M. F. Crommie. Strain-induced pseudo-magnetic fields greater than 300 tesla in graphene nanobubbles. *Science*, 329:544–547, 2010.
- [121] J. Sun, J. B. Hannon, R. M. Tromp, P. Johari, A. A. Bol, V. B. Shenoy, and K. Pohl. Spatially-resolved structure and electronic properties of graphene on polycrystalline Ni. *ACS Nano*, 4(12):7073–7077, 2010.
- [122] V. A. Finkel, M. I. Palatnik, and G. P. Kovtun. X-ray-diffraction study of thermal-expansion of ruthenium, osmium and rhenium at 77-300 degrees K. *Physics of Metals and Metallography-USSR*, 32, 1971.
- [123] A. Herold. Recherche sur les composés d’insertion du graphite. *Bulletin de la Société Chimique de France*, 187:999–1012, 1955.
- [124] S. Horiuchi, T. Gotou, M. Fujiwara, R. Sotoaka, M. Hirata, K. Kimoto, T. Asaka, T. Yokosawa, Y. Matsui, K. Watanabe, and M. Sekita. Carbon nanofilm with a new structure and property. *Japanese Journal of Applied Physics*, 42(Part 2, No. 9A/B):L1073–L1076, 2003.
- [125] C. Lee, X. Wei, J. W. Kysar, and J. Hone. Measurement of the elastic properties and intrinsic strength of monolayer graphene. *Science*, 321:385, 2008.
- [126] J.-C. Charlier, X. Gonze, and J.-P. Michenaud. First-principles study of the stacking effect on the electronic properties of graphite(s). *Carbon*, 32(2):289–299, 1994.
- [127] P. L. de Andres, R. Ramírez, and J. A. Vergés. Strong covalent bonding between two graphene layers. *Physical Review B*, 77(4):045403, 2008.
- [128] T. Wiederholt, H. Brune, J. Wintterlin, R. J. Behm, and G. Ertl. Formation of two-dimensional sulfide phases on Al(111): an stm study. *Surface Science*, 324:91–105, 1995.
- [129] A. T. N’Diaye, J. Coraux, T. N. Plasa, C. Busse, and T. Michely. Structure of epitaxial graphene on ir(111). *New Journal of Physics*, 10:043033, 2008.
- [130] W. Moritz, B. Wang, M.-L. Bocquet, T. Brugger, T. Greber, J. Wintterlin, and S. Günther. Structure determination of the coincidence phase of graphene on Ru(0001). *Physical Review Letters*, 104:136102, 2010.
- [131] D. Martoccia, M. Björck, C. M. Schlepütz, T. Brugger, S. A. Pauli, B. D. Patterson, T. Greber, and P. R. Willmott. Graphene on Ru(0001): a corrugated and chiral structure. *New Journal of Physics*, 12:043028, 2010.
- [132] J. Lu, A. H. Castro Neto, and K. P. Loh. Transforming moire blisters into geometric graphene nano-bubbles. *Nature Communications*, 3:823, 2012.

- 
- [133] M. Iannuzzi and J. Hutter. Comparative study of the nature of chemical bonding of corrugated graphene on Ru(0001) and Rh(111) by electronic structure calculations. *Surface Science*, 605:1360 – 1368, 2011.
- [134] D. Stradi, S. Barja, C. Díaz, M. Garnica, B. Borca, J. J. Hinarejos, D. Sánchez-Portal, M. Alcamí, A. Arnau, A. L. Vázquez de Parga, R. Miranda, and F. Martín. Role of dispersion forces in the structure of graphene monolayers on Ru surfaces. *Physical Review Letters*, 106:186102, 2011.
- [135] S. Grimme. Semiempirical GGA-type density functional constructed with a long-range dispersion correction. *Journal of Computational Chemistry*, 27(15):1787, 2006.
- [136] R. C. Haddon. Hybridization and the orientation and alignment of  $\pi$ -orbitals in nonplanar conjugated organic molecules:  $\pi$ -orbital axis vector analysis (POAV2). *Journal of the American Chemical Society*, 108(11):2837–2842, 1986.
- [137] Gabriele Sclauzero and Alfredo Pasquarello. Carbon rehybridization at the graphene/SiC(0001) interface: Effect on stability and atomic-scale corrugation. *Physical Review B*, 85:161405, 2012.
- [138] X. Peng and R. Ahuja. Epitaxial graphene monolayer and bilayers on Ru(0001) ab initio calculations. *Physical Review B*, 82:045425, 2010.
- [139] J.-P. Cleuziou, W. Wernsdorfer, V. Bouchiat, T. Ondarçuhu, and M. Monthieux. Carbon nanotube superconducting quantum interference device. *Nature nanotechnology*, 1(1):53–59, 2006.
- [140] H. Brune and P. Gambardella. Magnetism of individual atoms adsorbed on surfaces. *Surface Science*, 603(10-12):1812–1830, 2009.



# Acknowledgements

First and foremost, I would like to thank my thesis advisor, Prof. Harald Brune, for offering me the possibility to carry out this very exciting thesis project. I am particularly grateful for his wise guidance throughout the project, for the excellent working conditions, for taking care of always having someone working with me on the wonderful, yet very demanding, ultralow-temperature STM, and for not only having allowed, but also encouraged me to attend conferences, workshop and schools, where I certainly learned a lot.

I thank Prof. Phil Willmott, Dr. Jens Wiebe, and Prof. Marco Gioni for doing me the honour of having accepted to be part of my thesis jury, and Prof. Georges Meylan for having presided it.

I want to thank Dr. Markus Etzkorn, Dr. Fabián Calleja, Dr. Fabio Donati, with whom I am very happy to have worked on the various subjects presented in this thesis. Sharing the lab work, the long measurement runs, the data analysis and article writing, the office, the week-end refilling of the cryostat, and so much more, was a fantastic experience and a real pleasure. Thanks for sharing your theoretical and technical knowledge with me, in five words, thanks for teaching me everything! Vielen Dank! Muchas gracias! Grazie mille!

Thanks to Dr. François Patthey for his many and significant contributions to the improvement of the machine, thanks for having made our life in the lab easier! Thanks for all the precious help, I learned a lot from his remarkable ability and expertise.

I particularly thank all my colleagues in the Laboratory of Nanostructures at Surfaces, past and present, who are too many to name. Thanks for the help, especially with my thesis manuscript and presentation, thanks for the friendly atmosphere, for the lively lunch and coffee breaks, and for the many activities we shared.

I also want to thank the Institute of Condensed Matter Physics staff members. Thanks to Gilles Grandjean and his co-workers of the mechanical and electrical workshops for their technical help, their availability, their understanding, and their remarkable work. Thanks to Martial Doy and Primo Locatelli for the IT support, and to Chantal Roulin and Florence Grandjean for taking care admirably of all the administrative tasks.

Last but not least, I want to thank my family, relatives, friends, and fellow church members for their unfailing support throughout this great experience.

*Lausanne, le 10 avril 2013*

Q. Dubout



# Curriculum vitae

Quentin Dubout

Born: 04.02.1987, St-Julien-en-Genevois, France

Nationality: Swiss/French

## Education

2009 – 2013 PhD studies / teaching assistant, EPFL, Lausanne, Switzerland.

2007 – 2009 Master's degree in Physics (Ing. Phys. Dipl. EPF), EPFL Lausanne, Switzerland.

2004 – 2007 Bachelor's degree in Physics, EPFL, Lausanne, Switzerland.

2006 – 2007 Third year of bachelor at The University of Nottingham, UK (exchange program).

2000 – 2004 Baccalauréat scientifique (A-level), Lycée International Ferney Voltaire, France.

## Publications

*"Two Distinct Phases of Bilayer Graphene Films on Ru(0001)"*, M. Papagno, D. Pacilé, D. Topwal, P. Moras, P. M. Sheverdyaeva, F. D. Natterer, A. Lehnert, S. Rusponi, **Q. Dubout**, F. Calleja, E. Frantzeskakis, S. Pons, J. Fujii, I. Vobornik, M. Grioni, C. Carbone, and H. Brune, *ACS Nano* **6**, 9299 (2012).

*"Magnetic moment and anisotropy of individual Co atoms on graphene"*, F. Donati, **Q. Dubout**, G. Autès, F. Patthey, F. Calleja, P. Gambardella, O. V. Yazyev, and H. Brune, *submitted to Nature Physics*.

*"Structure of mono- and bilayer graphene on Ru(0001)"*, **Q. Dubout**, F. Calleja, G. Sclauzero, M. Etzkorn, A. Lehnert, L. Claude, S. Rusponi, M. Papagno, A. Pasquarello, and H. Brune, *in preparation*.

*"Hydrogen-induced Kondo effect for single Co atoms on Pt(111)"*, **Q. Dubout**, F. Calleja, M. Etzkorn, F. Donati, A. Lehnert, L. Claude, P. Gambardella, and H. Brune, *in preparation*.